University of Strathclyde

Department of Mechanical & Aerospace Engineering

An Open-Source CFD Solver for Planetary Entry

Vincent Casseau

A thesis presented in fulfilment of the requirements
for the degree of Doctor of Philosophy

2017

Declaration of author's rights

This thesis is the result of the author's original research. It has been composed by the author and has not been previously submitted for examination which has led to the award of a degree.

The copyright of this thesis belongs to the author under the terms of the United Kingdom Copyright Acts as qualified by University of Strathclyde Regulation 3.50. Due acknowledgement must always be made of the use of any material contained in, or derived from, this thesis.

<div align="right">

Vincent Casseau

April 2017

</div>

Abstract

hy2Foam is a newly-coded open-source two-temperature computational fluid dynamics (CFD) solver that aims at (1) giving open-source access to a state-of-the-art hypersonic CFD solver to students and researchers; and (2) providing a foundation for a future hybrid CFD-DSMC (direct simulation Monte Carlo) code within the OpenFOAM framework. Benchmarking has firstly been performed for zero-dimensional test cases and *hy2Foam* has then been shown to produce results in good agreement with previously published data for a 2D-axisymmetric Mach 11 nitrogen flow over a blunted cone and with the *dsmcFoam* code for a series of Fourier cases and a 2D Mach 20 cylinder flow for a binary reacting mixture. This latter case scenario provides a useful basis for other codes to compare against. *hy2Foam* and *dsmcFoam* capabilities have eventually been utilised to derive and to test a new set of chemical rates based on quantum-kinetic theory and that could be employed for Earth atmospheric re-entry computations.

"Alone we can do so little; together we can do so much"

- Helen A. Keller

List of Publications

Journal Articles

V. Casseau, D. E. R. Espinoza, T. J. Scanlon, and R. E. Brown. A Two-Temperature Open-Source CFD Model for Hypersonic Reacting Flows, Part Two: Multi-dimensional Analysis. *Aerospace*, 3(4):45, 2016.

V. Casseau, R. C. Palharini, T. J. Scanlon, and R. E. Brown. A Two-Temperature Open-Source CFD Model for Hypersonic Reacting Flows, Part One: Zero-dimensional Analysis. *Aerospace*, 3(4):34, 2016.

C. White, R. C. Palharini, V. Casseau, and T. J. Scanlon. Chemical Reactions Involving Charged Species in an Open Source DSMC Solver. *Considered for publication*, 2017.

Conference proceedings and unpublished conference papers

V. Casseau, D. E. R. Espinoza, and T. J. Scanlon. Open-source High-fidelity Solvers Dedicated to Re-entry Analysis and Design for Demise. 31st Oct. – 3rd Nov. 2016. Paper presented at the Final Stardust Conference, ESA-ESTEC, Noordwijk, the Netherlands.

V. Casseau, T. J. Scanlon, and R. E. Brown. Development of a Two-Temperature Open-Source CFD Model for Hypersonic Reacting Flows. *AIAA*, Paper 2015-3637, 2015.

V. Casseau, T. J. Scanlon, B. John, D. R. Emerson, and R. E. Brown. Hypersonic Simulations using Open-Source CFD and DSMC Solvers. *AIP Conference Proceedings*, 1786(1):050006, 2016.

D. E. R. Espinoza, V. Casseau, T. J. Scanlon, and R. E. Brown. An Open Source Hybrid CFD-DSMC Solver for High-Speed Flows. *AIP Conference Proceedings*, 1786(1):050007, 2016.

J.-J. Hoste, V. Casseau, M. Fossati, I. J. Taylor, and R. J. Gollan. Numerical Modeling and

Simulation of Supersonic Flows in Propulsion Systems by Open-Source Solvers. *AIAA*, Paper 2017-2411, 2017.

T. J. Scanlon, R. C. Palharini, C. White, D. E. R. Espinoza, and V. Casseau. Simulations of rarefied and continuum hypersonic flow over re-entry objects. Mar. 2015. Paper presented at 8th European Symposium on Aerothermodynamics for Space Vehicles, Lisbon, Portugal.

Webpage

Github repository of the *hy2Foam* solver. `https://github.com/vincentcasseau/hyStrath/`, 2017. Version 1.0, commit 8b44e95.

Acknowledgements

Contents

List of Figures

List of Tables

Nomenclature

Greek Symbols

α — thermal accommodation coefficient in the Smoluchowski temperature jump boundary condition

α_{KNP} — upwind bias in the Kurganov, Noelle and Petrova scheme

α_m — fraction of the dissociation energy needed for calculation of the dissociation potential

α_P — trans-rotational temperature exponent in the Park TTv model

β — temperature exponent in the modified Arrhenius law

δ — Kronecker delta

$\Delta_{s,r}^{(1)}$ — collision term for species s and r, m s

ζ — degree of freedom

ϵ_a — energy of activation, kg m^2 s^{-2}

ϵ_{coll} — collision energy, kg m^2 s^{-2}

$\epsilon_{m,i,P}$ — energy of particle P for a specific mode m and level i, kg m^2 s^{-2}

Γ — gamma function

γ — ratio of specific heats

θ_v — characteristic vibrational temperature, K

$\theta_{el,i}$ characteristic electronic temperature of the excited electronic level i, K

κ thermal conductivity, kg m s^{-3} K^{-1}

λ second viscosity coefficient, kg m^{-1} s^{-1}

μ shear viscosity, kg m^{-1} s^{-1}

μ_b bulk viscosity, kg m^{-1} s^{-1}

ϕ_f volumetric flux, m^3 s^{-1}

ϕ_s scaling factor for species s

$\boldsymbol{\Psi}$ tensor field of any rank

ρ gas density, kg m^{-3}

ρ_s partial density of species s, kg m^{-3}

σ tangential momentum accommodation coefficient in the Maxwell velocity slip boundary condition

$\sigma_{m,s}$ collision cross-section of species m and s based on the respective molecular diameters, m^2

σ_v limited collision cross-section, m^2

$\boldsymbol{\tau}$ shear stress tensor

$\tau_{m-s,V-T}$ interspecies vibrational-translational relaxation time for species s and m, s

τ_{V-T} vibrational-translational relaxation time, s

$\dot{\omega}$ net mass production of species, kg m^{-3} s^{-1}

$\dot{\omega}_v$ vibrational source term, kg m^{-1} s^{-3}

ω temperature coefficient of viscosity

$\Omega_{s,r}^{(1,1)}$ binary collision integral for species s and r, m^3 s^{-1}

$\bar{\Omega}_{s,r}^{(1,1)}$ collision cross-section for species s and r, m^2

$\omega_{f,\text{KNP}}$ diffusive volumetric flux, m^3 s^{-1}

Roman Symbols

A pre-exponential factor in the Arrhenius law, m^3 s^{-1} mol^{-1} (or m^3 s^{-1} molecule^{-1} when specified)

a speed of sound

$A_{m,s}$, $B_{m,s}$ coefficients in the Millikan-White correlation relative to species m and s

$A_{B,s} - C_{B,s}$ coefficients in Blottner's equation

$A_D - D_D$ coefficients in Gupta's 1989 curve fit for binary diffusion coefficients

$A_{\bar{\Omega}^{(1,1)}} - D_{\bar{\Omega}^{(1,1)}}$ coefficients in Gupta's 1990 curve fit for collision cross-sections

$\mathscr{A}^*$, $\mathscr{B}$, $\mathscr{F}$ coefficients in the Armaly and Sutton mixing rule

C species concentration

C_D drag coefficient

C_H integrated wall heat flux, kW

$\bar{c}$ average molecular speed, m s^{-1}

Cp heat capacity at constant pressure, m^2 s^{-2} K^{-1}

C_f skin-friction coefficient

C_p pressure coefficient

Cv heat capacity at constant volume, m^2 s^{-2} K^{-1}

d diameter, m

D_s effective diffusion coefficient of species s in the mixture, m^2 s^{-1}

D_s dissociation potential of species s, m^2 s^{-2}

$D_{s,r}$	binary diffusion coefficient for species s and r, m^2 s^{-1}
e	energy per unit mass of species, m^2 s^{-2}
E	total energy, kg m^{-1} s^{-2}
$\boldsymbol{\mathcal{F}}_{i,inv}$	flux vector for coordinate i ($= x$, y or z), inviscid contribution
$\boldsymbol{\mathcal{F}}_{i,vis}$	flux vector for coordinate i ($= x$, y or z), viscous contribution
g_i	degeneracy of the excited electronic level i
h	enthalpy per unit mass of species, m^2 s^{-2}
h°	chemical enthalpy, m^2 s^{-2}
$i_{\max}$	maximum vibrational quantum level available to a molecule
$\boldsymbol{\mathcal{J}}$	species diffusion vector
k_B	Boltzmann constant, kg m^2 s^{-2} K^{-1}
k_b	backward reaction rate constant
K_{eq}	equilibrium constant
k_f	forward reaction rate constant, m^3 s^{-1} mol^{-1}
Kn/Kn_{ov}	(overall) Knudsen number
Kn_{Br}	continuum-breakdown parameter
Kn_{GLL}	local gradient-length Knudsen number
Le	Lewis number
m_s	mass of one particle of species s, kg
$\mathfrak{m}_{s,r}$	reduced mass of species s and r, kg
$\mathcal{M}_s$	molecular weight of species s, kg mol^{-1}
$\mathcal{M}_{s,r}$	reduced molecular weight of species s and r, kg mol^{-1}

N_A Avogadro number, mol^{-1}

n number density, m^{-3}

$\mathfrak{N}_m$ cut-off value for the number of vibrational energy levels considered for the molecule m in the CVDV model

N_s number of species in the mixture

N_v number of molecules in the mixture

p total pressure, Pa (or atm when specified)

p_s partial pressure of species s, Pa

Pr Prandtl number

$P_{s,r}$ assessed probability exchange of species s and r

$\mathbf{q}$ heat conduction vector

Q_{e-i} energy loss due to electron impact ionization reactions, $\text{kg m}^{-1}\text{ s}^{-3}$

Q_{e-V} electron-vibration energy transfer, $\text{kg m}^{-1}\text{ s}^{-3}$

Q_{h-e} heavy particle-electron energy transfer, $\text{kg m}^{-1}\text{ s}^{-3}$

Q_{C-V} chemistry-vibration source term, $\text{kg m}^{-1}\text{ s}^{-3}$

Q_{V-T} vibrational-translational energy transfer, $\text{kg m}^{-1}\text{ s}^{-3}$

Q_{V-V} vibrational-vibrational energy transfer, $\text{kg m}^{-1}\text{ s}^{-3}$

R specific gas constant, $\text{m}^2\text{ s}^{-2}\text{ K}^{-1}$

$\mathcal{R}$ universal gas constant, $\text{kg m}^2\text{ s}^{-2}\text{ K}^{-1}\text{ mol}^{-1}$

$\boldsymbol{S}_f$ vector area of face f

St Stanton number

T_c controlling temperature, K

T_a	temperature of activation, K
T_F	modified temperature in the CVDV model, K
t	time, s
T_{ov}	overall temperature, K
T_P	Park's temperature, K
T_{tr}	trans-rotational temperature, K
T_{ve}	vibro-electronic temperature, K
u, v, w	components of the velocity vector, m s^{-1}
$\boldsymbol{\mathcal{U}}$	vector of conserved quantities
U_m	factor related to species s in the CVDV model, K
u_s	tangential slip velocity
$\boldsymbol{U}$	velocity vector
$\dot{\boldsymbol{\mathcal{W}}}$	source vector
X	molar-fraction
Y	mass-fraction
Z	collision number

Subscripts

e	electron
el	electronic
$+, -$	outward and inward directions of the owner cell
f	cell face
KNP	reference to the Kurganov, Noelle and Petrova scheme

mix	mixture
ov	overall
r	rotational
ref	reference
t	translational
tr	trans-rotational
v	vibrational
ve	vibro-electronic
wall	wall

Superscripts

0	initial
eq	equilibrium

Abbreviations

AIAA	American Institute of Aeronautics and Astronautics
AUSM	Advection Upstream Splitting Method
cFASTT	Centre for Future Air-Space Transportation Technology
CFD	computational fluids dynamics
COOLFluiD	Computational Object-Oriented Libraries for Fluid Dynamics
CVDV	coupled vibration-dissociation-vibration
DAC	the DSMC Analysis Code
DK	Dunn and Kang experiments
DLR	German Aerospace Center

DPLR   Data-Parallel Line Relaxation

DSMC   direct simulation Monte-Carlo

eid   electron impact dissociation

eii   electron impact ionization

EPSRC   Engineering and Physical Sciences Research Council

ESA   European Space Agency

ESTEC   European Space Research and Technology Centre

EXPERT   European eXPErimental Re-entry Test-bed

FG   use of modified Fick's law and Gupta's curve fits

FS   use of modified Fick's law and Stephani's expression

HLLC   Harten–Lax-van Leer–Contact

KNP   Kurganov, Noelle and Petrova

LAURA   Langley Aerothermodynamic Upwind Relaxation Algorithm

LeMANS   the aerothermal Navier-Stokes solver of the University of Michigan

LTS   local time stepping

MPI   message passing interface

MUTATION   Multicomponent Thermodynamic And Transport properties for Ionized gases

MW   Millikan and White correlation

MWP   Millikan and White correlation with Park's correction

NASA   National Aeronautics and Space Administration

NR   non-reacting

NSF   Navier–Stokes–Fourier

NTC   no time counter

OpenFOAM   Open Field Operation and Manipulation

QK   Quantum Kinetics

SMILE   Statistical Modeling In Low-density Environment

SPARTA   Stochastic PArallel Rarefied-gas Time-accurate Analyzer

SRC   sample return capsule

SSH   Schwartz, Slawsky, and Herzfeld

TCE   total collision energy

TVD   total variation diminishing

US3D   UnStructured 3D

V–T   vibrational-translational

V–V   vibrational-vibrational

VHS   variable hard sphere

VKI   the Von Karman Institute

Chapter 1

Introduction

1.1 Background

The study of high-speed vehicles entering a planetary atmosphere is of current interest as witnessed by the ongoing tests on the Orion capsule (see Figure 1.1(a)) [1, 2]. This exploration vehicle, conceived by the National Aeronautics and Space Administration (NASA), has the goal to take humans farther into space and is thought to ultimately be able to ferry and sustain a crew during a journey to Mars in the 2030s. Access to space continues to be a challenging area with significant economic and scientific implications in the near-future for the leading countries [3, 4]. Mastering the art of the high-speed regime is not solely limited to space missions though and new prospects may emerge such as those related to hypersonic civilian transportation. This future vision of air-space transportation is embodied by vehicles, such as the cFASTT-1 [5] shown in Figure 1.1(b) designed in the Centre for Future Air-Space Transportation Technology (cFASTT) at the University of Strathclyde, flying at cruise-altitudes around ten times higher than today's aircraft. However, many scientific and technological hurdles remain to be cleared before turning this future into a reality. The technological challenges remain considerable from an engineering, environmental, and societal standpoint [6]. In particular, previous missions have highlighted the harsh environment experienced by a spacecraft during the descent phase and the essential role played by thermal protection systems to preserve the integrity of the vehicle. The accurate prediction of aerodynamic and thermal loads are thus a vital prerequisite to any outer space missions. Despite the

significant amount of studies focusing on the subject area since the 1960s [7] a thorough understanding and characterisation of the aerothermodynamic flow conditions during re-entry is yet to be resolved as no definitive models exist to describe the wide range of physical phenomena encountered by the re-entry craft.

(a) Orion spacecraft. Credit: National Aeronautics and Space Administration (NASA)

(b) cFASTT-1 hypersonic airliner.
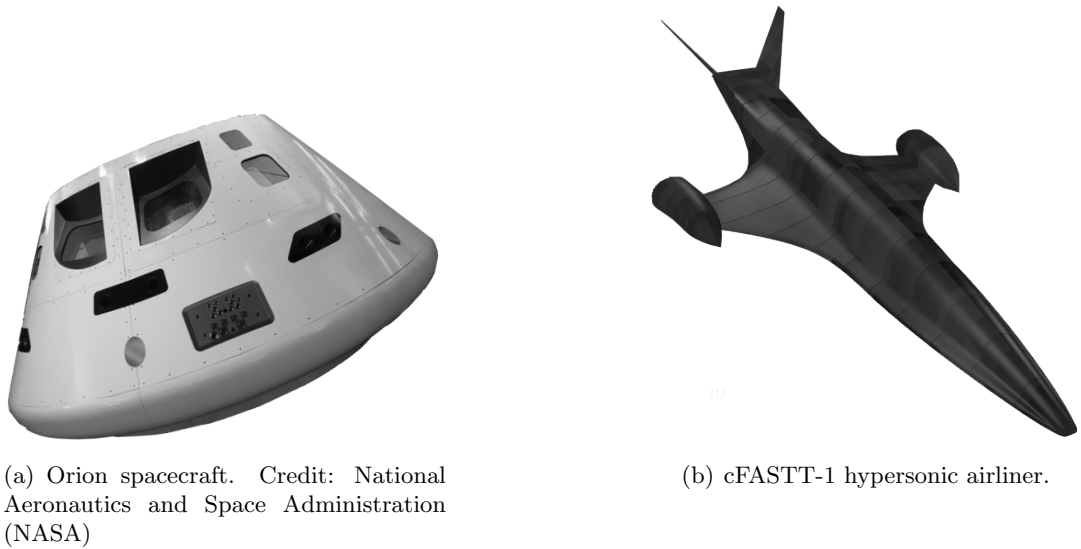
Figure 1.1: Two visions of the future of air-space transportation

1.2   Re-entry flow regimes and related numerical aspects

The highly complex flow field surrounding a re-entry vehicle needs to be captured by means of numerical simulations with a satisfactory level of accuracy and within realistic timescales. The Knudsen number, Kn, defined as the ratio of the mean free path of the gas particles to the characteristic length of the problem, is commonly employed to gauge the degree of rarefaction of a gas. During the entry in a planetary atmosphere at hypervelocities, a craft will traverse the full range of the Knudsen number, from the free-molecular regime down to the continuum regime (see Figure 1.2) due to the change in atmospheric density with altitude. These regimes are shown in the altitude-velocity map in Figure 1.3 along with other characteristic flow features.

Re-entry flight paths for the Space Shuttle, the Apollo mission (lunar return), a Mars return and a far Solar system return are shown. For the later two, the initial descent is not displayed but their re-entry velocities are approaching 16 km s^{-1}. As a
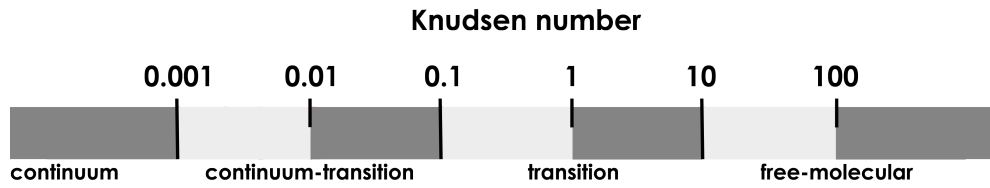
Knudsen number

Figure 1.2: Flow regimes depending on the Knudsen number

vehicle initiates its descent in the atmosphere, it first encounters a collisionless environment where the free-stream flow particles are widely spaced apart and are essentially interacting with the craft surface but not between each other. This region obeys to the free-molecular flow regime. From that follows the transition regime that exhibits the on-set of particle collisions within the gas flow and the flow-field is greatly affected as a consequence with the formation of strong shock waves, a dramatic increase in the wall heat flux and the rise of aerodynamic forces as the altitude reduces. There is still an insufficient amount of inter-particle collision events and this results in a flow that departs significantly from thermal equilibrium. The chemically reacting environment over the craft has also to be accounted for as it is of importance for the correct prediction of aerodynamic loads and surface heating. Ranges for reactions of dissociation and ionization to occur are highlighted on the map. The atmosphere gets denser at lower altitudes and the vehicle then enters into the continuum-transition regime that is composed of a mixture of continuum and non-continuum flows. Under the flow conditions at these altitudes, rarefied flow areas are located in the wake of the vehicle and in regions of strong gradients in shocks waves and boundary layers [8]. Finally, the transition between laminar and turbulent flow is shown to be taking place at altitudes slightly below 60 km and it is observed that it is delayed as the Mach number increases [9].

Practically, this translates into the need for different numerical techniques to resolve the flow-field past such hypersonic bodies. The two approaches considered in this thesis are the direct simulation Monte Carlo (DSMC) method and conventional computational fluid dynamics (CFD). They present the advantage of being well-established numerical techniques in the hypersonics community, being both widely used in academia and space agencies, whereas industry is predominantly using CFD. As such they can be described as relatively engineering-friendly approaches. The DSMC particle-based methodology
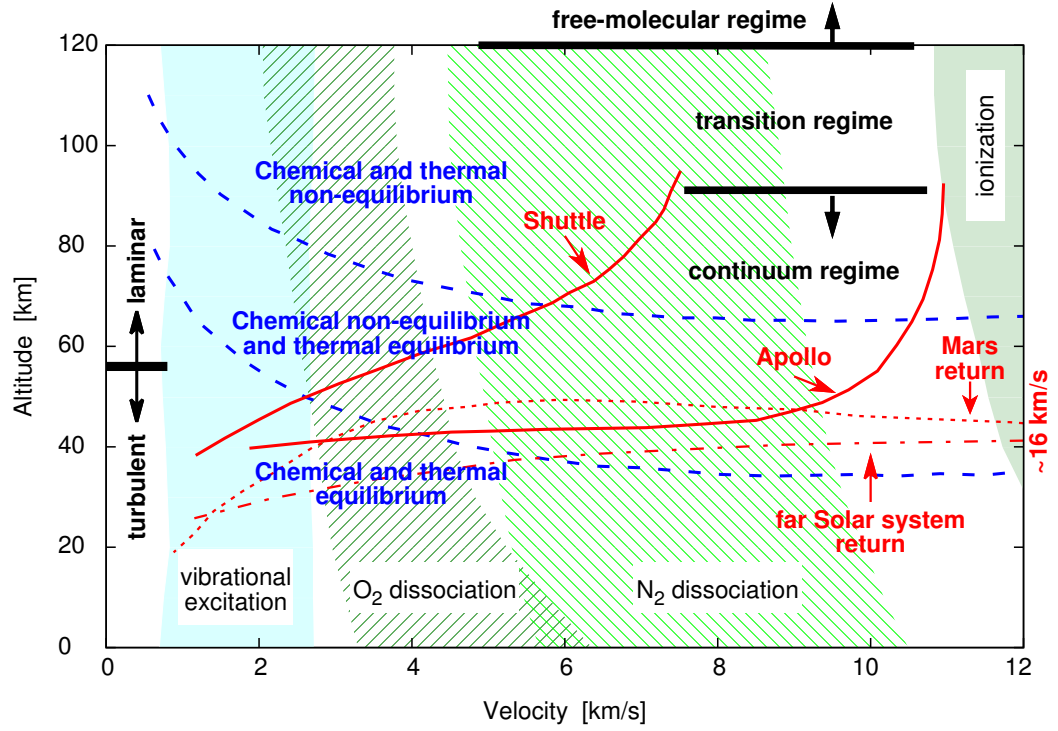
Figure 1.3: Flow-field features encountered during the Earth atmosphere re-entry (adapted from Longo *et al.* [10] and Anna [11]). The band limits are defined as 10% and 90% of the phenomenon full activation.

developed by Bird [12] is numerically efficient for high Knudsen number flows but requires significant computational effort when Kn is less than 0.05, which occurs when solving continuum regions. Abbate *et al.* [13] reported that the computational demands of DSMC scale with Kn^{-4}. As an example, following this rule of thumb would yield to a couple of hours DSMC real time for the simulation of a flow field with $Kn = 0.1$, and to a day and a year of computations using values of Kn equal to 0.05 and 0.005, respectively. Conversely, the CFD approach that solves the Navier–Stokes–Fourier (NSF) equations is generally adopted for the lower altitude range. NSF solutions are appropriate for continuum flows (Kn below 0.005) but fail to accurately predict non-equilibrium flow behaviour. To extend the range of applicability of the NSF equations towards the transition regime, Park formulated the two-temperature CFD model [14], thus distinguishing the trans-rotational energy pool from the vibro-electronic energy pools and modelling the energy exchange processes via vibrational rate equations.

In between higher and lower altitudes lies an intermediate zone where DSMC is computationally prohibitive and where conventional CFD fails due to the presence of

non-continuum regions within the flow-field [15]. For re-entry studies into the Earth's atmosphere, this region typically spans from 60 to 80 km altitude, while for Mars entry it lies at lower altitudes. The numerical resolution of such problems is detailed in the subsequent section.

1.3 Flow computations at intermediate altitudes

In the light of the previous discussion, hybrid CFD-DSMC simulations naturally emerge as a potential candidate to address the issue created by the co-existence of non-continuum and continuum areas within the flow-field, and therefore to explore flow-fields across the whole range of Knudsen numbers. However, CFD-DSMC coupling possesses potential pitfalls due to fundamental differences between CFD and DSMC solving methodologies. Indeed, Petkow *et al.* [16] stated that there might be some issues in the optimisation and parallelisation processes and that special care should be given to ensure numerical stability. Burt and Boyd [17] emphasized the fact that the disadvantage of DSMC is its large statistical scatter and that there might be a problem when transferring information from the DSMC domain to the CFD boundary, unless significant computational effort is undertaken to reduce the statistical noise.

All continuum/rarefied coupling methods involve the definition of a breakdown parameter to determine the extent of the continuum and particle zones, and thus the position of the continuum/particle interface (and if required its spatial evolution with respect to the simulation time). The initial position of the interface is crucial to ensure the accuracy and numerical efficiency of any coupling methodology. Indeed, an incorrect initial position of the interface, *i.e.*, an interface located out of the collisional equilibrium region, will generate physical inaccuracies because the NSF equations are not valid in this region. So, maximizing the numerical efficiency is synonymous with an interface location being as close as possible to the edge of the non-equilibrium region, since it limits the spatial extent of the DSMC domain and hence saves computational time. The local gradient-length Knudsen number initially proposed by Boyd [18] is extensively used as a breakdown parameter in the literature, *e.g.* in [8, 13, 19, 20], and is defined as follows

$$Kn_{GLL-\phi} = \frac{\lambda}{\phi}|\nabla\phi| \tag{1.1}$$

where λ is the local mean free path of the gas molecules and ϕ is a local macro-scopic flow quantity such as the gas density ρ, the magnitude of the velocity vector $|\mathbf{U}|$ (or $max\,(|\mathbf{U}|,a)$ in the denominator where a is the speed of sound for low-speed regions [21]), or a temperature T. The degree of local continuum breakdown is then evaluated as the maximum for all the three aforementioned flow quantities

$$Kn_{GLL} = max\,\big(Kn_{GLL-\rho},\, Kn_{GLL-T},\, Kn_{GLL-|\mathbf{U}|}\big) \tag{1.2}$$

An improvement of this formulation that can be obtained from a DSMC computa-tion has been proposed in [22]. The breakdown parameter given in Eq. 1.2 works well in pre-shock, stagnation and wake regions, whereas the one defined in Eq. 1.3 is also said to better reproduce the thermal non-equilibrium in the post-shock region that is not accounted for in Eq. 1.2. It states

$$Kn_{GLL} = max\,\left(Kn_{GLL-\rho},\, Kn_{GLL-T},\, Kn_{GLL-|\mathbf{U}|},\, 5\times\frac{T_t - T_r}{T_r}\right) \tag{1.3}$$

where T_t and T_r are the local translational and rotational temperatures of the gas molecules, respectively. Cut-off values of the continuum-breakdown parameter, de-noted as Kn_{Br}, that are slightly greater or equal to 0.05 are often recommended for hypersonic flows (see *e.g.* [8, 18, 22–24]). Boyd and Deschenes [23] claimed that a conservative value of 0.05 should not introduce more than 5 % error within a hybrid simulation compared to a full DSMC simulation. A general discussion of the various continuum-breakdown parameters has been conducted by Boyd [25] and their influence on accurately reproducing shock waves and gas expansion flow features is debated. Some definitions of breakdown parameters are also presented in [23].

Detail about CFD-DSMC coupling methodologies are outside of the scope of this study and the reader is referred to [8, 13, 26, 27]. Instead, the functioning of the hybrid solver is treated as a black box and the interest is placed on the inputs and outputs from the CFD code perspective. This is represented in Figure 1.4.

After the calculation of the Kn_{GLL} number, the required CFD outputs are: the
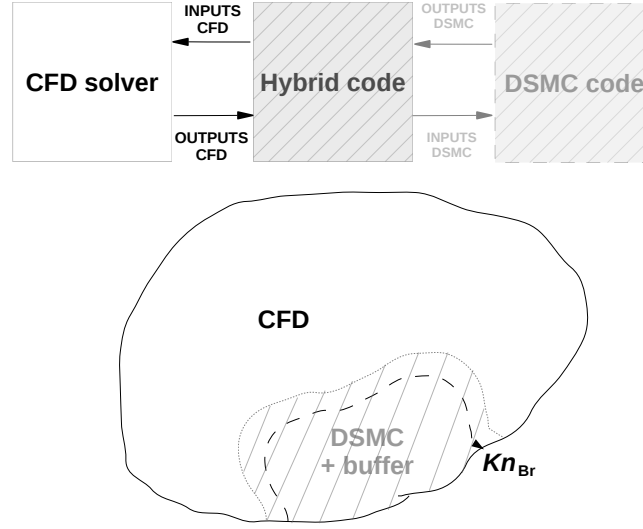
Figure 1.4: Sketch of the computational domain and basic communications when using a hybrid code

extent of the DSMC region(s) as prescribed by Kn_{Br}, and within these regions the velocity, the temperatures, the density, the partial density for each of the species, and in some cases the diffusion velocities. Conversely, the CFD solver should accommodate with the following inputs for the whole computational domain: the velocity, the temperatures, the density, and the partial densities for each of the species.

1.4   Previous contributions

There are various ways of classifying the many CFD and DSMC solvers that gravitate around the hypersonic community. One of them is their accessibility to the public and following this direction, previous efforts to simulate hypersonic flows can fall into two categories: proprietary and open-source codes. Proprietary codes include specialised in-house solvers developed in a given institution for the specific task of modelling hypersonic flows and whose source code is not meant to be shared and used freely by anyone outwith this institution or partner laboratories. Among proprietary CFD codes dedicated to the hypersonic regime are NASA's LAURA (Langley Aerothermodynamic Upwind Relaxation Algorithm) [28], DPLR (Data-Parallel Line Relaxation) [29], Le-MANS [30, 31] the aerothermal Navier-Stokes solver of the University of Michigan, US3D (UnStructured 3D) [32, 33] from the University of Minnesota and the TAU

solver [34] from the German Aerospace Center (DLR). In terms of proprietary DSMC solvers, there are essentially DS1V, DS2V and DS3V by Bird [35, 36], MONACO [37] from the University of Michigan, DAC [38] (the DSMC Analysis Code) from NASA's Langley Research Center and later Johnson Space Center and SMILE [39] (Statistical Modeling In Low-density Environment) by the Laboratory of Computational Aerodynamics in the Khristianovich Institute of Theoretical and Applied Mechanics of the Siberian Branch of the Russian Academy of Sciences.

Proprietary codes also include commercial codes which are designed to accommodate the needs of most companies/users, thus providing a reasonable solution to a wide range of flow problems and therefore being labelled as general purpose codes. Ansys FLUENT [40] and CFD++ [41] for instance possess features for aeronautical and aerospace applications.

In their review on the "evaluation of CFD codes for hypersonic flow modeling" dated July 2010, Maicke and Majdalani [42] pointed out two main driving parameters for the selection of a CFD code in a preliminary design phase. Those were computational efficiency and the ease of use[1]. They insisted on the latter driver and in particular on the logical bridge that can be made between education and engineering. According to them, the benefits of CFD code accessibility at college level are twofold: a) an improved understanding of the modelling of physical phenomena and especially a better comprehension of the underlying assumptions which guarantee that models can be applied in certain conditions, and b) a gain in confidence in the work they produce after graduation. This is of primordial interest considering that a great deal of knowledge and skills are needed to meet the needs of the high-speed sector that is very demanding but nonetheless exciting. In this regard, concrete hands-on sessions and projects to complement lectures and tutorials at university level should indeed seek to develop scientific aptitudes but also to nurture scientific vocations. And yet not all universities can afford costly commercial solvers and even fewer of them can benefit from restricted in-house hypersonic codes. Hence, an overview of the main open-source codes for planetary entry purposes is given in the subsequent paragraphs.

---

[1]Please note that all reviewed codes were proprietary codes in the absence of open-source solvers for such purpose. It is therefore implied here that the code features are rigorously verified/validated.

1.4.1   Open-source DSMC codes

dsmcFoam and _dsmcFoam+_

For low-density flow conditions, a DSMC solver called _dsmcFoam_ (first publication in 2010) has been developed and validated within the framework of the open-source CFD platform OpenFOAM (Open Field Operation and Manipulation) [43] at the University of Strathclyde [44, 45]. The two main features of _dsmcFoam_ are that vibrational-translational post-collision energy redistribution is executed using a quantum version of the Larsen-Borgnakke procedure [44, 46] and that chemical reactions are described by Quantum-Kinetic (QK) theory, as initially proposed by Bird [47]. It has recently received the addition of the electronic energy and this version is renamed _dsmcFoam+_ [48, 49] and more details will be given in Chapter 2. The code can model arbitrary 2D/3D geometries while taking advantage of unlimited parallel processing. Focusing solely on space applications, _dsmcFoam_ has served to compute flow-fields past the Orion and SARA capsules [45, 50], the demise of a satellite [51] and the interaction of a rocket plume with the Martian soil [52].

SPARTA

SPARTA (Stochastic PArallel Rarefied-gas Time-accurate Analyzer) [53] (first publication in 2014 [54]) is a massively parallel C++ DSMC code developed by Sandia National Laboratories that performs 2D or 3D simulations of rarefied gases. It possesses all the required capabilities for planetary entry studies such as the ability to model ionized plasmas and to deal with both gas-phase and surface chemistry reactions to name just a few. SPARTA has so far been applied to model the Richtmyer-Meshkov instability [55] and to resolve the case of a hypersonic flat plate and flows over a flared cylinder and a planetary probe [56].

1.4.2   Open-source CFD codes

Eilmer3

Eilmer3 [57, 58] is a C++ solver from the University of Queensland, Australia. Hyper-velocity external flows have been tackled by Gollan [59] and a two-temperature model

was developed. The implementation was tested for an inviscid, frozen flow of nitrogen over a 2D cylinder and a steady 1D shock tube simulation. The code was used to simulate expansion tube operation. Further work on hypersonic flow problems verification and validation included for example [58] and a list of all undergraduate projects using Eilmer3 can be found in Ref. [60]. Current focus is set on modelling high-speed internal flows dealing in particular with the interaction between combustion and turbulence for potential propulsion applications, *e.g.* scramjet flow-field simulations.

COOLFluiD

COOLFluiD (Computational Object-Oriented Libraries for Fluid Dynamics) [61, 62] is a C++ platform created in 2002 at the Von Karman Institute (VKI) for Fluid Dynamics in Rhode-St-Genèse, Belgium. It has been released open-source in 2014. State-of-the-art thermodynamic and transport models for high-speed entry are implemented in the C++ MUTATION (Multicomponent Thermodynamic And Transport properties for Ionized gases) library and the parallel implicit finite-volume CFD solver within the COOLFluiD platform has been shown to be robust and to provide satisfactory solutions when simulating chemically reacting flows up to Mach 35 [63]. Performed computations included for example the vehicle forebody of the European eXPErimental Re-entry Test-bed (EXPERT) and the Stardust Sample Return Capsule (SRC) [63].

1.5   Project objectives

The aim of this project is to lay the foundations for solutions of satisfactory accuracy using time-efficient open-source simulations to traverse the full spectrum of rarefied to continuum conditions during the planetary atmosphere entry of a spacecraft. As stated earlier in this Chapter, the problem is to be addressed from an engineering perspective and the CFD and DSMC approaches are customarily employed in this framework.

For high altitudes, the *dsmcFoam* code is a natural candidate because of a) its maturity, b) the good exposure it benefits from thanks to the OpenFOAM platform -that is widely used in academia and in industrial research [64]-, and c) the expertise of the group at the Universities of Strathclyde and Glasgow. *dsmcFoam* was in fact the

only open-source DSMC code to contain all the required features for Earth atmospheric re-entry when this work was initiated early in 2014.

At low altitudes, an open-source two-temperature CFD solver is required and although Eilmer3 would certainly merit consideration, the reasons why this option was not retained are twofold: a) the code is fully explicit which greatly affect its computational efficiency, and b) hypersonic developments are thought to be resumed with the release of Eilmer4 [65] that is coded in D language. As for COOLFluiD, it was not an option as of early 2014 since its first open-source release came later in September 2014 and the platform does not benefit from a user community as large as OpenFOAM. On practical grounds having CFD, DSMC and hybrid CFD-DSMC solvers coded into more than one platform would make their distribution cumbersome. The learning curve for the user would also be steeper having to get accustomed to two different platforms. With the benefit of hindsight[2], implementing hypersonic CFD capabilities directly within the OpenFOAM framework undeniably facilitates communications between the CFD and DSMC solvers in an attempt to anticipate future code developments. Indeed, in parallel to this work investigations led by Espinoza *et al.* [66] on a hypersonic hybrid hydrodynamic-molecular gas flow solver to operate at intermediate altitudes are underway and should ultimately use *dsmcFoam* and the future hypersonic OpenFOAM CFD solver within the same software suite.

In addition, the new two-temperature CFD solver should be an answer to Maicke and Majdalani's discussion on state-of-the-art hypersonic code accessibility [42], *i.e.*, the code should be posted open-source upon completion of this work and it should be relatively easy to use. To address this, a suitable OpenFOAM CFD solver, *rhoCentral-Foam*, has first been identified and assessed. This solver was created by Greenshields *et al.* [67] to resolve supersonic flows, making use of central-upwind interpolation schemes of Kurganov, Noelle and Petrova [68]. Basic chemistry features have then been added to *rhoCentralFoam* by incorporating parts of the solver *reactingFoam*, an OpenFOAM solver dealing with subsonic combustion. The newly blended code has been given the name *hyFoam* and the two-temperature solver that will share the same foundations will be called *hy2Foam*. Therefore, it is foreseen that little time should be needed for

---

[2]COOLFluiD and Eilmer3 are coded in C++ while the OpenFOAM solver *dsmcFoam* is coded in what is regularly called "OpenFOAM C++"

experienced *rhoCentralFoam* users to grasp the functioning of *hyFoam* and *hy2Foam*.

1.6   Dissertation overview

Chapter 2 addresses the state-of-the-art numerical procedures that have been implemented in *hy2Foam* to solve hypervelocity flow-fields in near-thermal equilibrium. This Chapter then describes the DSMC method as implemented in the *dsmcFoam* code and particular emphasis is set on the QK chemistry framework.

Chapter 3 aims at demonstrating the correct implementation of the CFD features presented in Chapter 2. Zero-dimensional adiabatic heat baths are reviewed at length considering the contributions of competing mechanisms in isolation. Multi-dimensional case scenarios of progressive complexity are then considered. The verification/validation process is supported by comparisons with data from the literature, results from the CFD solver LeMANS and the DSMC code *dsmcFoam*.

Chapter 4 exploits the combined DSMC and CFD capabilities of *dsmcFoam+* and *hyFoam* to address the problem of chemical rate constants modelling during the Earth atmosphere re-entry. *dsmcFoam+* QK chemistry framework allows the determination of the full set of 116 chemical rate constants without relying on any macroscopic data. They are derived therein and tabulated in Appendix C. Chapter 4 ends with recommendations.

Chapter 5 reports the key findings, the future areas of work and the perspectives opened up by this research.

Chapter 2

Computational Methods

2.1 Conventional computational fluid dynamics

This section describes the state-of-the-art numerical procedures that have been implemented in *hy2Foam* to solve hypervelocity flow-fields in near-thermal equilibrium. Section 2.1.1 recalls the non-equilibrium Navier-Stokes-Fourier (NSF) equations that are used in the framework of a two-temperature CFD model for a weakly-ionized flow. The different variables appearing in these equations are detailed in the subsequent sections. Transport quantities are shown in Section 2.1.2, the mixing rules employed in this thesis are described in Section 2.1.3, while mass diffusion models are presented in Section 2.1.4. Energy transfers between the different energy modes and finite-rate chemistry modelling are then addressed in Sections 2.1.5 and 2.1.6 with emphasis placed on chemistry-vibration coupling. Finally, numerical schemes and details about the boundary conditions used in *hy2Foam* are given in Section 2.1.8.

2.1.1 Non-equilibrium Navier-Stokes-Fourier equations

The computation of transient hypersonic reacting flows in the continuum regime traditionally employs the non-equilibrium NSF equations. These are shown in Eq. 2.1 in flux-divergence form using a Cartesian coordinate system for a mixture composed of N_s species, including N_m molecules. The continuity equation, the N_s species transport and

reaction equations[1], the momentum equations, the N_m vibrational energy equations, and the total energy equation can be written as [15]

$$\frac{\partial \mathcal{U}}{\partial t} + \frac{\partial \left(\mathcal{F}_{i,inv} - \mathcal{F}_{i,vis} \right)}{\partial x_i} = \dot{\mathcal{W}} \tag{2.1}$$

The vector of conserved quantities, $\mathcal{U}$, is defined as

$$\mathcal{U} = (\rho, \ \rho_s, \ \rho u, \ \rho v, \ \rho w, \ E_{ve,m}, \ E)^T \qquad s \in N_s \, , \ m \in N_m \tag{2.2}$$

u, v, and w are the components of the velocity vector. ρ is the mass density of the fluid and ρ_s is the partial density of species s. The flux vectors are split into inviscid and viscous contributions and are written as follows

$$\mathcal{F}_{i,inv} = \begin{pmatrix} \rho u_i \\ \rho_s u_i \\ \rho u_i\, u + \delta_{i1} p \\ \rho u_i\, v + \delta_{i2} p \\ \rho u_i\, w + \delta_{i3} p \\ E_{ve,m}\, u_i \\ (E + p) u_i \end{pmatrix} \tag{2.3}$$

and

$$\mathcal{F}_{i,vis} = \begin{pmatrix} 0 \\ -\mathcal{J}_{s,i} \\ \tau_{i1} \\ \tau_{i2} \\ \tau_{i3} \\ -q_{ve,i,m} - e_{ve,m}\, \mathcal{J}_{m,i} \\ \tau_{ij} u^j - q_{tr,i} - q_{ve,i} - \sum_{r \neq e} h_r \mathcal{J}_{r,i} \end{pmatrix} \tag{2.4}$$

where the index i refers to one of the three dimensions of space and δ is the Kro-

---

[1]Both total and all individual species continuity equations are solved for robustness as explained in [69]. However, it is possible to solve $N_s - 1$ species transport and reaction equations as well.

necker delta. E and $E_{ve,m}$ represent, respectively, the total energy and the total vibro-electronic energy for molecule m. In the remainder of the thesis, the index tr denotes the trans-rotational energy mode, ve the vibro-electronic energy mode and e the electron energy mode. h_s is the enthalpy per unit mass of species s, while the pressure, p, is recovered from the partial pressures using Dalton's law

$$p = \sum_{s \neq e} p_s + p_e = \sum_{s \neq e} \left(\rho_s \, R_s \, T_{tr} \right) + \rho_e \, R_e \, T_e \tag{2.5}$$

where R_s is the specific gas constant for species s.

It should be noted that no additional vibro-electronic energy equations are solved for ions but instead, species are grouped into energy pools and the vibro-electronic temperature of an ion is forced to follow the vibro-electronic temperature of the non-ionized molecule. Hence, $T_{ve,\mathrm{N}_2^+} = T_{ve,\mathrm{N}_2}$ for example. The atomic temperature is given a similar treatment should the electronic energy be included into the calculations: their vibro-electronic temperature is set to the undissociated molecule vibro-electronic temperature. For instance,

$$
\begin{aligned}
T_{ve,\mathrm{N}} &= T_{ve,\mathrm{N}_2} \quad \text{with inclusion of the electronic energy} \\
T_{ve,\mathrm{N}} &= 0 \qquad\quad \text{otherwise}
\end{aligned}
\tag{2.6}
$$

Moreover, the electron temperature is set to the vibro-electronic temperature of a reference particle and $T_e = T_{ve,\mathrm{ref}}$.

In Eq. 2.4, τ_{ij} represent the components of the viscous stress tensor which can be written as follows

$$\tau_{ij} = \mu \left(\frac{\partial u_i}{\partial x_j} + \frac{\partial u_j}{\partial x_i} \right) + (\lambda + \mu_b) \frac{\partial u_k}{\partial x_k} \, \delta_{ij} \tag{2.7}$$

where μ is the shear viscosity, λ is the second viscosity coefficient, and μ_b is the bulk viscosity. Unless otherwise stated, this work assume that Stokes' hypothesis is valid, namely that $\mu_b = 0$ and that the shear and second viscosity are not independent quantities but given by the relation $\lambda = -\frac{2}{3}\mu$. The validity of this hypothesis for compressible flows has however been questioned and it is in fact only valid for a dilute monatomic gas [70].

The spatial components of the heat conduction vector are assumed to follow Fourier's law

$$q_{tr,i} = -\kappa_{tr} \frac{\partial T_{tr}}{\partial x_i} \tag{2.8}$$

where κ_{tr} is the mixture thermal conductivity and

$$q_{ve,i} = \sum_s q_{ve,i,s} = \sum_s -\kappa_{ve,s} \frac{\partial T_{ve,s}}{\partial x_i} \quad \text{for } s \in N_s \tag{2.9}$$

Finally, the source term vector, $\dot{\boldsymbol{\mathcal{W}}}$, is written as

$$\dot{\boldsymbol{\mathcal{W}}} = \left(0, \ \dot{\omega}_s, \ 0, \ 0, \ 0, \ \dot{\omega}_{v,m}, \ 0\right)^T \tag{2.10}$$

where $\dot{\omega}_s$ is the net mass production of species s and $\dot{\omega}_{v,m}$, for $m \in N_m$, is defined as follows

$$
\begin{aligned}
\dot{\omega}_{v,m} &= Q_{m,V-T} + Q_{m,V-V} + Q_{m,C-V} + Q_{m,e-V} \quad \text{if } m \text{ is not the reference} \\
&\qquad\qquad\qquad\qquad\qquad\qquad\qquad\qquad\qquad\qquad \text{particle for } e^- \\
&= Q_{m,V-T} + Q_{m,V-V} + Q_{m,C-V} + Q_{m,e-V} \\
&\quad + Q_{h-e} + Q_{e-i} + \boldsymbol{U} \cdot \nabla p_e \quad \text{otherwise}
\end{aligned} \tag{2.11}
$$

where $\boldsymbol{U}$ represents the velocity vector. The meaning of the different vibrational source terms that appear in Eq. 2.11 is given in Section 2.1.5.

The NSF equations presented in this paragraph correspond to a two-temperature CFD model with multiple vibrational energy pools. A simpler approach would consist in writing a single vibrational equation as in Eq. 2.12.

$$
\frac{\partial E_{ve}}{\partial t} + \frac{\partial \left(E_{ve}\, u_i + q_{ve,i} + \sum_{r \neq e} e_{ve,r} \mathcal{J}_{r,i} \right)}{\partial x_i} = \sum_{r \neq e} \left(Q_{r,V-T} + Q_{r,C-V} \right)
$$
$$
+ Q_{h-e} + Q_{e-i} + \boldsymbol{U} \cdot \nabla p_e \quad r \in N_s \tag{2.12}
$$

In most cases, the vibrational energy pools of the different molecules composing the gas mixture are tightly coupled such that a single vibrational energy equation to represent the system should suffice. However, the initial method appears to be interesting from a coding point of view because it facilitates possible extensions of this work (*i.e.*, implementation of the electron energy equation) and it offers a direct correspondence between the CFD and DSMC vibrational outputs. Ultimately, both formulations have been implemented.

2.1.2   Transport quantities

In *hy2Foam*, the species shear viscosities can be considered as temperature-independent, or either set to follow a power law or Blottner's curve fits [71]. The corresponding equations for these two models are shown in Equations 2.13 and 2.15, respectively

$$\mu_s = \mu_{\text{ref},s} \times \left(\frac{T_{tr}}{T_{\text{ref}}} \right)^{\omega_s} \qquad \text{for } s \in N_s \tag{2.13}$$

with

$$\mu_{\text{ref},s} = \frac{15\sqrt{\pi m_s\, k_B\, T_{\text{ref}}}}{2\pi\, d_{\text{ref},s}^2\,(5 - 2\omega_s)(7 - 2\omega_s)} \tag{2.14}$$

and

$$\mu_s = 0.1 \times exp\left((A_{B,s}\, ln(T_{tr}) + B_{B,s})\, ln(T_{tr}) + C_{B,s} \right) \qquad \text{for } s \in N_s \tag{2.15}$$

where ω_s is the temperature coefficient of viscosity for species s, k_B is Boltzmann's constant and T_{ref} is a reference temperature taken as 273 K. $m_s = \mathcal{M}_s/N_A$ represents the mass of a single particle of s with N_A being Avogadro's constant and $\mathcal{M}_s$ the species molecular weight whose value can be found in Appendix A. $A_{B,s}$, $B_{B,s}$ and $C_{B,s}$ are coefficients in the Blottner equation for shear viscosity. These parameters are also outlined in Appendix A.

The thermal diffusivities $\kappa_{tr,s}$ and $\kappa_{ve,s}$ can be considered as temperature-independent, or set to follow Eucken's relation [15, 70] that writes

$$\kappa_{tr,s} = \frac{5}{2}\,\mu_s\,Cv_{t,s} + \mu_s\,Cv_{r,s} \tag{2.16}$$

for the trans-rotational mode and

$$\kappa_{ve,s} = 1.2\,\mu_s\,Cv_{ve,s} \tag{2.17}$$

for the vibro-electronic counterpart. Cv is the heat capacity at constant volume and it can be split into the contributions of the different energy modes as shown later in Eq. 2.43 - 2.47. The coefficient 1.2 in Eq. 2.17 is derived from kinetic theory for hard-sphere particles.

Transport properties can also be calculated using collision cross-section data obtained from Gupta's curve fits [72, 73]. Unlike Blottner's and Eucken's formalae, Gupta's approach is said to be more physically accurate at temperatures greater than 10,000 K and in weakly-ionized environments [74]. Its implementation in *hy2Foam* is an ongoing work.

2.1.3   Mixing rules

Mixture quantities are recovered from species quantities using a mixing rule. The Wilke [75], and Armaly and Sutton [76] mixing rules are widely used in the field of hypersonics and have been implemented in *hy2Foam*. Wilke's mixing rule for viscosity, that is a simplification of the full first-order Chapman-Enskog relation [77], can be written as

$$\mu = \sum_s \frac{\mu_s\,X_s}{\phi_s} \qquad \text{for } s \in N_s \tag{2.18}$$

where X is the molar-fraction and ϕ_s is a scaling factor defined as

$$\phi_s = X_s + \sum_{r \neq s} X_r \left[1 + \sqrt{\frac{\mu_s}{\mu_r}}\left(\frac{\mathcal{M}_r}{\mathcal{M}_s}\right)^{1/4}\right]^2 \left[\sqrt{8\left(1 + \frac{\mathcal{M}_s}{\mathcal{M}_r}\right)}\right]^{-1} \text{for } r \in N_s \tag{2.19}$$

and a similar formula can be applied to thermal diffusivity. The use of Wilke's mixing rule is limited to the study of neutral gases at moderate atmospheric entry velocity -or

moderate temperatures below 10,000 K- as it was shown in Palmer and Wright's review to give poor results for ionized gases outwith this temperature range [74].

The Armaly and Sutton mixing rule [76] mitigates this issue and has shown to give a more satisfactory approximation of the multi-component viscosity method solution for ionized gases for barely no additional computational cost and is thus recommended by Palmer and Wright [74]. The scaling factor ϕ_s in Eq. 2.18 now takes the following form

$$
\begin{aligned}
\phi_s \;=\;\; & X_s + \sum_{r \neq s} X_r \left[\frac{5}{3 \mathscr{A}_{sr}^*} + \frac{\mathcal{M}_r}{\mathcal{M}_s} \right] \left[1 + \frac{\mathcal{M}_r}{\mathcal{M}_s} \right]^{-1} \left[\mathscr{F}_{sr} + \mathscr{B}_{sr} \sqrt{\frac{\mu_s}{\mu_r}} \left(\frac{\mathcal{M}_r}{\mathcal{M}_s} \right)^{1/4} \right]^2 \\
& \times \left[\sqrt{ 8 \left(1 + \frac{\mathcal{M}_s}{\mathcal{M}_r} \right) } \right]^{-1} \text{ for } r \in N_s
\end{aligned}
$$

(2.20)

where quantities $\mathscr{A}^*$, $\mathscr{B}$, and $\mathscr{F}$ depend on the type of particle interaction. The parameter $\mathscr{F}$ is set equal to 1 for all interactions while the quantity $\mathscr{B}$ has the value 0.78 for neutral–neutral collisions, 0.15 for neutral–ion interactions, 0.2 for neutral–electrons collisions, and 1.0 for all other types of interaction. Finally, the parameter $\mathscr{A}^*$ is equal to 1.25 for all interactions except the one of an atom with its own ion. In this latter case, $\mathscr{A}^* = 1.1$ in the uncorrected form of the Armaly and Sutton mixing rule and 0.21 in the corrected form [74]. Both uncorrected and corrected formulations are available in *hy2Foam*.

2.1.4   Mass diffusion

The diffusion fluxes, $\mathcal{J}_{s,i}$, are governed by the modified Fick's law, which ensures that the sum of the diffusion mass fluxes is zero [78]

$$
\mathcal{J}_{s,i} = \mathcal{I}_{s,i} - Y_s \sum_{r \neq e} I_{r,i} \quad \text{ for } s,\, r \in N_s \setminus \{e^-\}
$$

(2.21)

with

$$
\mathcal{I}_{s,i} = -\rho \, \mathcal{D}_s \, \frac{\partial Y_s}{\partial x_i}
$$

(2.22)

and

$$\mathcal{J}_{e,i} = \mathcal{M}_e \sum_{r \neq e} \frac{\mathfrak{C}_r \times \mathcal{J}_{r,i}}{\mathcal{M}_r} \tag{2.23}$$

for electrons to ensure charge neutrality of the flow. Y is the mass-fraction, $\mathfrak{C}_r$ represents the charge of species r, and $\mathcal{D}_s$ is the effective diffusion coefficient of species s in the mixture. A simple approach to model the effective diffusion coefficient may be adopted for relatively low-speed case scenarios. The Lewis number model is widely-applied and the assumption is made that the effective diffusion coefficient is identical for all neutral particles, and double of that of neutral particles for charged particles due to ambipolar diffusion, such that

$$
\begin{aligned}
\mathcal{D}_s \;\; = \;\; \mathcal{D} \;\; &= \;\; \frac{\kappa_{tr}\,Le}{\rho\,Cp_{tr}} \qquad \text{for neutral particles} \\
&= \;\; 2\,\mathcal{D} \qquad\qquad\;\; \text{for charged particles}
\end{aligned}
\tag{2.24}
$$

where Le is the Lewis number and Cp_{tr} stands for the mixture heat capacity at constant pressure for the trans-rotational mode as defined in Eq. 2.49. This model works well when the flow is composed of species having similar diffusion properties (as is the case for the N_2 and O_2 molecules for example). Conversely, it was shown to fail in capturing the correct mixture composition and surface heat flux, when compared to the solution given by the Stephan-Maxwell iterative method, at entry velocities greater than 8 km s $^{-1}$ [79]. It is thus not appropriate for ionised flow.

Another approach consists in writing the effective diffusion coefficient in function of the binary diffusion coefficients, $\mathcal{D}_{s,r}$, as follows [78]

$$\mathcal{D}_s = (1 - X_s) \left(\sum_{r \neq s} \frac{X_r}{\mathcal{D}_{s,r}} \right)^{-1} \qquad \text{for } s,\, r \in N_s \setminus \{e^-\} \tag{2.25}$$

and to employ the complete first Chapman-Enskog approximation [77] to evaluate $\mathcal{D}_{s,r}$. Setting

$$\mathcal{D}_{s,r} = \frac{\overline{\mathcal{D}}_{s,r}}{p} \tag{2.26}$$

with the pressure expressed in atmospheres, Gupta [72] operated a curve-fit for $\overline{\mathcal{D}}_{s,r}$ obtaining:

$$\overline{\mathcal{D}}_{s,r} = e^{D_D} \, T^{\left[A_D \, (lnT)^2 + B_D ln(T) + C_D\right]} \tag{2.27}$$

where A_D, B_D, C_D and D_D are constants that differ for each pair of species (s, r) and that can be found in Table VI in Ref. [72]. The expression for $\overline{\mathcal{D}}_{s,r}$ presented in Eq. 2.27 is valid for an electron pressure, p_e, equal to 1 atm and a correction for non neutral–neutral collisions is also provided in this reference when $p_e \neq 1$ atm.

The binary diffusion coefficients in Eq. 2.25 may also be modelled using collision terms $\Delta_{s,r}^{(1)}$ as [80]

$$\mathcal{D}_{s,r} = \frac{k_B \, T_{tr}}{p \, \Delta_{s,r}^{(1)}(T_{tr})} \quad \text{for } s, r \in N_s \setminus \{e^-\} \tag{2.28}$$

for heavy-particle interactions and

$$\mathcal{D}_{e,r} = \frac{k_B \, T_e}{p \, \Delta_{e,r}^{(1)}(T_e)} \quad \text{for } r \in N_s \setminus \{e^-\} \tag{2.29}$$

for heavy-particle – electrons interactions. $\Delta_{s,r}^{(1)}$ is a function of a temperature T that is either T_{tr} or T_e, such that

$$\Delta_{s,r}^{(1)}(T) = \frac{8}{3} \sqrt{\frac{2 \, \mathcal{M}_{s,r}}{\pi \, \mathcal{R} \, T}} \, \pi \, \bar{\Omega}_{s,r}^{(1,1)}(T) \quad \text{for } s \in N_s \text{ and } r \in N_s \setminus \{e^-\} \tag{2.30}$$

where $\mathcal{R}$ is the universal gas constant and the reduced molecular weight of species s and r, $\mathcal{M}_{s,r}$, is defined as

$$\mathcal{M}_{s,r} = \frac{\mathcal{M}_s \, \mathcal{M}_r}{\mathcal{M}_s + \mathcal{M}_r} \tag{2.31}$$

$\pi \, \bar{\Omega}_{s,r}^{(1,1)}$ represents the collision cross-sections (in m^2) which, in the case of neutral–neutral collisions, can be curve-fitted in a similar manner to as Eq. 2.27 such that [72]

$$\pi \, \bar{\Omega}_{s,r}^{(1,1)}(T) = e^{D_{\bar{\Omega}(1,1)}} \, T^{\left[A_{\bar{\Omega}(1,1)} \, (lnT)^2 + B_{\bar{\Omega}(1,1)} ln(T) + C_{\bar{\Omega}(1,1)}\right]} \times 10^{-20} \tag{2.32}$$

where $A_{\bar{\Omega}(1,1)}$, $B_{\bar{\Omega}(1,1)}$, $C_{\bar{\Omega}(1,1)}$ and $D_{\bar{\Omega}(1,1)}$ are collision-specific constants. The values used in this work are provided in Ref. [73]. For other interaction types, the reader is

referred [72] for further detail about the calculation of collision cross-sections.

Stephani derived an expression for binary collision integrals of VHS particles (see Appendix C in Ref. [81]) that follows the form given by Chapman and Cowling [77]. For neutral–neutral interactions, Stephani firstly wrote the binary diffusion coefficients as (see Eq. (4.4) in [81])

$$\mathcal{D}_{s,r} = \frac{3k_B\,T_{tr}}{16 n_{\mathrm{mix}}\,\mathfrak{m}_{s,r}\,\Omega_{s,r}^{(1,1)}(T_{tr})} \tag{2.33}$$

where n_{mix} is the mixture number density, $\mathfrak{m}_{s,r}$ represents the reduced mass defined as the ratio of the reduced molecular weight to Avogadro's number, and $\Omega_{s,r}^{(1,1)}$ is the binary collision integral (in $\mathrm{m}^3\ \mathrm{s}^{-1}$) given by

$$\Omega_{s,r}^{(1,1)}(T) = \frac{\pi}{2}\,d_{\mathrm{ref}}^2\sqrt{\frac{k_B\,T}{2\pi\,\mathfrak{m}_{s,r}}}\left(\frac{T_{\mathrm{ref}}}{T}\right)^{\omega-0.5}\frac{\Gamma(7/2-\omega)}{\Gamma(5/2-\omega)} \tag{2.34}$$

where Γ is the gamma function, and d_{ref}, T_{ref}, and ω are the reference diametre, the reference temperature and the temperature coefficient of viscosity of the pair $(s,\,r)$, respectively, as defined as the arithmetic average of these quantities between species s and r. Re-arranging Eq. 2.28 - 2.32, one can make the following analogy between Gupta's curve fit for $\pi\,\bar{\Omega}^{(1,1)}$ and Stephani's development:

$$\pi\,\bar{\Omega}_{s,r}^{(1,1)}\Big|_{\mathrm{curve\ fit}} \equiv \frac{d_{\mathrm{ref}}^2}{2}\left(\frac{T_{\mathrm{ref}}}{T}\right)^{\omega-0.5}\frac{\Gamma(7/2-\omega)}{\Gamma(5/2-\omega)} \tag{2.35}$$

The performance of the models presented in Eq. 2.24, 2.26, 2.28 and 2.33 will be evaluated in next Chapter for a non-homogeneous Fourier flow.

2.1.5   Energy transfers

The decomposition of the total energy, E, as shown in Eq. 2.36 allows the isolation of different energy pools, each of them being described by a specific temperature and exchanging energy with the other pools.

$$E \quad = \quad \frac{1}{2}\rho \sum_i u_i^2 \quad + \quad \sum_{s \neq e} E_{t,s} \quad + \quad \sum_{s \neq e} E_{r,s} \quad + \quad \sum_{s \neq e} E_{v,s} \quad + \quad \sum_{s \neq e} E_{el,s}$$
$$+ \quad E_e \quad + \quad \sum_{s \neq e} \rho_s h_s^\circ \tag{2.36}$$

In order of appearance in Eq. 2.36 are the kinetic, translational (index t), rotational (r), vibrational (v), electronic (el), electron (e), and chemical energies. u_i are the spatial components of the velocity vector and h_s° is the standard enthalpy of formation of species s. The relation between the total energy of a specific mode and the energy per unit mass of species s is given in Eq. 2.37 for the vibrational energy mode

$$E_v = \sum_{s \neq e} E_{v,s} = \sum_{s \neq e} \rho_s \, e_{v,s} \tag{2.37}$$

and the different energies per unit mass of species are detailed for each mode in Eq. 2.38 - 2.42

$$e_{t,s} = \frac{3}{2} \, R_s \, T_t \tag{2.38}$$

$$e_{r,s} = R_s \, T_r \tag{2.39}$$

$$e_{v,s} = R_s \, \frac{\theta_{v,s}}{exp\left(\frac{\theta_{v,s}}{T_{v,s}}\right) - 1} \tag{2.40}$$

$$e_{el,s} = R_s \, \frac{\displaystyle\sum_{i \neq 0} g_{i,s} \, \theta_{el,i,s} \, exp\left(-\theta_{el,i,s}/T_{el,s}\right)}{\displaystyle\sum_{i} g_{i,s} \, exp\left(-\theta_{el,i,s}/T_{el,s}\right)} \tag{2.41}$$

$$e_e = R_e \, T_e \tag{2.42}$$

at the exception of atoms and atom ions for which $e_{r,s}$ and $e_{v,s}$ are zero. The simple harmonic oscillator model [47] is utilized for the vibrational mode with $\theta_{v,s}$ being the characteristic vibrational temperature for species s. $\theta_{el,i,s}$ and $g_{i,s}$ are the characteristic

electronic temperature and the degeneracy degree of a given electronic level i for species s, respectively.

From Eq. 2.38 - 2.42, the heat capacity at constant volume of a given energy mode can be derived as follows

$$Cv_{t,s} = \frac{3}{2} R_s \tag{2.43}$$

$$Cv_{r,s} = R_s \tag{2.44}$$

$$Cv_{v,s} = R_s \frac{(\theta_{v,s}/T_{v,s})^2 \; exp\left(\frac{\theta_{v,s}}{T_{v,s}}\right)}{\left(exp\left(\frac{\theta_{v,s}}{T_{v,s}}\right) - 1\right)^2} \tag{2.45}$$

$$
Cv_{el,s} = R_s \frac{\sum\limits_{i\neq 0} g_{i,s} \; (\theta_{el,i,s}/T_{el,s})^2 \; exp\left(-\theta_{el,i,s}/T_{el,s}\right)}{\sum\limits_{i} g_{i,s} \; exp\left(-\theta_{el,i,s}/T_{el,s}\right)}
$$
$$
- \frac{\left[\sum\limits_{i\neq 0} g_{i,s} \, \theta_{el,i,s} \, exp\left(-\theta_{el,i,s}/T_{el,s}\right)\right] \times \left[\sum\limits_{i\neq 0} \frac{g_{i,s} \, \theta_{el,i,s}}{T_{el,s}^2} \, exp\left(-\theta_{el,i,s}/T_{el,s}\right)\right]}{\left(\sum\limits_{i} g_{i,s} \; exp\left(-\theta_{el,i,s}/T_{el,s}\right)\right)^2} \tag{2.46}
$$

$$Cv_e = R_e \tag{2.47}$$

at the exception once again of atoms and atom ions for which $Cv_{r,s}$ and $Cv_{v,s}$ are zero. Finally, the heat capacity at constant pressure for the translational mode is defined as

$$Cp_{t,s} = Cv_{t,s} + R_s \tag{2.48}$$

from which the expression for the trans-rotational Cp can naturally be derived as being

$$Cp_{tr,s} = Cp_{t,s} + Cv_{r,s} \tag{2.49}$$

Two-temperature formulation

The relaxation towards thermal equilibrium of the translational and rotational energy modes is usually achieved within a small number of particle collision events [47]. In a two-temperature formulation, the translational and rotational temperatures are thus considered to be equilibrated at all times and equate the trans-rotational temperature, denoted by T_{tr}. Similarly, electron and electronic energy modes are assumed to be in equilibrium with the vibrational energy mode [47]. Hence, all three temperatures are forced to follow the vibrational-electron-electronic temperature designated by T_{ve} in a single vibrational temperature formulation. Considering a multiple vibrational temperature model, which is precisely the focus of this work, each molecule has its own vibro-electronic temperature, $T_{ve,m}$. The two-temperature model formulation adopted in *hy2Foam* thus consists in rewriting Eq. 2.36 as follows

$$E \;=\; \frac{1}{2}\rho \sum_i u_i^2 \;+\; E_{tr} \;+\; \sum_{s \neq e} E_{ve,s} \;+\; E_e \;+\; \sum_{s \neq e} \rho_s h_s^{\circ} \tag{2.50}$$

with

$$E_{tr} = E_t + E_r \tag{2.51}$$

and

$$E_{ve,s} = E_{v,s} + E_{el,s} \tag{2.52}$$

Overall temperature calculation

For verification purposes in particular, it is useful to evaluate the temperature that the gas particles actually feel. This temperature is considered as the overall temperature, T_{ov}, and can be determined considering the different molecular temperatures and their respective degrees of freedom. This may be written as

$$T_{ov} = \frac{\sum\limits_{s\neq e}\left[\,X_s\,(\zeta_{t,s}+\zeta_{r,s})\,T_{tr}\,\right] + \sum\limits_{s\neq e}\left[\,X_s\,(\zeta_{v,s}+\zeta_{el,s})\,T_{ve,s}\,\right] + X_e\,\zeta_e\,T_e}{\sum\limits_{s\neq e}\left[\,X_s\,(\zeta_{t,s}+\zeta_{r,s}+\zeta_{v,s}+\zeta_{el,s})\,\right] + X_e\,\zeta_e} \tag{2.53}$$

ζ is the number of degrees of freedom in relation to one specific energy mode. Both translational and rotational energy modes are supposed to be fully excited; therefore, three degrees of freedom are associated with the translational mode and $\zeta_{t,s} = 3$. Neglecting the degree of freedom of rotation along the nuclear axis for diatomic particles, two degrees of freedom are allocated to the rotational energy mode and $\zeta_{r,s} = 2$. For the vibrational and electronic modes, $\zeta_{v,s}$ and $\zeta_{el,s}$ are derived from the following equations

$$\zeta_{v,s} = \frac{2\,e_{v,s}(T_{ve,s})}{R_s\,T_{ve,s}} \tag{2.54}$$

and

$$\zeta_{el,s} = \frac{2\,e_{el,s}(T_{ve,s})}{R_s\,T_{ve,s}} \tag{2.55}$$

The vibrational source terms introduced into the NSF equations in Section 2.1.1 are now described in sequence.

Vibrational-translational energy transfer

The energy exchange between the trans-rotational and the vibro-electronic energy modes (V–T), designated by $Q_{m,V-T}$, is dictated by the Landau-Teller equation [82] and may be written as

$$Q_{m,V-T} = \rho_m\,\frac{\partial e_{ve,m}(T_{ve,m})}{\partial t} = \rho_m\,\frac{e_{ve,m}(T_{tr}) - e_{ve,m}(T_{ve,m})}{\tau_{m,V-T}} \qquad m \in N_m \tag{2.56}$$

where $\tau_{m,V-T}$ is the molar-averaged V–T relaxation time. This quantity is evaluated as the summation of the Millikan and White correlation and Park's correction factor, and later denoted as MWP. Millikan and White [83] introduced a semi-empirical correlation to evaluate the V–T relaxation time for individual or mixture of species. The

temperature range of validity of the proposed formula is from 300 K up to 8000 K. Within this range, the estimation does not deviate from experimental measurements by more than a factor of 5. Park added a correction factor to the Millikan-White formula [14] to take into account the inaccurate estimation of the collision cross-section at high temperatures. For a mixture, this produces to

$$\tau_{m,V-T} = \frac{\sum\limits_{s \neq e} X_s}{\sum\limits_{s \neq e} X_s / \tau_{m-s,V-T}} \qquad m \in N_m \tag{2.57}$$

where the interspecies relaxation time, $\tau_{m-s,V-T}$, is expressed as the sum of the Millikan and White (MW) and Park (P) contributions

$$\tau_{m-s,V-T} = \tau_{m-s,V-T}^{MW} + \tau_{m-s,V-T}^{P} \tag{2.58}$$

where firstly

$$\tau_{m-s,V-T}^{MW} = \frac{1}{p} \, exp \left[A_{m,s} \left(T_{tr}^{-1/3} - B_{m,s} \right) - 18.42 \right] \quad \text{with } p \text{ in atm} \tag{2.59}$$

Coefficients $A_{m,s}$ and $B_{m,s}$ can either be calculated following Equations 2.60 and 2.61 or be read from a table.

$$A_{m,s} = 1.16 \times 10^{-3} \, \sqrt{\mathcal{M}_{m,s}} \, \theta_{v,m}^{4/3} \tag{2.60}$$

$$B_{m,s} = 0.015 \, \mathcal{M}_{m,s}^{1/4} \tag{2.61}$$

$\mathcal{M}_{m,s}$ is the reduced molecular weight of species m and s as given by Eq. 2.31 with $\mathcal{M}_m$ the molecular weight of species m in g/mol. The tabulated values of $A_{m,s}$ and $B_{m,s}$ used in this thesis originates from the work of Park [7]. Secondly, Park's counterpart may be written as

$$\tau_{m-s,V-T}^{P} = \frac{1}{\bar{c}_m \, \sigma_{v,m} \, n_{m,s}} \tag{2.62}$$

where $n_{m,s}$ is the number density of the colliding pair (m, s), $\bar{c}_m$ represents the average

molecular speed, and $\sigma_{v,m}$ is the limited collision cross-section defined as follows

$$\bar{c}_m = \sqrt{\frac{8\,R_m\,T_{tr}}{\pi}} \tag{2.63}$$

and

$$\sigma_{v,m} = \sigma_m \left(\frac{50,000}{T_{tr}}\right)^2 \tag{2.64}$$

In the original formulation, σ_m is taken as $10^{-21}\ m^2$. In this thesis, σ_m is set to $3.0 \times 10^{-21}\ m^2$ for N_2, O_2, and NO [7].

The second V–T model tested in this work is the SSH theory named after Schwartz, Slawsky, and Herzfeld [84]. The coefficients of this latter model are taken from the work of Thivet [85] and a blended model is created with the MWP formulation for molecule-atom collisions.

Vibrational-vibrational energy transfer

Although the vibrational-vibrational (V–V) energy redistribution is known to play only a secondary role in vibrational energy exchange, vibrational energy pools of the different molecules are not always supposed to be tightly coupled. In the multi-vibrational temperature version of *hy2Foam*, the formulation that has been implemented to account for V–V energy transfer is the one of Knab *et al.* [86, 87]. The source term designated by $Q_{m,V-V}$ may be written as

$$
\begin{aligned}
Q_{m,V-V} \quad = \quad & \sum_{\substack{l \neq m \\ l \neq e}} N_A\,\sigma_{m,l}\,P_{m,l}\sqrt{\frac{8\,\mathcal{R}\,T_{tr}}{\pi\,\mathcal{M}_{m,l}}}\frac{\rho_l}{\mathcal{M}_l} \\
& \times \rho_m \left(e_{v,m}(T_{tr})\frac{e_{v,l}(T_{ve,l})}{e_{v,l}(T_{tr})} - e_{v,m}(T_{ve,m})\right) \quad m,\,l \in N_m
\end{aligned}
\tag{2.65}
$$

where $P_{m,l}$ represents the assessed exchange probability whose recommended value is a constant equal to 10^{-2} [88]. $\sigma_{m,l}$ is the collision cross-section of the pair $(m,\,l)$ based on the respective molecular diameters.

Energy transfers involving electrons

In Eq. 2.11, Q_{h-e}, $Q_{m,e-V}$, and Q_{e-i} stand for the energy exchange between free-electrons and heavy-particles, free-electrons and the vibrational mode, and the vibro-electronic energy removal due to electron impact ionization, respectively. These terms are assumed to be zero in this thesis. The term in $\boldsymbol{U} \cdot \nabla p_e$ represents an approximation to the work done on the electrons by the electric field induced by the electron pressure gradient [89].

Finally in Eq. 2.11, the vibro-electronic energy added or removed by chemical reactions to species m, and represented by $Q_{m,\,C-V}$, is modelled either with the Park TTv model or the CVDV model in *hy2Foam*. This is addressed in the following sub-section.

2.1.6   Chemical source terms

The law of mass action stipulates that the net source of chemical species s due to chemical reactions, previously denoted by $\dot{\omega}_s$, is computed as the sum of the reaction sources over the N_R reactions in which the species participates in. It is written as [90]

$$\dot{\omega}_s = \mathcal{M}_s \sum_{r=1}^{N_R} \left(\nu''_{s,r} - \nu'_{s,r} \right) \left[k_{f,r} \prod_{k=1}^{N_r} \left(\frac{\rho_k}{\mathcal{M}_k} \right)^{\nu'_{k,r}} - k_{b,r} \prod_{k=1}^{N_r} \left(\frac{\rho_k}{\mathcal{M}_k} \right)^{\nu''_{k,r}} \right] \qquad (2.66)$$

where $\nu'_{s,r}$ and $\nu''_{s,r}$ are the forward and backward stoichiometric coefficients of species s in the reaction r, and N_r is the number of species in reaction r.

The forward rate constant, k_f, is assumed to follow the (modified) Arrhenius law, and is thus given by

$$k_f \left(T_{c,f} \right) = A \times T_{c,f}^{\beta} \, exp \left(-\frac{T_a}{T_{c,f}} \right) \qquad (2.67)$$

where A is a pre-exponential factor, β is the temperature exponent, and T_a is the temperature of activation derived from the activation energy. $T_{c,f}$ is the controlling temperature of the forward reaction.

The relation giving the backward rate constant, k_b, writes as follows

$$k_b\left(T_{c,b}\right) = \frac{k_f\left(T_{c,b}\right)}{K_{eq}\left(T_{c,b}\right)} \tag{2.68}$$

where $T_{c,b}$ is the controlling temperature of the backward reaction. K_{eq} is the equilibrium constant for the reaction of interest and its evolution with temperature taken from experiments has been curve-fitted to produce [14]

$$K_{eq}\left(T_{c,b}\right) = exp\left(\frac{A_1\,T_{c,b}}{10^4} + A_2 + A_3\,ln\left(\frac{10^4}{T_{c,b}}\right) + \frac{A_4\,10^4}{T_{c,b}} + A_5\left(\frac{10^4}{T_{c,b}}\right)^2\right) \tag{2.69}$$

where coefficients $A_1 - A_5$ depend on the local mixture number density and are provided in Ref. [91]. Unless otherwise stated, chemical reactions throughout this thesis are considered to be irreversible to be in line with the *dsmcFoam* code.

Chemistry-vibration coupling

The Park TTv model   For a dissociation reaction, the controlling temperature is Park's temperature, defined as

$$T_P = T_{tr}^{\alpha_P} \times T_{ve}^{1-\alpha_P} \tag{2.70}$$

An exponent of 0.7 in favour of the trans-rotational temperature is commonly adopted [15]. Other controlling temperatures corresponding to the various types of reaction that may occur in hypersonic flows are also implemented in *hy2Foam* and are shown in Table 2.1.

Table 2.1: Controlling temperature depending on the type of the chemical reaction

Reaction Type	Forward, $T_{c,f}$	Backward, $T_{c,b}$
dissociation	T_P	T_{tr}
associative ionization	T_{tr}	T_e
electron impact dissociation	T_e	T_e
electron impact ionization	T_e	T_e
exchange	T_{tr}	T_{tr}
charge exchange	T_{tr}	T_{tr}

The vibro-electronic energy added or removed by chemical reactions to species m is translated into an additional source term to appear in the NSF equations as seen in Eq. 2.10. It takes the following form [89, 91]

$$Q_{m,\,C-V} = \dot{\omega}_m \left(D'_m + e_{el,m} \right) \qquad m \in N_m \tag{2.71}$$

The coefficient D'_m can either be determined from a non-preferential or a preferential model. The non-preferential model postulates that molecular creation and destruction take place at the average vibrational energy such that [91]

$$D'_m = e_{v,m} \tag{2.72}$$

whereas in the preferential model molecules at the higher vibrational energy states are more likely to undergo dissociation [92] and

$$D'_m = \alpha_m \times D_m \tag{2.73}$$

D_m is the dissociation potential of species m and it can be found in Appendix A. The fraction of the dissociation energy, α_m, is a constant usually taken as 0.3 [15]. However, heat bath DSMC studies from Holman and Boyd have shown that α_m follows a linear trend as a function of the translational temperature [93]. In *hy2Foam*, both non-preferential and preferential chemistry-vibration models are available for use and for the latter model, the choice is left between a constant and a linear fit with translational temperature for α_m.

The coupled vibration-dissociation-vibration model   The coupled vibration-dissociation-vibration (CVDV) model of Marrone and Treanor [94] is another popular model to describe the preferential energy removal from the upper vibrational energy states due to dissociation [92]. The forward rate constant introduced in Eq. 2.67 is amended as follows

$$k_f = \frac{Z(T_{tr})\, Z(T_{F,m})}{Z(T_{ve,m})\, Z(-U_m)} \times A\, T_{tr}^{\beta}\, exp \left(-\frac{T_a}{T_{tr}} \right) \tag{2.74}$$

where U_m is a factor defined as

$$U_m = \frac{D_m}{3\,R_m} \tag{2.75}$$

and $T_{F,m}$ is a modified temperature given by

$$T_{F,m}^{-1} = \frac{1}{T_{ve,m}} - \frac{1}{T_{tr}} - \frac{1}{U_m} \tag{2.76}$$

In Eq. 2.74, $Z(T)$ is the vibrational partition function for the particle m at temperature T computed as

$$Z(T) = \sum_{\alpha=0}^{\mathfrak{N}_m} exp\left(-\frac{\epsilon_{v,\alpha,m}}{k_B\,T}\right) \tag{2.77}$$

in which α is a positive integer and $\mathfrak{N}_m$ is a cut-off value for the number of vibrational levels considered for m. Using the simple harmonic oscillator model, the energy of the α-th vibrational level of the molecule m is given by

$$\epsilon_{v,\alpha,m} = \alpha\,k_B\,\theta_{v,m} \tag{2.78}$$

Introducing now

$$\bar{E}(T_{tr}, T_{ve,m}) = \frac{1}{Z(T_{F,m})} \sum_{\alpha=0}^{\mathfrak{N}_m} \epsilon_{v,\alpha,m}\,exp\left(-\frac{\epsilon_{v,\alpha,m}}{k_B\,T_{F,m}}\right) \tag{2.79}$$

and

$$\bar{E}(T_{tr}, T_{tr}) = \frac{1}{Z(-U_m)} \sum_{\alpha=0}^{\mathfrak{N}_m} \epsilon_{v,\alpha,m}\,exp\left(\frac{\epsilon_{v,\alpha,m}}{k_B\,U_m}\right) \tag{2.80}$$

and splitting the net source of chemical species into its forward and backward components, the CVDV chemistry-vibration source term eventually becomes

$$Q_{m,\,C-V} = \frac{1}{m_m}\left(\bar{E}(T_{tr}, T_{ve,m}) \times \dot{\omega}_{f,m} + \bar{E}(T_{tr}, T_{tr}) \times \dot{\omega}_{b,m}\right) \qquad m \in N_m \tag{2.81}$$

where $m_m = \mathcal{M}_m/N_A$ is the mass of one particle of species m.

2.1.7 Boundary conditions

In the continuum regime, the gas velocity and temperature in the vicinity of a wall are in equilibrium with the surface and no-slip boundary conditions are applied such that for a stationary wall

$$
\begin{aligned}
u_s &= 0 \\
T &= T_{\text{wall}}
\end{aligned}
\tag{2.82}
$$

where u_s is the tangential slip velocity and T_{wall} is the prescribed wall temperature.

As the local Knudsen number increases, the number of particle collision events becomes insufficient near the wall and slip boundary conditions are employed instead. In a coordinate system where x represents the direction tangential to the wall and n the normal to the wall pointing into the fluid, the Maxwell velocity slip boundary condition [95] is traditionally employed and can be expressed as

$$
u_s = A \frac{2-\sigma}{\sigma} \lambda \frac{\partial u}{\partial n} + \frac{3}{4} \frac{\mu}{\rho\, T_{tr}} \frac{\partial T_{tr}}{\partial x}
\tag{2.83}
$$

where A is a constant usually taken as $\sqrt{2/\pi}$ and σ is the tangential momentum accommodation coefficient [96]. Rarefaction effects translate into a gas temperature at the wall that is different from the prescribed wall value and this is usually handled by the Smoluchowski temperature jump boundary condition [97] that is given by the relation

$$
T = T_{\text{wall}} + \frac{2-\alpha}{\alpha} \frac{2\gamma}{(\gamma+1)\, Pr} \lambda \frac{\partial T}{\partial n}
\tag{2.84}
$$

where γ is the ratio of specific heats, $Pr = \dfrac{\mu\, Cp_{tr}}{\kappa_{tr|ve}}$ stands for the Prandtl number, and α is the thermal accommodation coefficient. In this work, it is assumed that both σ and α coefficients are equal to unity, *i.e.*, that the wall is fully diffusive.

Finally, all simulations in this thesis assume a non-catalytic wall in which the gas composition in the cell adjacent to the wall is imposed at the surface.

2.1.8   Numerical procedures

The *hy2Foam* solver uses the numerical procedures present in the official OpenFOAM application *rhoCentralFoam*. It is an implicit finite-volume, parallel, three-dimensional code that is also capable of simulating 2D and axisymmetric simulations on any mesh composed of polyhedral cells that have an arbitrary number of faces. The implementation performed by Greenshields *et al.* [67] has shown to be competitive with well-established methods such as a Roe solver with van Leer limiting and the piecewise parabolic method. In particular, similar predictions to a Roe solver were obtained for the separation region on a hypersonic flow over a double cone configuration. It has further been tested and assessed in [98] and has been shown to produce similar results to those given by the MISTRAL flow solver [99] and DLR's TAU code [34] for the study of a non-reacting hypersonic flow past a hollow cylinder in the continuum regime.

The first-order accurate Euler discretisation scheme is used for temporal derivatives. More elaborate schemes could be used for time integration instead but this does not constitute the core of the present work.

Convective fluxes are discretised using the second-order accurate central-upwind scheme of Kurganov, Noelle and Petrova (KNP) [67, 68], while diffusive fluxes are treated using central differences. The motivation of Greenshields *et al.* in implementing the KNP scheme lies in the fact that the method does not rely on the specific eigen-structure of the problem. Interpolation of values at cell centres to values at cell faces solely involves an owner cell and a neighbouring cell which makes this Jacobian-free approach inherently simple and adequate to engineering applications. The downside of the KNP scheme is its dissipative nature that may result in a less accurate prediction of near-wall effects as compared with notable schemes from the AUSM (Advection Upstream Splitting Method) family such as AUSM$^+$-up [100] and AUSMDV [101], and the HLLC (Harten–Lax-van Leer–Contact) Riemann solver [102]. It also necessitates superior mesh quality. Typically for hypersonic entry case scenarios, this translates into the need of a mesh that is aligned with the bow shock whenever possible.

After application of the Gauss's theorem to transform the integration of the convective flux over a control volume into a summation over the control volume faces, the flux at faces is split into two directions, outward (owner to neighbour, denoted with

the $+$ sign) and inward (neighbour to owner, denoted with the $-$ sign). The linearised expression for the product of the volumetric flux $\phi_f = \boldsymbol{S}_f \cdot \boldsymbol{U}_f$, where $\boldsymbol{S}_f$ is the vector area, by a tensor of any rank $\boldsymbol{\Psi}$ can be written as

$$\sum_f \phi_f \boldsymbol{\Psi}_f = \sum_f \left[\alpha_{\text{KNP}} \phi_{f+} \boldsymbol{\Psi}_{f+} + (1 - \alpha_{\text{KNP}}) \phi_{f-} \boldsymbol{\Psi}_{f-} + \omega_{f,\text{KNP}} \left(\boldsymbol{\Psi}_{f-} - \boldsymbol{\Psi}_{f+} \right) \right] \quad (2.85)$$

The central-upwind character of KNP follows from the calculation of the weighting coefficient α_{KNP} that uses one-sided local speeds of propagation, $a_{f\pm} = \sqrt{\frac{Cp_{tr,mix}}{Cv_{tr,mix}} R_{mix} T_{tr,f\pm}}$, and acting as an upwind bias. Defining

$$\psi_{f\pm} = \max \left(a_{f\pm} |\boldsymbol{S}_f| \pm \phi_{f\pm}, \, a_{f\mp} |\boldsymbol{S}_f| \pm \phi_{f\mp}, 0 \right) \quad (2.86)$$

then

$$\alpha_{\text{KNP}} = \frac{\psi_{f+}}{\psi_{f+} + \psi_{f-}} \quad (2.87)$$

In Eq. 2.85, ω_f is the diffusive volumetric flux given by

$$\omega_{f,\text{KNP}} = \alpha_{\text{KNP}} (1 - \alpha_{\text{KNP}}) \left(\psi_{f+} + \psi_{f-} \right) \quad (2.88)$$

Second-order face interpolation in the positive and negative directions is achieved using total variation diminishing (TVD) scheme with the van Leer limiter function. The reader is encouraged to consult the original work in [67] for the sake of completeness.

Parallel computing uses the public domain Open MPI implementation of the standard message passing interface (MPI). The domain decomposition technique employed by OpenFOAM uses the scotch method and thus the mesh and fields are broken into pieces and allocated to different processors, while attempting to minimise the number of processor boundaries [103].

Local time stepping (LTS), that is used to accelerate the convergence of a computation towards its steady-state solution, has been implemented in *hy2Foam* following the work done by Espinoza *et al.* [104].

2.2   The direct simulation Monte-Carlo method

The direct simulation Monte-Carlo (DSMC) method [12] is reviewed succinctly hereafter with emphasis on the models being used in *dsmcFoam* [44] and *dsmcFoam+* [49]. The DSMC method is a particle-based, stochastic numerical technique to model rarefied gas flows. It was initially proposed by Bird in the late 1960's and has now grown into one of the predominant numerical approaches to compute dilute gas flows. Typical applications span across the entire range of characteristic lengths, from the scale of the micro- or nanometer to that of the order of magnitude of meters [105].

DSMC instructs computational particles, also called simulators, to move and collide upon a computational grid. Each simulator corresponds to a very large number of physical particles. The DSMC method foundations lie on the classical kinetic theory and as such it is dictated by the assumption of molecular chaos. This implies that the gas particles mean free path is much larger than the range of intermolecular forces, that is about 10 times the diameter of the gas particles [9]. Consequently, the motion and collision routines can be executed in an uncoupled fashion provided the cell size and time-step are set correctly.

It has been proven that the DSMC method provides an exact solution to the Boltzmann equation when the number of simulated particles is increasing to infinity and when time-step and cell size are decreasing to zero [106]. Good DSMC practice dictates that the cell size must be a fraction of the mean free path and that every cell volume should contain no less than about 20 simulators. The time-step should be a fraction of the minimum between the mean collision time and mean residence time, that is defined as a estimation of the time spend by a particle in a grid cell.

Following the traditional DSMC algorithm sequentially, the domain is initially filled with particles that are randomly generated according to an equilibrium distribution function and boundary conditions are imposed. Simulators are then moved by a distance that corresponds to the current time-step and boundary interactions are also performed at this stage (see subsection 2.2.3). Indexing of the particles is updated and next is the treatment of particle collisions as detailed in subsection 2.2.1. Finally, the macroscopic flow variables are recovered from the microscopic state of particles by averaging quantities in each grid cell.

2.2.1   Collisions

There are various techniques for handling collisions probabilistically in DSMC and the one retained is the No Time Counter (NTC) [12, 107] model proposed by Bird. It first calculates the number of binary collisions within a grid cell and for a given time-step, prior to the execution of the collision procedure per say, which makes this model time efficient compared to other techniques. Then, pairs are randomly selected and tested following an acceptance-rejection routine until the number of collisions to occur is satisfied.

Collisions can either be elastic or inelastic and are described by the variable hard sphere (VHS) model [108]. Particles do not exchange momentum nor energy during an elastic collision. The description of the method employed for the computation of the post-collisional quantities is given in Ref. [47]. In the event of an inelastic collision, transfer of momentum and energy between the translational and internal modes can take place and thermal relaxation processes are discussed in the subsequent subsection on internal energy storage.

2.2.2   Internal energy

The equilibration rate of an internal energy mode with the translational mode is prescribed by a collision number, Z, that is defined as the average number of molecular collisions for an energy mode to reach equilibrium. In *dsmcFoam*, it is postulated that the vibrational energy of a particle can only assume discrete quantum levels [109, 110] that are equally-spaced, thus obeying to the harmonic oscillator model [47]. Relaxation of the vibrational mode is operated first using a serial application of the quantum Larsen-Borgnakke procedure [44, 46] in which the vibrational collision number is not constant but depends in particular on a quantized collision temperature. The procedure for the electronic mode is omitted because it will not be used in this thesis but it can be found in Ref. [49]. For the rotational energy mode at last, the standard Larsen-Borgnakke procedure is enforced and a rotational collision number value is chosen equal to 5 that is a good approximation for engineering problems [45].

2.2.3   Boundary conditions

Particles are inserted at the inflow patch and gets deleted whether they strike an inflow or outflow boundary. Two types of wall boundary conditions are considered, that are specular and fully diffuse reflections. A particle striking a specular wall reflects back with no change in energy and with an angle of departure that equals the angle of incidence. Conversely, fully diffuse reflection emits the particle from the surface with a temperature that is accommodated to the wall temperature and with velocity components that have no dependence on its incident velocity. The new internal energies and velocity components of the simulator are sampled from equilibrium distributions at the surface temperature.

2.2.4   Chemical reactions modelling

Among the number of chemistry models that were made available for use in a DSMC framework, the total collision energy (TCE) model introduced by Bird in 1979 [111] is one of the most popular. It employs equilibrium kinetic theory to translate Arrhenius rate coefficients, that are function of the macroscopic gas temperature, into collision probabilities, which are function of the collision energy at a microscopic level. An alternative chemical reaction procedure laid out by Bird in 2009, that has been adopted in *dsmcFoam* and *dsmcFoam+*, is the quantum-kinetic (QK) model [112]. Unlike TCE that relies on the availability of experimental data, the QK method is a molecular level chemistry model that presents the advantage of employing fundamental molecular properties and thus of relying on a limited number of macroscopic data [113]. Yet it is highly phenomenological in nature and may lead to computed rates that are outwith the range of uncertainty of the measured rates [114].

The different types of chemical reaction considered in the QK framework and that are relevant to the Earth atmospheric re-entry are detailed in the subsequent paragraphs. The development recalled below that is a synthesis of the work presented in Refs. [44, 47, 49, 114, 115] will be useful for the derivation of QK rates for a VHS gas in equilibrium as shown in Chapter 4.

For each collision event, an array is constructed to contain the probabilities associated with reactions that can potentially occur. After reviewing all possible reactions,

the array is sorted by decreasing probabilities and each of them are tested in sequence versus a randomly-generated number ranging between 0 and 1, and the reaction does occur if the reaction probability is greater than this number. If two probabilities are equal (which is the case for dissociation and ionization reactions), then the algorithm randomly decides which of the two reactions has the priority over the other. Once a reaction is accepted, this process is repeated with the remaining collision pairs.

Dissociation reactions

A dissociation reaction can be written as $AB + C \longrightarrow A + B + C$ where AB is a molecule formed of two atoms A and B, and C a reactant partner. In the case where C is an electron, the reaction is called electron impact dissociation. The collision energy is calculated as the sum of the relative translational energy of the colliding pair $AB-C$ and the vibrational energy of the molecule AB

$$\epsilon_{coll} = \epsilon_{t,AB-C} + \epsilon_{v,AB} \tag{2.89}$$

A dissociation reaction can possibly occur if the collision energy of the pair is greater than the dissociation energy of the molecule AB

$$\epsilon_{coll} > \epsilon_{\text{dissociation},AB} \tag{2.90}$$

In this eventuality, the dissociation reaction in question is affected a probability equal to one and this probability is added to the probability list. Should the dissociation reaction take place, the dissociation energy $\epsilon_{\text{dissociation},AB}$ is removed from the energy balance, A and B are introduced while AB is deleted, and the dissociation counter for this reaction is advanced by one. The remaining energy is finally redistributed between A, B and C. There are a total of 50 dissociation reactions listed in the DSMC chemistry dictionary.

Ionization reactions

Ionization reactions in the form $P + Q \longrightarrow P^+ + e^- + Q$ involve two particles P and Q where P can either be an atom or a molecule and Q can represent any type of particles.

In the case where Q is an electron, the reaction is called electron impact ionization. The procedure describing ionization reactions in the QK framework is equivalent to that of dissociation reactions. The collision energy of the pair P−Q is defined as

$$\epsilon_{coll} = \epsilon_{t,P-Q} + \epsilon_{el,P} \qquad (2.91)$$

where $\epsilon_{el,P}$ is the electronic energy for the particle P and the condition for an ionization reaction to possibly occur is

$$\epsilon_{coll} > \epsilon_{\text{ionization},P} \qquad (2.92)$$

Again, if this condition is met, a probability equal to unity is added to the list of possible reactions to take place. And if the reaction does occur, the ionization energy $\epsilon_{\text{ionization},P}$ is subtracted from the energy balance, particles get created or deleted accordingly to their role played in the reaction, and the ionization counter for this reaction is augmented by one.

Associative ionization reactions

The reaction mechanism for associative ionization reactions depends on the reaction direction. Forward associative ionization reactions written as A + B $\longrightarrow$ AB $\longrightarrow$ AB$^+$+e$^-$ involve two atoms A and B, an intermediate molecule AB, an ionized molecule AB$^+$ and an electron e$^-$. The methodology given by Bird [114] is composed of three main steps that should all be satisfied in sequence for the associative ionization to eventually take place: a) test the recombination of the pair of atoms, b) verify that pseudo-molecule AB is in its ground vibrational state after a Larsen-Borgnakke redistribution, and if successful, redistribute the sum of the collision energy and recombination energy amongst the internal energy modes, and finally c) AB is considered for ionization following the procedure described in the previous paragraph [49].

Reverse associative ionization reactions can be written as AB$^+$ + e$^-$ $\longrightarrow$ AB $\longrightarrow$ A + B. The first two steps remain unchanged except that it is the sum of the collision energy and ionization energy that is redistributed in b). In the last stage, AB is tested for dissociation [49].

Exchange reactions

Exchange reactions take the form AB+C $\longrightarrow$ AC+B where AB is a molecule composed of two atoms A and B, and C a reactant partner that is necessarily an atom. The probability for an exchange reaction to take place is defined as

$$P_{\text{exchange}} = \frac{\left(\epsilon_{coll} - \epsilon_a\right)^{\frac{3}{2} - \omega}}{\displaystyle\sum_{i=0}^{i_{\max}} \left(\epsilon_{coll} - \epsilon_{v,i,P}\right)^{\frac{3}{2} - \omega}} \tag{2.93}$$

where E_a is the activation energy of the reaction, i represents a vibrational energy level and $i_{\max}$ is the maximum vibrational quantum level available to a molecule [47]. The temperature exponent of viscosity of the reacting pair, ω, is usually taken as $\frac{1}{2}\left(\omega_{\text{P}} + \omega_{\text{Q}}\right)$. This probability is added to the probability list.

Charge exchange reactions

Charge exchange reactions can be written as P + Q$^+$ $\longrightarrow$ P$^+$ + Q where P and Q represent either an atom or a molecule. A Larsen-Borgnakke electronic energy redistribution is first considered for the neutral particle P and the charge exchange reaction will take place with a probability equal to

$$P_{\text{charge exchange}} = \frac{g_a \left(\epsilon_{coll} - \epsilon_{el,a,P}\right)^{\frac{3}{2} - \omega}}{\displaystyle\sum_{i=0}^{i_{\max}} g_i \left(\epsilon_{coll} - \epsilon_{el,i,P}\right)^{\frac{3}{2} - \omega}} \tag{2.94}$$

if the new electronic energy level of P is the level directly below the activation energy of the reaction. In Eq. 2.94, $\epsilon_{el,i,P}$ and g_i stand for the electronic energy and the degeneracy of the electronic energy level i for particle P and the exponent a is the electronic quantum level immediately below the activation energy of the reaction.

Chapter 3

Verification and Validation of the *hy2Foam* Code

The newly coded two-temperature solver will now be verified considering the contributions of competing mechanisms in isolation and a zero-dimensional adiabatic heat bath will first be used for this purpose in Section 3.1. Vibrational-Translational (V–T) and Vibrational-Vibrational (V–V) energy transfers will be reviewed and both Park TTv and the coupled vibration-dissociation-vibration (CVDV) model for chemistry-vibration coupling will be tested. This first section ends with a CFD-DSMC comparison for the thermo-chemical relaxation of a non-ionized air mixture. Section 3.2 is then dealing with multi-dimensional case scenarios of increasing complexity considering 1-D Fourier flows in sub-section 3.2.1, a 2-D axisymmetric blunt body for a Mach 11.3 non-reacting nitrogen flow in 3.2.2 and a 2-D circular cylinder for both non-reacting and reacting Mach 20 nitrogen flows in 3.2.3.

3.1 Zero-dimensional analysis

From an initially disturbed system, the V–T relaxation of a single-species gas to recover equilibrium conditions will first be investigated. This will be followed by the V–T and V–V thermal relaxations of several mixtures. The relaxation towards equilibrium of a chemically-reacting mixture will finally be carried out. The verification is supported by comparisons against results from DSMC codes *dsmcFoam* and MONACO [116], and the

CFD two-temperature solver LeMANS. Throughout this entire section, the heat bath is composed of a single cubic cell of length 1×10^{-5} m. The time-step for CFD and DSMC computations has been set at 1×10^{-9} s. At least 50,000 DSMC particles were used for each *dsmcFoam* run [117] and data shown are the ensemble average resulting from three statistically-independent computations. It should be noted that the *dsmcFoam* code used here has three temperatures: translational, rotational, and vibrational. However, the rotational collision number, Z_r, can be tuned and set to unity to allow a direct comparison between *dsmcFoam* and two-temperature CFD solvers in the absence of electronic energy.

3.1.1 Vibrational-Translational relaxation of a single-species gas

Case without electronic energy

Following the work of Boyd and Josyula [118], vibrational heating $(T_v^0 < T_{tr}^0)$ and vibrational cooling $(T_v^0 > T_{tr}^0)$ heat bath simulations involving nitrogen have been performed. Results from *hy2Foam* and *dsmcFoam*, and published data using LeMANS and MONACO are shown in Figures 3.1(a) and 3.1(b).

In the heating case, the initial trans-rotational temperature is set at $10,000$ K while the vibrational temperature is lowered down to $1,000$ K. The initial pressure is set to 1 atm. From Eq. 2.40 and 2.54, the number of vibrational of degrees freedom associated with the simple harmonic model for nitrogen at T_v^0 is equal to $\zeta_{tot}^0 = 0.240$. This corresponds to an initial overall temperature of $9,588$ K according to Eq. 2.53. In Figure 3.1(a) the *hy2Foam* solver is run twice, first in a default configuration with the A_{N_2,N_2} coefficient taken from Park's 1993 table, and secondly in a configuration that represents a best-fit to *dsmcFoam* results by adjusting the value of A_{N_2,N_2}, as shown with the red solid lines.

An excellent agreement is observed between the default configuration of *hy2Foam*, the CFD code LeMANS and the DSMC code MONACO. *dsmcFoam* predicts a noticeably longer thermal relaxation that is 48% slower (defined as the time to recover 99% of the equilibrium temperature).

It can be seen that all simulations converge towards an equilibrium temperature of $T^{eq} = 7,623.3$ K. The number of vibrational of degrees freedom for nitrogen at T^{eq} is
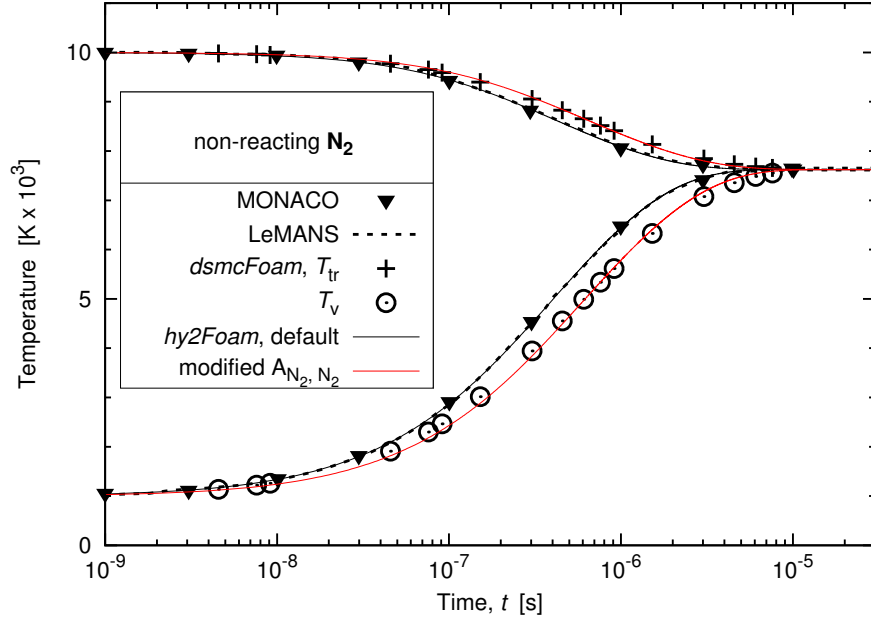
(a) Vibrational heating: $T_{tr}^0 = 10,000$ K, $T_{v,N_2}^0 = 1,000$ K, and $p^0 = 1$ atm
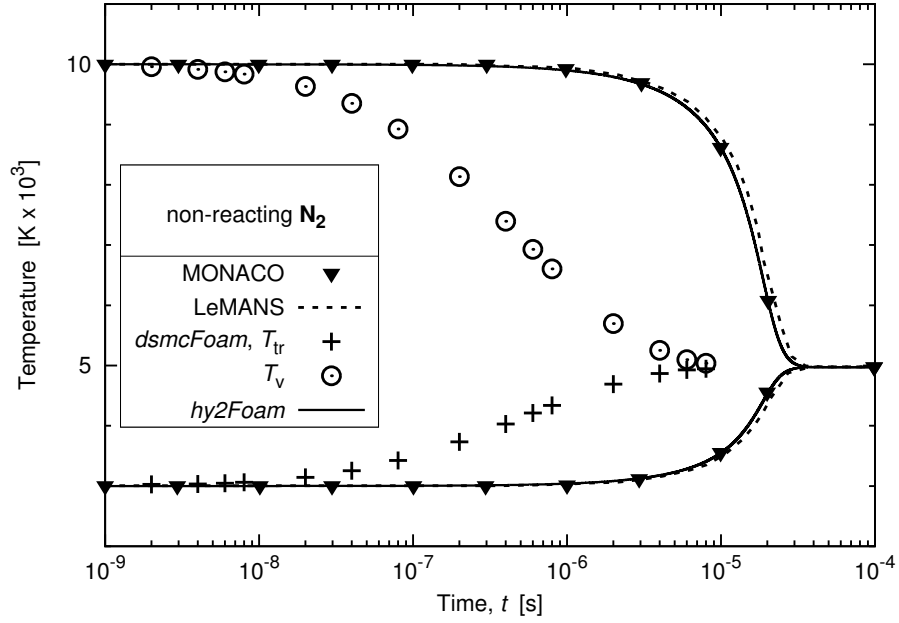
(b) Vibrational cooling: $T_{tr}^0 = 3,000$ K, $T_{v,N_2}^0 = 10,000$ K, and $p^0 = 1$ atm

Figure 3.1: V–T relaxation towards equilibrium of a N_2 heat bath

1.590. Hence, the total number of degrees of freedom at equilibrium is $\zeta_t^{eq} + \zeta_r^{eq} + \zeta_v^{eq} = \zeta_{tot}^{eq} = 6.590$. A straightforward calculation that ensures energy equipartition enables the determination of the initial overall temperature

$$T_{ov}^0 = T^{eq} \times \frac{\zeta_{tot}^{eq}}{\zeta_{tot}^0} \qquad\qquad (3.1)$$

The calculation produces an initial overall temperature of $9,588.0$ K which is therefore consistent with the aforementioned value and in agreement with both DSMC codes.

In the cooling case, the initial trans-rotational temperature is set to $3,000$ K while the vibrational temperature is increased to $10,000$ K. The *hy2Foam* results match exactly with the prediction given by MONACO in Figure 3.1(b). Conversely, there are significant differences between *dsmcFoam* and *hy2Foam*. The post-collisional energy redistribution in *dsmcFoam* is handled by the quantum Larsen-Borgnakke procedure [44]. MONACO adopts the standard Larsen-Borgnakke procedure but post-collisional energy redistribution is ensured to be consistent with the CFD approach at a macroscopic scale [118, 119], which explains why the results are comparable to *hy2Foam* and LeMANS.

Case with electronic energy

In the preceding heating case, the electronic energy has no significant effect on thermal relaxation if the initial trans-rotational temperature is maintained at 10,000 K and it has thus been increased up to $T_{tr}^0 = 30,000$ K. The effect of the electronic energy mode on the thermal relaxation of the nitrogen molecules is displayed in Fig. 3.2. The equilibrium temperatures reached in both cases agree with energy equipartition and are specified on the right-hand side.

Without electronic energy, the *hy2Foam* and *dsmcFoam* results are in very satisfactory agreement considering the degree of empiricism that the two-temperature solution carries. With the inclusion of the electronic energy the relaxation to equilibrium is observed to be around $26\,\%$ faster. These runs highlight the importance of the electronic energy mode that is often overlooked in re-entry case studies [47]. Indeed, the difference in equilibrium temperature is not of the order of a few percent but is in the present case as large as $23.7\,\%$. Accounting for the electronic mode of nitrogen thus becomes necessary above $10,000$ K to accurately predict thermal quantities for example.

The results shown in Figures 3.1(a), 3.1(b), and 3.2 therefore validate the imple-
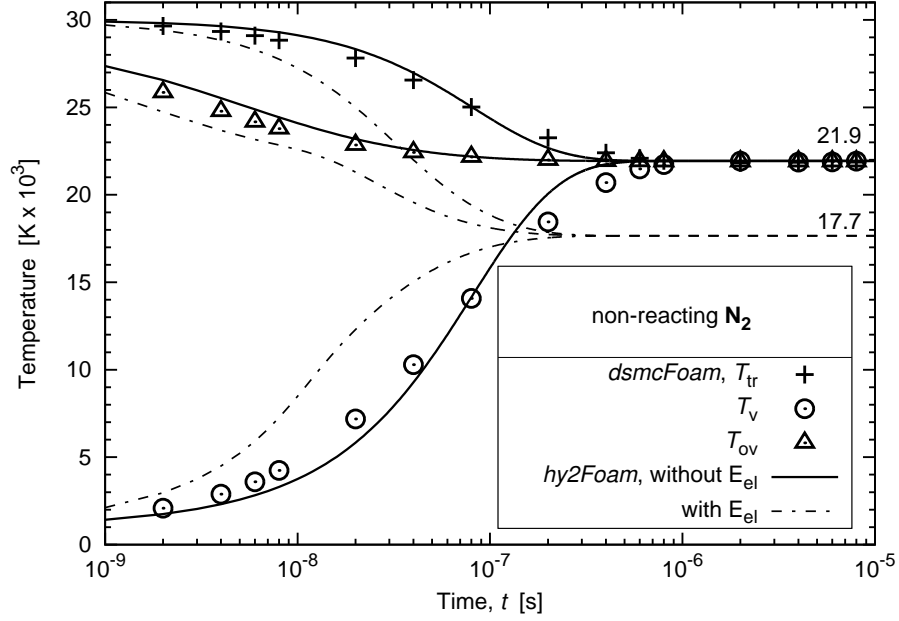
Figure 3.2: Thermal relaxation of a N_2 heat bath with and without electronic energy

mentation of *hy2Foam* for a single-species gas.

3.1.2   Vibrational-Translational relaxation of a non-reacting multi-species gas

The non-reacting heat bath is now composed of gas mixture made of N_2 and N in equal proportions. The initial temperatures remain unchanged with regard to the previous paragraph and number densities are equal to 5.0×10^{22} m^{-3} for both species. In Figure 3.3, the equilibrium temperature specified on the right-hand side is once more consistent with energy equipartition and the same value is recovered using *dsmcFoam* and LeMANS. The disaccord between the *hy2Foam* and *dsmcFoam* solutions appear to be slightly greater that in the case considered without atomic nitrogen, nonetheless, they do remain satisfactory. The results using LeMANS are not in agreement with *hy2Foam*; however, a different convention is adopted for Eq. 2.62 in LeMANS where the number density $n_{m,s}$ represents the mixture number density and σ_m equals 1×10^{-20} m^2. For clarity, these modifications have been temporarily implemented in *hy2Foam* and are shown by the red solid line in Figure 3.3. The temperature profiles are now shown to be nearly superimposed, thus verifying the *hy2Foam* implementation for a

mixture.

Compared to the full N_2 configuration shown in Figure 3.2, the increase in equilibrium temperature due to the loss of half of the mixture vibrational energy is less pronounced with the inclusion of the electronic mode. This can be explained by the relative importance of the electronic mode of N that brings 1.39 degrees of freedom to the mixture at T^{eq}, and thus compensates part of the vibrational energy loss.
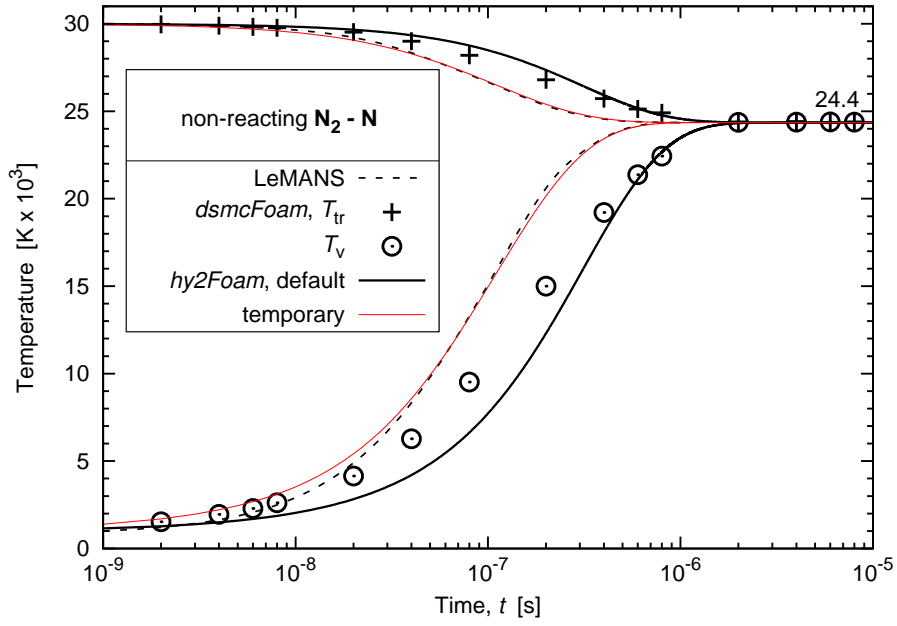
Figure 3.3: V–T relaxation of a N_2-N heat bath

3.1.3 Vibrational-Translational and Vibrational-Vibrational relaxations

A vibrational cooling scenario with a high initial vibrational temperature is chosen to better illustrate the role of vibrational-vibrational energy exchange. The mixture is composed of oxygen and nitrogen molecules in equal proportions. The initial trans-rotational temperature is set at 5,000 K, the vibrational temperature at 30,000 K, and the pressure at 1 atm. In Figure 3.4, the thermal relaxation process in *hy2Foam* is presented with and without V–V energy transfer using dashed-dotted and solid lines, respectively.

As it is supposed to, V–V energy transfer promotes vibrational energy redistribution between the vibrational energy pools and thus a quicker relaxation towards equilibrium
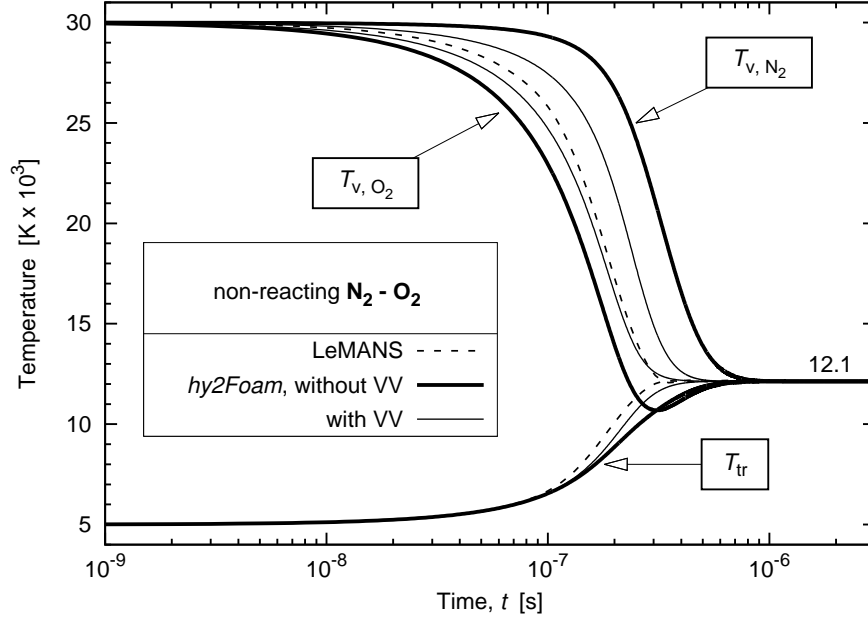
Figure 3.4: V–T and V–V relaxations of a $N_2 - O_2$ heat bath

is achieved. In the present case, the N_2 and O_2 vibrational energy pools remain distinct throughout the calculation. The solver LeMANS has only one vibrational temperature. Logically, this unique vibrational temperature profile should be somewhere between the $T_{v,N_2}(t)$ and $T_{v,O_2}(t)$ profiles when the V–V transfer is enabled and this is precisely what is observed in Figure 3.4.

Figures 3.3 and 3.4 provide sufficient evidence of the verification of *hy2Foam* for a non-reacting multi-species gas.

3.1.4   Relaxation of a chemically-reacting mixture

The chemical reaction considered is the irreversible molecule-molecule dissociation of nitrogen

$$N_2 + N_2 \xrightarrow{k_f} 2N + N_2$$
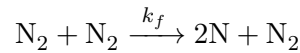
The rate coefficients are shown in Table 3.1 in which the units of A and T_a are given in $cm^3 \, mol^{-1} \, s^{-1}$ and Kelvin, respectively. They come from the Quantum Kinetic (QK) theory [44], and Park's rates for the use of a two-temperature CFD model [7].

The next simulations are run from an initial trans-rotational temperature of 30,000

Table 3.1: Chemically-reacting heat bath: parameters for the evaluation of k_f

Reaction rate	Arrhenius law constants		
	A	β	T_a
Park (1993)	7.0×10^{21}	-1.6	$113,200$
QK (2015)	2.47×10^{18}	-0.62	$113,500$

K and vibrational temperature of 1,000 K. The initial number density is equal to 5.0×10^{22} m^{-3} for both species. In the following, the *hy2Foam* configuration named *Park* shown with solid lines in Figure 3.5 makes the use of the Park TTv model and Park's 1993 chemical rate constants, which is the most commonly adopted set-up in the hypersonic community. The second configuration shown with dashed-dotted lines and called *CVDV–QK* results in the combination of the CVDV chemistry-vibration model and the QK rates.

It can first be noted that in using the conventionally-adopted *Park* set-up, the decrease in trans-rotational temperature is not well-captured. The chemical reactions take about ten times longer to have a significant effect on the mixture composition when compared to the DSMC solution. Using the *CVDV–QK* configuration in *hy2Foam*, a much improved agreement is achieved with regard to the DSMC simulations. The trans-rotational temperature and species concentrations are now correctly estimated over time, while the early increase in vibrational temperature can be imputed to a departure from a Boltzmann distribution and certain aspects of current multi-temperature CFD modelling approaches used to describe N_2-N_2 and N_2-N interactions [120].

Both CFD and DSMC chemistry modules must deliver consistent results in the development of any hybrid CFD-DSMC code. The appropriateness of the *CVDV–QK* configuration is thus further evaluated for a mixture initially set in a state of thermal equilibrium. Figure 3.6 confirms the trend observed in Figure 3.5. The *Park* configuration first initiates a thermal relaxation before any chemistry takes place which results in a lag in the vibrational temperature decrease. Conversely, the profiles predicted by *dsmcFoam* are once again much better approximated by the *CVDV–QK* configuration.

It can be concluded that the *CVDV–QK* set-up is a more suitable choice for use in a CFD solver than the *Park* configuration when compared to a DSMC code that uses
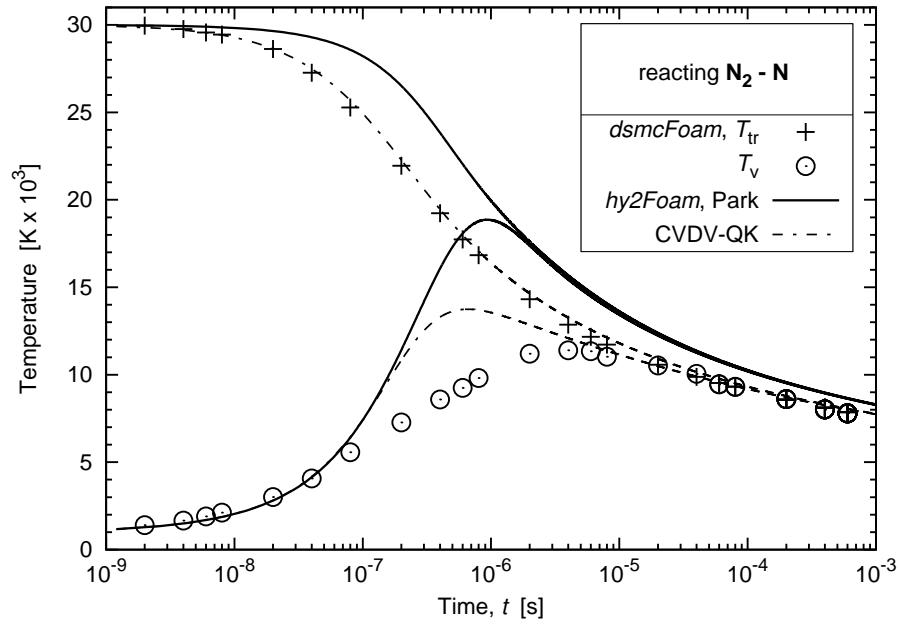
(a) Temperature versus time
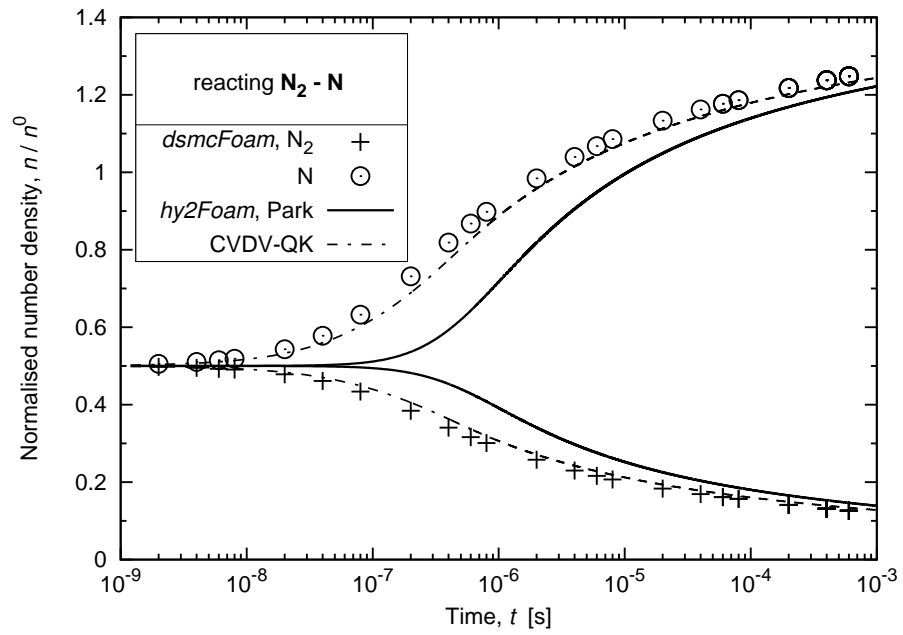
(b) Normalised number density versus time

Figure 3.5: Influence of the chemistry-vibration model and chemical rate constants on a chemically-reacting N_2-N heat bath

Quantum-Kinetic chemistry.
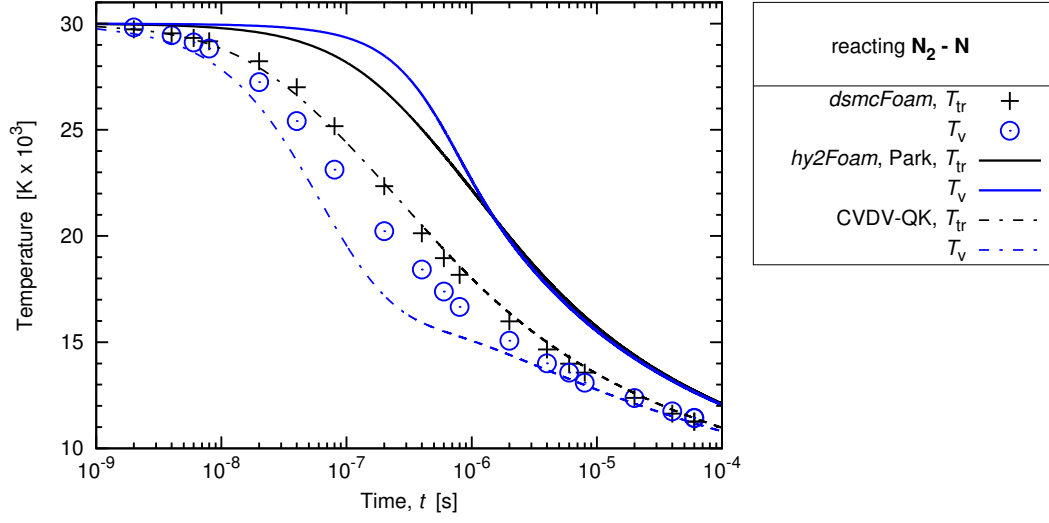
(a) Temperature versus time
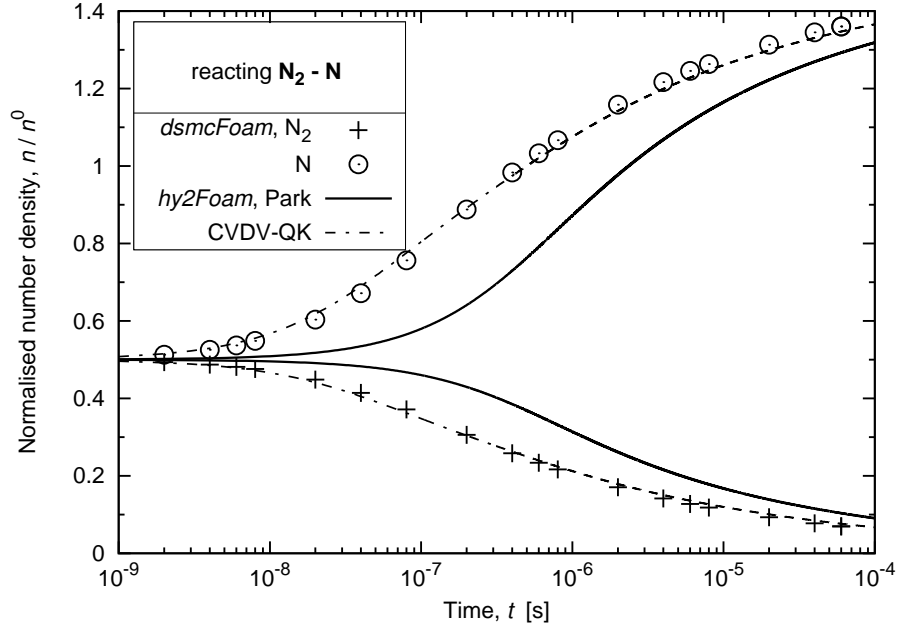
(b) Normalised number density versus time

Figure 3.6: Chemically-reacting N_2-N heat bath in an initial state of thermal equilibrium

3.1.5   Chemically-reacting air

To conclude on the validation of the *hy2Foam* solver using adiabatic heat baths, the complete set of 19 reactions to occur in a pre-heated 5-species air is considered. The 15 dissociation reactions and four exchange reactions are listed in Table 1 in Ref. [44]. The initial pressure is set at 0.063 atm and the initial temperature is equal to 10, 000 K.

It is supposed in this case that all molecular temperatures are in thermal equilibrium at all times. In *hy2Foam*, the possibility is offered to the user to downgrade the two-temperature solver to a single-temperature solver. This latter solver is given the name *hyFoam* for clarity.

By doing so, there is again a very good agreement between *hy2Foam* and LeMANS temperature and number density fields as shown in Figure 3.7.
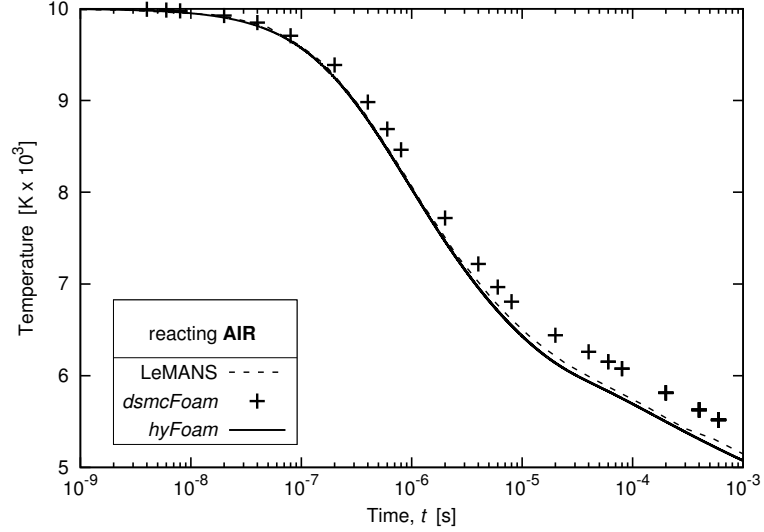
(a) Temperature versus time
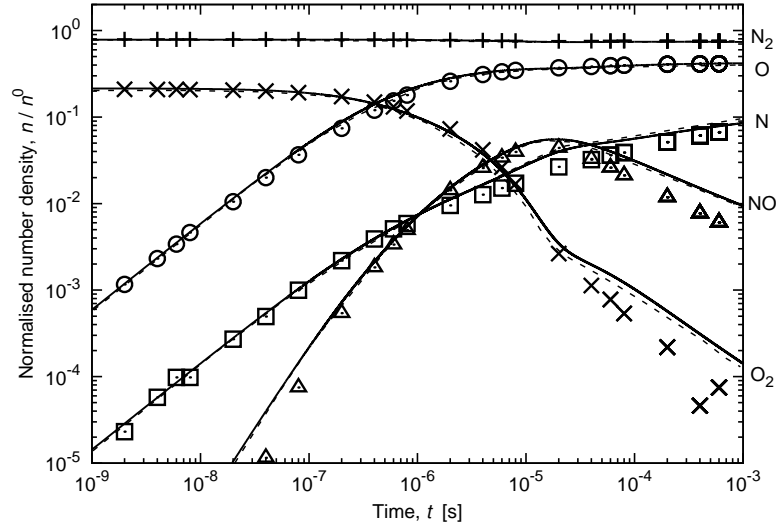
(b) Normalised number densities versus time

Figure 3.7: Thermo-chemical relaxation of a 0.79 N_2 - 0.21 O_2 heat bath, where the *dsmcFoam* symbols are represented as: N_2 (+), O_2 (×), NO (△), N (⊡), and O (⊙).

3.2   Multi-dimensional analysis

3.2.1   Fourier flows

A heat transfer flow, also called Fourier flow, is simulated with *hy2Foam* and *dsmcFoam*. It is a one-dimensional periodic flow where two infinite parallel walls are separated by $H = 1$ m along the y-direction. The mesh is constructed with OpenFOAM's utility *blockMesh*. The flow velocity is set constant to 300 m s^{-1} and a slip velocity of the same magnitude is imposed on both walls. The top wall is heated at a temperature of 3,000 K, while the bottom wall temperature is set to equate $T_b^0 = 2{,}000$ K. Diffuse wall boundaries are used in *dsmcFoam* and the first-order Smoluchowski temperature jump [97] and Maxwell velocity slip [95] with the accommodation coefficients being taken as equal to unity are employed in *hy2Foam*. These conditions are reported in Table 3.2.

Table 3.2: Fourier flows: initial conditions for all cases considered

Quantity	Value	Unit
Velocity	300	m s^{-1}
Bottom wall temperature, T_b^0	2000	K
Top wall temperature	3000	K

Three main cases are investigated with different initial mixture compositions: 1) pure nitrogen, 2) homogeneous air, and 3) non-homogeneous air. The air composition is modified to be 0.5 N_2 - 0.5 O_2 in molar proportions. Case 2 is decomposed into two sub-cases a and b as outlined in Table 3.3. The initial mixture number density is varied so as to have an overall Knudsen number lying in the bottom range of the continuum-transition regime (case 2a) and in the transition regime (case 2b). The interest of case 3 is to test the implementation of species diffusion and to determine which of the models presented in Section 2.1.4 performs best with regards to the *dsmcFoam* solution. Above the channel centerline, the domain is initially filled with pure nitrogen and below that line the gas is pure oxygen. This case scenario examines the *hy2Foam* implementation assuming that both N_2 and O_2 are vibrationless molecules and that translational and rotational energy modes are in equilibrium with each other. In addition, the overall Knudsen number is the same than in case 2a, namely 0.002.

Species thermal properties in the CFD computations are determined using a power

Table 3.3: Initial conditions for each specific Fourier flow

Quantity	Unit	Case			
		1	**2a**	**2b**	**3**
N$_2$ number density, $n^0_{N_2=n^0}$	m$^{-3} \times 10^{-19}$	2.086	52.15	1.043	104.3
O$_2$ number density, $n^0_{O_2}$	m$^{-3} \times 10^{-19}$	0	52.15	1.043	104.3
Overall Knudsen number, Kn_{ov}	-	0.1	0.002	0.1	0.002

law and for cases involving a mixture, the mixing rule is that of Armaly and Sutton. Good DSMC practice is adopted and recalled hereafter for case 1. Adopting the variable hard sphere model for the mean-free-path, λ, and this latter quantity will equate to 0.1 m. It is recommended that the cell size be a fraction of λ and it is thus set to 0.05 m. Further calculations for the mean residence time and mean collision time yields values of 3.5×10^{-5} s and 9.1×10^{-5} s, respectively. The time-step should be a fraction of these two quantities and 1×10^{-5} s is therefore retained. Cell size and time-step for cases 2 and 3 are modified according to these rules when necessary. In cases 1 and 2, macroscopic variables are sampled over time once convergence is achieved, while in case 3 it is the transient behaviour of the solution that is studied and it is thus required to perform an ensemble average over 5 statistically-independent DSMC runs to recover the macroscopic fields.

Results for the homogeneous Fourier flows 1, 2a and 2b are presented in Figure 3.8. CFD and DSMC trans-rotational and vibrational temperature profiles are compared along the y-direction and are overall showing a good agreement for the two flow regimes studied and whether the gas is composed of one or two species. In case 2a, the relative error for trans-rotational and vibrational temperatures is approaching zero. Increasing the number of DSMC simulators or the number of statistically-independent DSMC simulations would help to decrease the scatter but this would be costly at $Kn_{ov} = 0.002$. Increasing the overall Knudsen number in cases 1 and 2b results as expected in the on-set of rarefaction effects in the near-wall region with larger discrepancies in the estimation of the temperature jump value between the two codes. It should be noted that the relative error will, in most cases, be the order of a few percent due to the nature of the case scenario that exhibits small deviations from the continuum solution.

The transient computations of case 3 are reported in Figure 3.10 for the two instants

(a) Normalised T_{tr}, case 1

(b) Normalised T_{v,N_2}, case 1

(c) Normalised T_{tr}, case 2a

(d) Normalised $T_{v,m}$, case 2a

(e) Normalised T_{tr}, case 2b

(f) Normalised $T_{v,m}$, case 2b
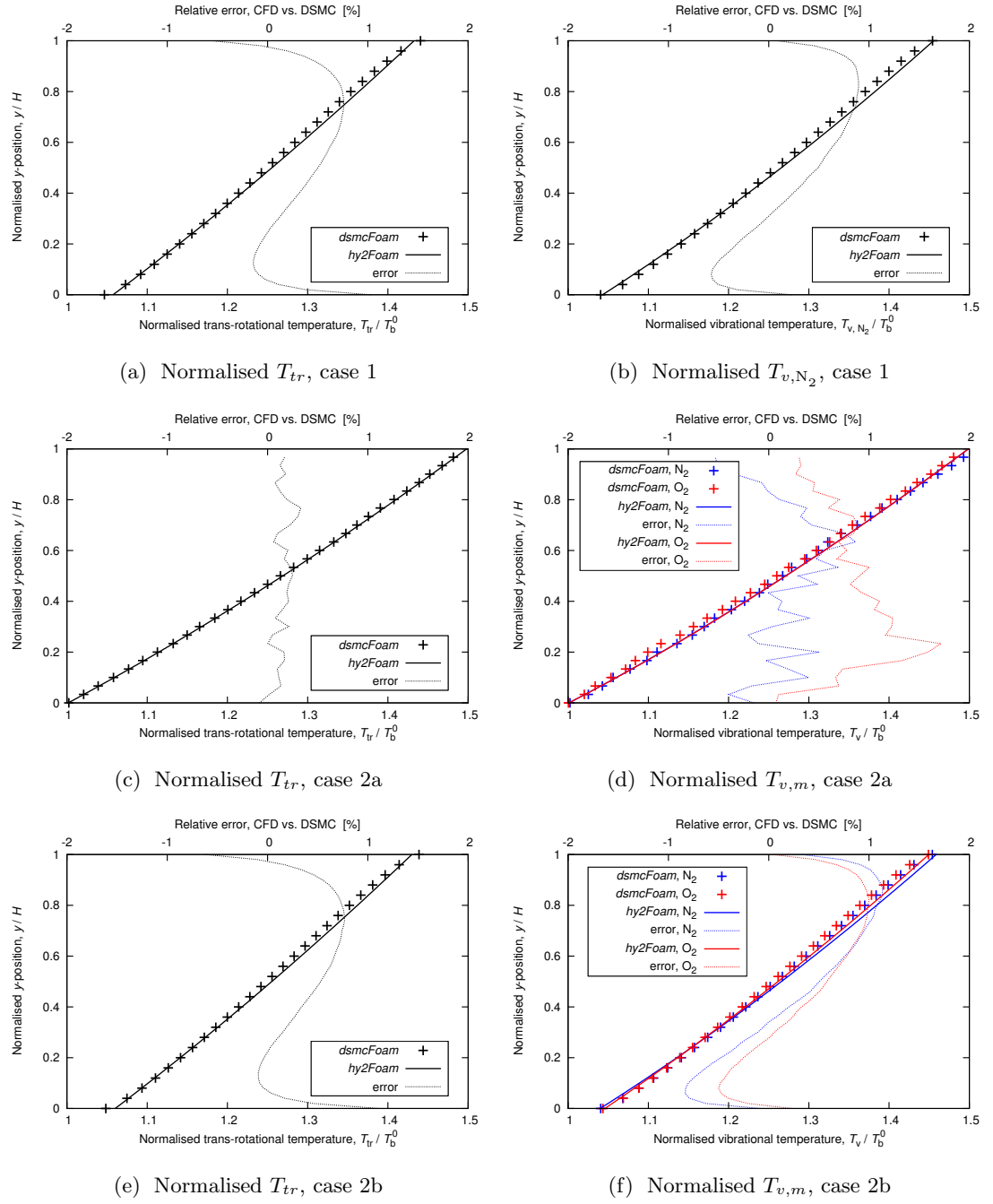
Figure 3.8: Homogeneous Fourier flows: normalised temperature profiles and relative errors

$t = 0.02$ s and $t = 0.1$ s. Various models are chosen to calculate the diffusion coefficients and are exposed in the subsequent graphs: Lewis number 1.0 (denoted by L 1.0) and the generalised Fick's law using either Gupta's 1989 curve fit for binary diffusion coefficients ($\text{FG}_{\bar{D}89}$, see Eq. 2.27), Gupta's 1990 curve fit for collision cross-sections ($\text{FG}_{\bar{\Omega}90}$, see

Eq. 2.32) or Stephani's expression (FS, see Eq. 2.33 and 2.34). These latter three models are plotted in Figure 3.9 for two mixtures having individual species number densities matching those of case 3. It is shown for a N_2-O_2 mixture that FS and $FG_{\bar{D}89}$ expressions are in excellent concordance while $FG_{\bar{\Omega}90}$ tends to over-estimate the N_2-O_2 diffusion coefficient as compared with Stephani's. Results for a N_2-N gas is also presented in Figure 3.9(b) to highlight that an agreement between the models depends on the pair considered. For a N_2-N mixture, all three models agrees well with each other for temperatures up to 15,000 K.

(a) $D_{N_2-O_2}$ vs. temperature   (b) D_{N_2-N} vs. temperature
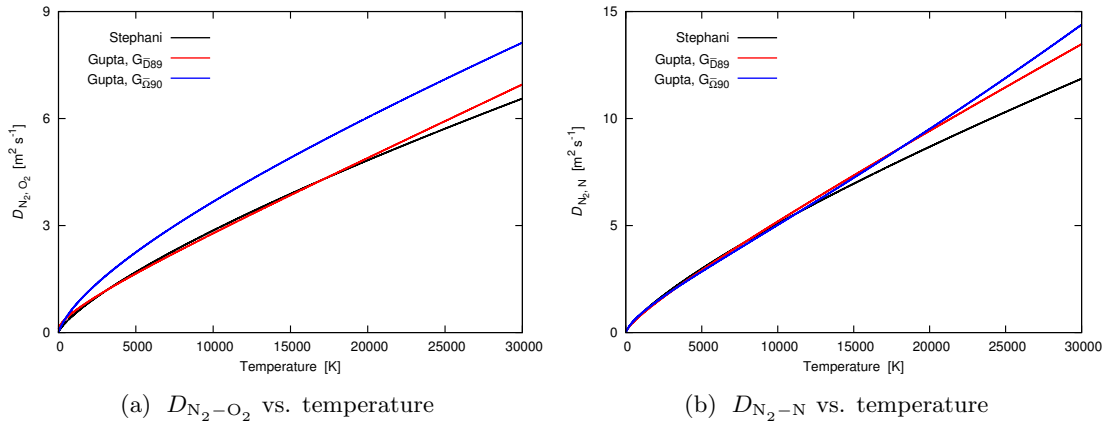
Figure 3.9: Diffusion coefficients values versus temperature as predicted by different models for species number densities matching those of case 3

The *dsmcFoam* solution is well approximated by the generalised Fick's law that uses either FS and $FG_{\bar{D}89}$ expression for diffusion coefficients. $FG_{\bar{\Omega}90}$ formulation and coefficients is seen to promote an excessive mixing as compared with DSMC, even if this has little consequence on the temperature distribution across the channel. Those results correlates well with the observations made in Figure 3.9(a).

Additional information about Fourier flows, and Couette flows, making the use of *dsmcFoam* and *hy2Foam* can be found in [66].

(a) Normalised T_{tr}, t = 0.02 s

(b) Normalised n_m, t = 0.02 s

(c) Normalised T_{tr}, t = 0.1 s

(d) Normalised n_m, t = 0.1 s
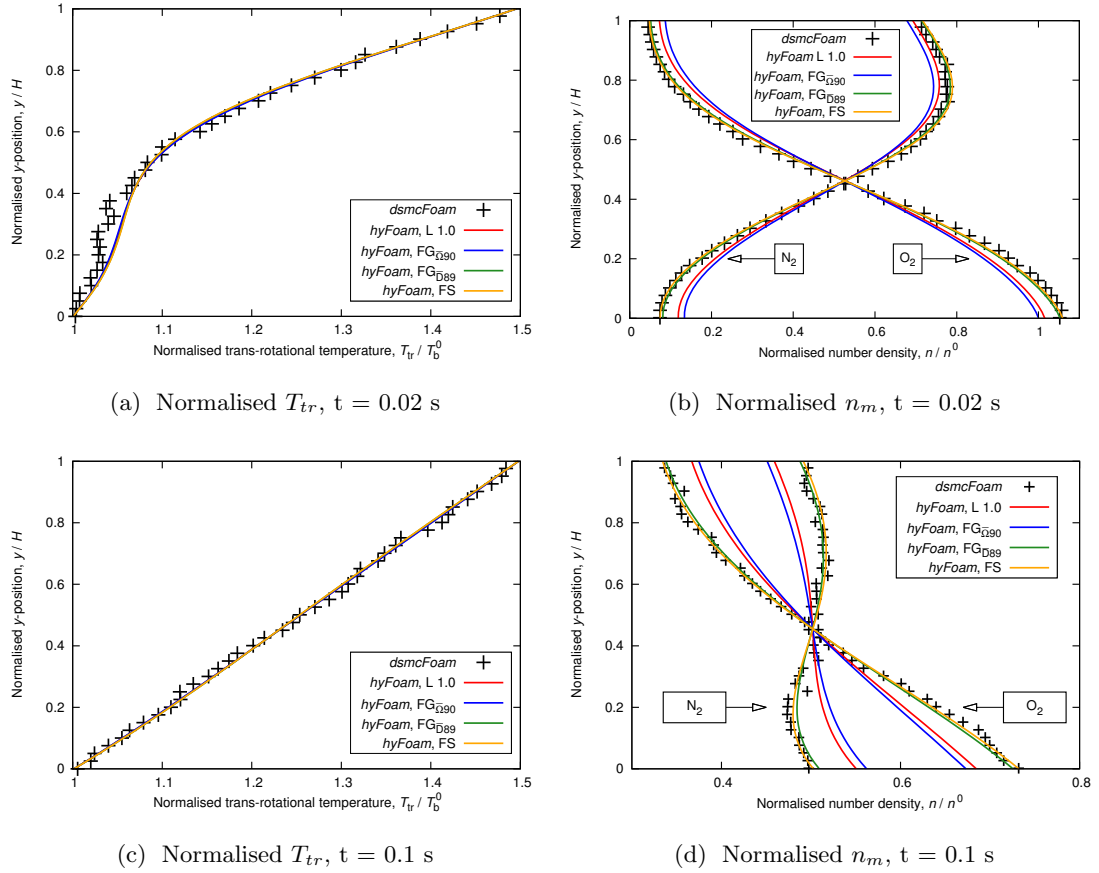
Figure 3.10: Non-homogeneous Fourier flow, case 3: normalised temperature and number density profiles. L stands for Lewis number, F for Fick's law, $G_{\bar{\Omega}90}$ for Gupta 1990's curve fit, $G_{\bar{D}89}$ for Gupta 1989's curve fit and finally S for Stephani.

3.2.2 Mach 11.3 blunted cone

In this sub-section, a non-reacting nitrogen flow past a blunted cone is examined at Mach 11.3. The case is composed of a 6.35 mm-radius nose followed by a flat plate forming a $25°$ angle with the free-stream flow direction and whose streamwise extension is 5 cm. The 2-D axisymmetric mesh that has been employed is shown in Fig. 3.11. The structured grid is aligned with the bow shock and consists of 600 by 200 cells. The first spacing at the wall surface is set to $2\,\mu$m by default and to $10\,\mu$m for comparison purposes.

The initial conditions of this case scenario are given in Table 3.4. The free-stream velocity corresponding to a Mach number of 11.3 is 2,764.5 m s^{-1}. The free-stream temperature and pressure are 144.4 K and 21.9 Pa, respectively. The wall is assumed to be isothermally heated to a temperature of 297.2 K. This simulation uses the MWP
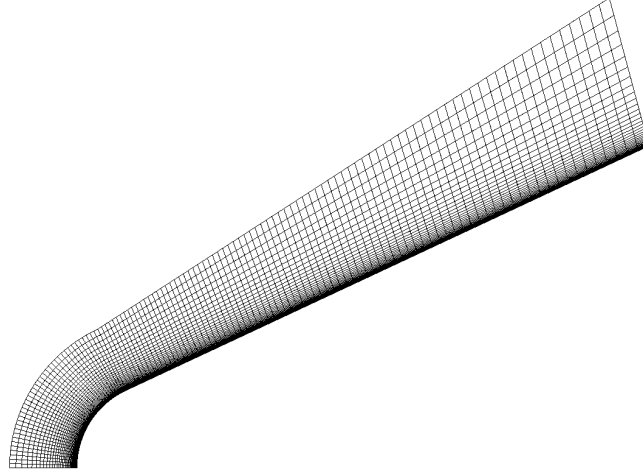
Figure 3.11: Mesh for the blunted cone (each 5th line is represented in each direction).

formulation for V–T energy exchange and the Blottner and Eucken formulas to compute transport properties. The variable hard sphere model is chosen for the calculation of the mean-free-path and the Knudsen number is computed using the streamwise extent of the cone as the characteristic length. The non-equilibrium boundary conditions employed at the cone surface are the first-order Smoluchowski temperature jump and Maxwell velocity slip with the accommodation coefficients being taken as equal to unity.

Convergence was achieved after 2.8 hours of computations on the ARCHIE-WeSt High Performance Computer [121]. The run used 24 Intel Xeon X5650 2.66 GHz cores with 48 GB RAM and Infiniband Interconnect computer-networking communications.

Table 3.4: Initial conditions for the Mach 11.3 blunted cone

Quantity	Value	Unit
Free-stream velocity, U_∞	2,764.5	m s^{-1}
Free-stream pressure, p_∞	21.9139	Pa
Free-stream density, ρ_∞	5.113×10^{-4}	kg m^{-3}
Free-stream temperature, T_∞	144.4	K
Free-stream mean-free-path, λ_∞	1.01×10^{-4}	m
Overall Knudsen number, Kn_{ov}	0.002	-
Wall temperature, T_w	297.2	K

This particular configuration has already been studied by Wang and Boyd [24], using the MONACO DSMC code and a Navier-Stokes CFD solver from the University of Michigan. The results from these simulations are reported in the subsequent graphs
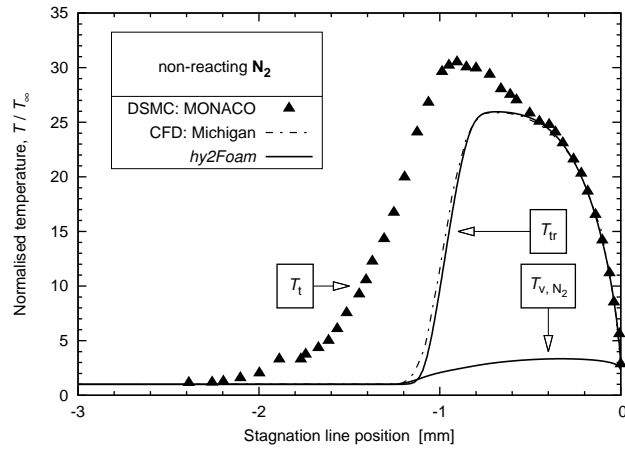
(a) Normalised temperature
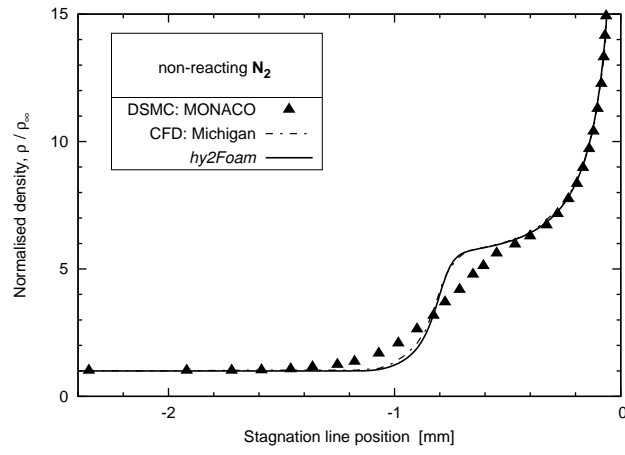
(b) Normalised mass density
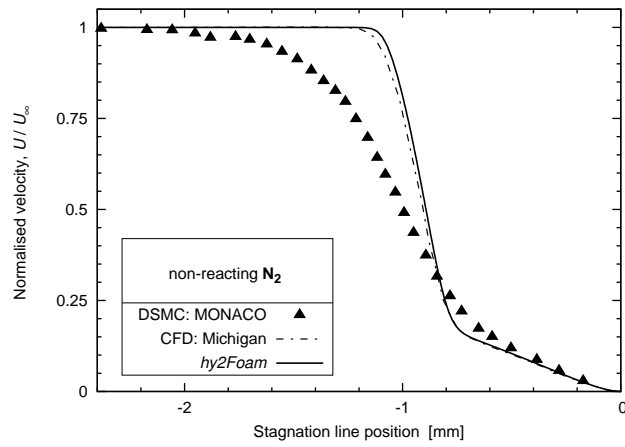
(c) Normalised velocity

Figure 3.12: Stagnation line profiles for the blunted cone case
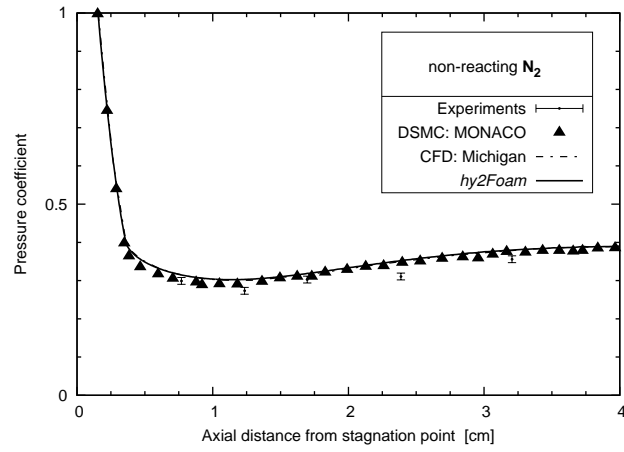
(a) Pressure coefficient
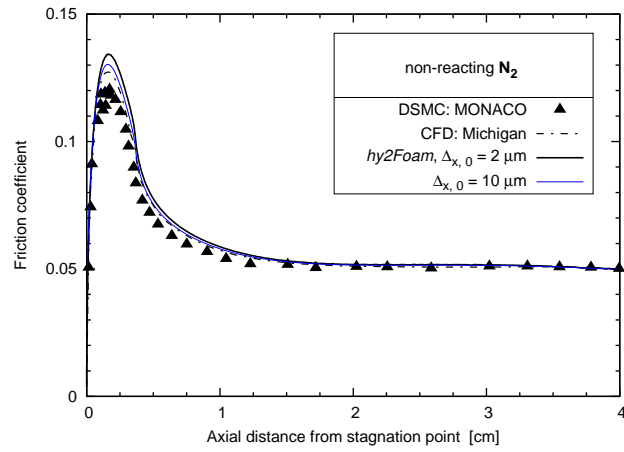
(b) Friction coefficient
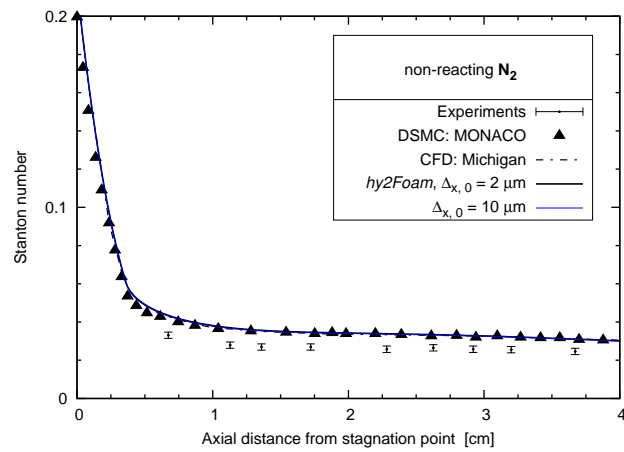
(c) Stanton number

Figure 3.13: Surface quantities along the blunted cone surface

with the denomination *DSMC: MONACO* and *CFD: Michigan*. Moreover, experimental data is also shown in Figures 3.13(a) and 3.13(c) and correspond to the run 31 of the CUBRC experiments [122].

The emphasis is placed on stagnation line data and then on surface properties such as the pressure coefficient, $\mathcal{C}_p$, friction coefficient, $\mathcal{C}_f$, and Stanton number, St, respectively given by

$$\mathcal{C}_p = \frac{p - p_\infty}{0.5\,\rho_\infty\,U_\infty^2} \quad (3.2) \qquad \mathcal{C}_f = \frac{\tau}{0.5\,\rho_\infty\,U_\infty^2} \quad (3.3) \qquad St = \frac{q}{0.5\,\rho_\infty\,U_\infty^3} \quad (3.4)$$

those essential aerothermodynamic quantities being shown in Figures 3.13(a)-(c).

In Figures 3.12(a)-(c), the pressure, temperature, and velocity stagnation line solutions given by the CFD code of Wang and Boyd are very similar to the ones produced by *hy2Foam*. It can be seen in Figure 3.12(a) that the vibrational mode is barely excited for this case scenario. The single-temperature model version of *hy2Foam* gave the same results. The small discrepancies concerning the shock stand-off distance can easily be explained by the difference in grid point density along the symmetry axis (indeed, the spatial extension of the domain normal to the body adopted here is about 40 % larger then the one in [24]) and by the use of a different viscosity model (the power law was used in [24]). As it is the case in most simulations of hypersonic flow-fields, the bow shock thickness given by the NSF equations is clearly under-predicted, as shown by the different DSMC profiles.

Once again in Figures 3.13(a)-3.13(c), an excellent agreement is found between *hy2Foam* and the Michigan NSF solver as the profiles of the surface quantities are shown to be superimposed with a first spacing of $10\,\mu$m. If the mesh is further refined to $2\,\mu$m, a small decrease in the Stanton number is observed. In conclusion, it is thought that the mesh used in [24] had a first spacing close to $10\,\mu$m.

The variable hard sphere mean-free-path computed by *hy2Foam* in the wall vicinity is of the order of $2\,\mu$m. Good DSMC practice dictates that the mean-free-path to cell-size ratio should exceed one so one could argue that the DSMC mesh employed might not be fine enough near the wall to accurately capture the surface aerothermodynamic

coefficients along the body, *e.g.*, the peak amplitude of the skin-friction.

Finally, this case is a good illustration that a hypersonic simulation can now be carried out using open-source packages all the way from pre- to post-processing using Gmsh [123] as a mesher, *hy2Foam* as a solver, Paraview [124] as a visualization utility, and Gnuplot [125] as a grapher.

3.2.3   Mach 20 Cylinder

The focus is now set on the hypersonic Mach 20 flow of nitrogen over a two-dimensional circular cylinder of radius R = 1 m. A symmetry plane exists about the $y = 0$ plane allowing the modelling solely of the upper half of the domain to be considered. The streamwise extent of the computational domain spans from -1.8 m to 5 m and the initial conditions are listed in Table 3.5.

A free-stream velocity of 6,047 m s^{-1} is applied with a free-stream pressure of 0.89 Pa and temperature $T_\infty = 220$ K. Such a temperature is high enough to result in a vibrationally-excited and chemically active flow-field. The cylinder wall is held at a uniform temperature of 1,000 K. The overall Knudsen number of 0.0022 lies in the lower range of the continuum-transition regime, however, the gas locally may lie in the transition regime.

Table 3.5: Initial conditions for the Mach 20 cylinder

Quantity	Value	Unit
Free-stream velocity, U_∞	6,047	m s^{-1}
Free-stream pressure, p_∞	0.89	Pa
Free-stream density, ρ_∞	1.363×10^{-5}	kg m^{-3}
Free-stream temperature, T_∞	220	K
Free-stream mean-free-path, λ_∞	4.45×10^{-3}	m
Overall Knudsen number, Kn_{ov}	0.0022	-
Wall temperature, T_w	1,000	K

CFD set-up   The mesh used in this investigation is shown in Figure 3.14 and was constructed using Ansys ICEM CFD [126]. This mesh consists of 155,000 cells with the first cell spacing at the cylinder wall set to 2 microns. Both Maxwellian velocity slip and Smoluchowski temperature jump boundary conditions were applied at the walls

with the accommodation coefficient equal to 1.
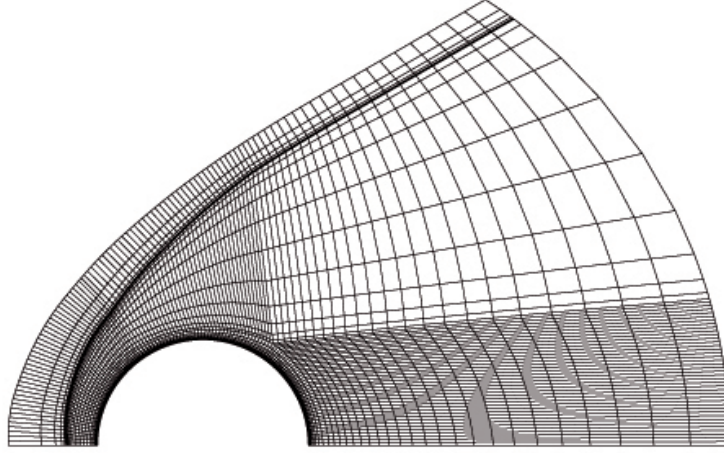
Figure 3.14: Mesh for the cylinder (each 5th line is represented in each direction).

Both MWP and SSH formulations are successively used for V–T energy transfer for comparison purposes. For the shear viscosity and the thermal conductivity, the Blottner and Eucken formulae were applied, respectively, while the mixing rule employed was that of Armaly and Sutton. Species diffusion was modelled using Fick's law and Gupta's 1990 curve fit (denoted as $FG_{\bar{\Omega}90}$) as it has previously shown to be appropriate for a N_2-N mixture in Section 3.2.1, Figure 3.9(b). The different set-ups are summarised in Table 3.6 together with a run identification number. The abbreviation NR stands for non-reacting.

Table 3.6: CFD simulations performed

Run number	V–T transfer	Electronic mode	CV model	Rates
NR	SSH	no	-	
1	MWP	no	CVDV	QK
2	SSH	no	CVDV	QK
3	MWP	no	Park TTv	Park

The two chemical reactions being considered in Run 1 to 3 are the irreversible molecule-molecule and molecule-atom dissociation of nitrogen

$$N_2 \ + \ N_2 \ \longrightarrow \ 2\,N \ + \ N_2$$
$$N_2 \ + \ N \ \longrightarrow \ 2\,N \ + \ N$$
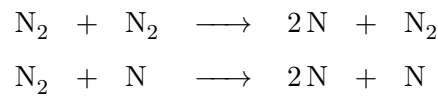
References and units of the Arrhenius rate constants shown in Table 3.7 are identical to the ones used in Section 3.1.4. Finally, two configurations associating a chemistry-vibration model with a set of chemical rates have been studied. They are also similar to those tested in Section 3.1.4 for zero-dimensional heat bath scenarios, namely *CVDV–QK* and *Park* that combines the Park TTv model with Park's rates.

Table 3.7: Mach 20 cylinder: parameters for the evaluation of k_f

Reaction rate	Reaction colliding partner	Arrhenius law constants		
		A	β	T_a
Park (1993) [7]	N_2	7.0×10^{21}	-1.6	113,200
	N	3.0×10^{22}	-1.6	113,200
QK (2015) [44]	N_2	2.47×10^{18}	-0.62	113,500
	N	6.02×10^{18}	-0.68	113,500

DSMC set-up   The variable hard sphere model is adopted with a temperature exponent of viscosity of 0.74, and a reference temperature of $T_{\text{ref}} = 273$ K. The particles impinging the cylinder wall are reflected diffusely with an accommodation coefficient equal to 1. Good DSMC practice have been satisfied for the mesh and the time-step. The cell size is equal to a third of the mean-free-path and a spline was used to minimize the region being modelled upstream the bow shock. The DSMC mesh, that is constructed with the *blockMesh* and *snappyHexMesh* OpenFOAM utilities, then consisted of 5.5 million cells. Each cell was filled with approximately 15 equivalent DSMC particles which resulted in simulations using over 80 million particles. The DSMC time-step was set to 1/5 of the mean-collision-time.

Results   The regions where the flow departs significantly from local thermodynamic equilibrium are highlighted in Fig. 3.15 using the local gradient-length Knudsen number and later shown in Fig. 3.19. This indicates that the CFD solver will be unlikely to provide satisfactory results within the bow shock and in the near-wake of the cylinder, as shown by Kn_{GLL} values above 0.05. In particular, the low density region for $\theta \simeq$ 130 deg is driving the Kn_{GLL} beyond 1. A very similar picture of Kn_{GLL} is observed for both reacting and non-reacting simulations.

As expected, the bow shock is more diffuse using the DSMC method as shown in
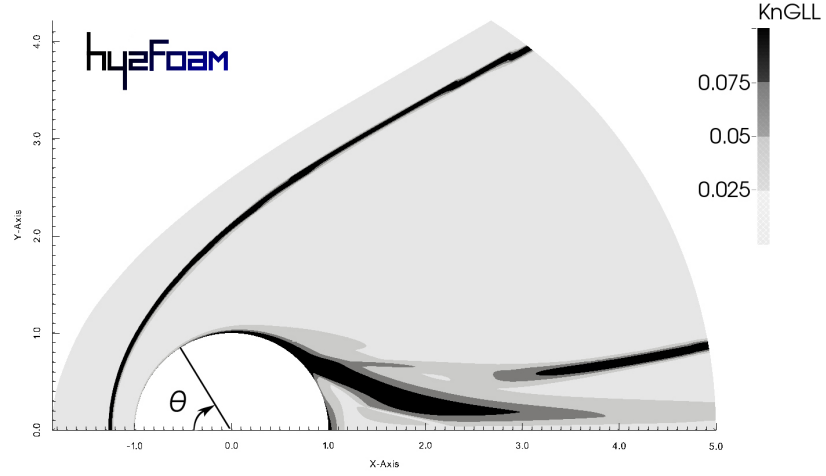
Figure 3.15: Mach 20 cylinder: local gradient-length Knudsen number for run 2

Fig. 3.16. The downstream shock position is nearly identical using both solvers. The temperature fields in Fig. 3.17(a) to 3.17(c) are correctly approximated using *hy2Foam* for $x < 0$, which corresponds to the region where the fluid undergoes compression. Unlike the non-reacting simulation which demonstrated a good agreement for the vibrational temperature field in the compression area, the discrepancies in Figure 3.17(d) are much larger in the whole domain when compared with DSMC. This can be explained by the application of the QK theory to capture the chemistry-vibration coupling and the use of the quantum Larsen-Borgnakke method in *dsmcFoam*, which promotes a quicker energy harmonisation in expansion regions (where $T_v > T_{tr}$) as reported in Section 3.1.4 using a zero-dimensional analysis. The Park combination used in run 1 is the instance which provides less accurate results with local vibrational temperatures above 10,000 K.

Figures 3.18(a) and 3.19(a) compare the stagnation line profiles of Mach number, temperature, and number density for non-reacting and reacting simulations as given by *hy2Foam* and *dsmcFoam*. It is evident that the shock stand-off distances are almost identical using both solvers and are approximately equal to 0.25 m in the reacting case, which is about 5 cm closer to the body than for the non-reacting case. The peak in trans-rotational temperature is correctly determined in the non-reacting case and using the *CVDV–QK* combination for both runs 1 and 2, and is slightly over-predicted using the *Park* combination. As shown previously in Figure 3.17(d), the trend in vibrational
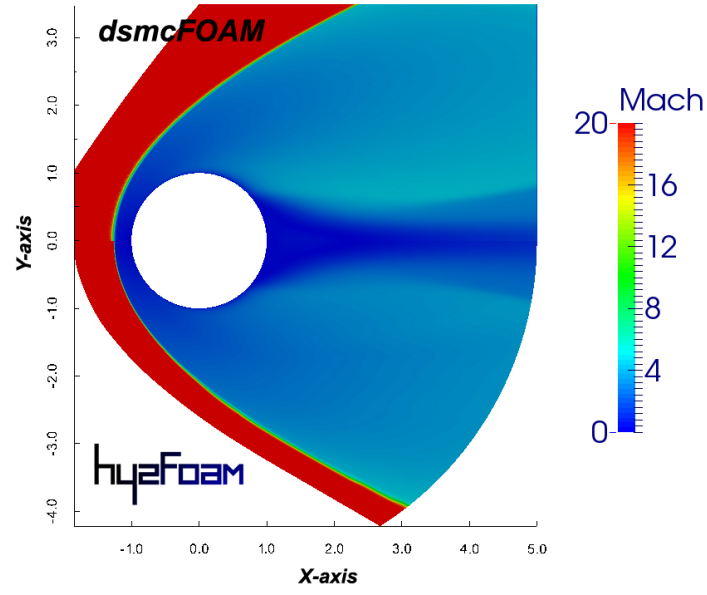
Figure 3.16: Mach 20 cylinder: Mach number CFD-DSMC flow-field comparison for run 2. The *dsmcFoam* solution is represented on the upper half and the *hy2Foam* solution on the lower half.

temperature shows a steeper increase across the shock wave. In Figure 3.19(c), the evolution of the species number densities for all runs is in satisfactory agreement with *dsmcFoam* outside of the $Kn_{GLL} > 0.01$ band. The early production of atomic nitrogen within the shock is not captured in the CFD solver due to the slight difference in shock thickness prediction.

Surface properties of pressure coefficient, skin friction and heat transfer are shown in Figures 3.20(a)-3.20(c) for both non-reacting (NR) and reacting simulations. There is a reasonable agreement between the CFD and DSMC solvers for $\mathcal{C}_p$ and $\mathcal{C}_f$.

The drag coefficient for each simulation is provided in Table 3.8 and this coefficient estimated by *hy2Foam* represents less than 2 % error when compared with *dsmcFoam* and the reacting environment does not significantly affect its magnitude. In addition, the values of *hy2Foam* and *dsmcFoam* are reasonably close to the one predicted by the Newtonian theory that is 4/3. The integrated heat flux, C_H, is however showing larger discrepancies between the two codes. There are several factors that could explain this observation: 1) a Kn_{GLL} number greater than 0.1 all around the cylinder, 2) a different treatment of the vibration-translational energy transfer between CFD and DSMC codes, and 3) the use of the KNP numerical schemes in *hy2Foam* that are known for being too dissipative in the near-wall region. It is also shown that the $CVDV-QK$ association

(a) Run NR, T_{tr}

(b) Run NR, T_v

(c) Run 2, T_{tr}

(d) Run 2, T_v
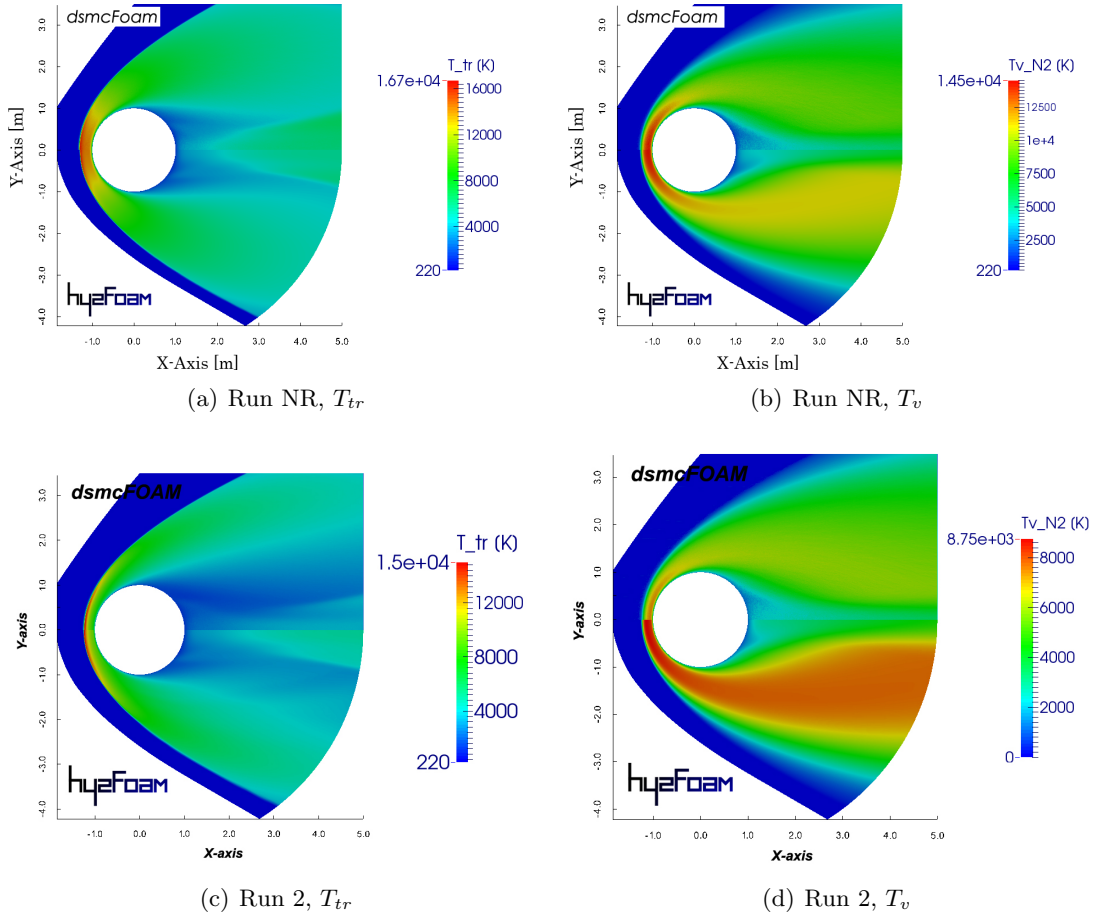
Figure 3.17: Mach 20 cylinder: temperature CFD-DSMC flow-field comparisons for runs NR and 2

is producing a 27 % larger integrated heat flux as compared with *dsmcFoam*, while the *Park* combination overpredicts C_H by 39 % in the present version of the *hy2Foam* code.

Table 3.8: Mach 20 cylinder: aerothermodynamic coefficients

CFD run number	C_D		C_H (kW)	
	CFD	DSMC	CFD	DSMC
NR	1.3	1.286	212	230
1	1.302		162	
2	1.302	1.284	161	126.6
3	1.304		176.2	
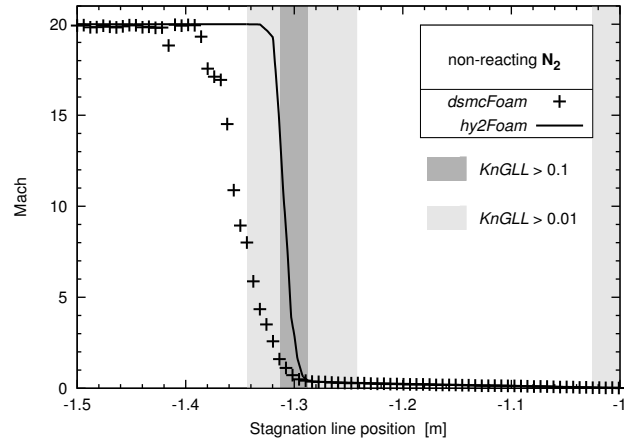
(a) Run NR: Mach number
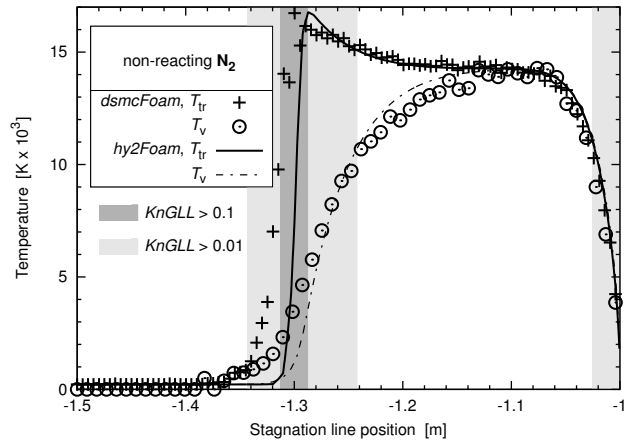
(b) Run NR: Temperature
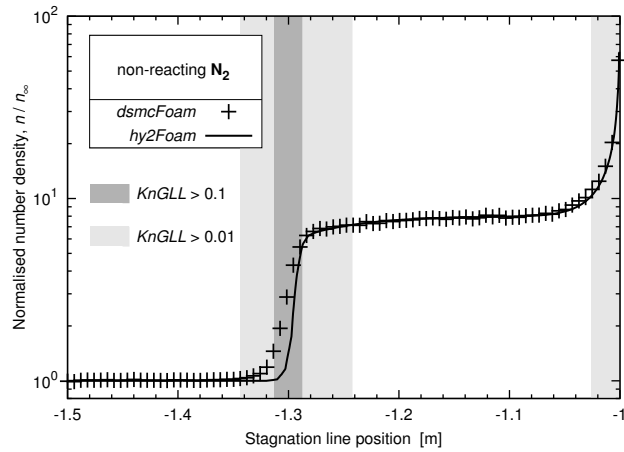
(c) Run NR: Number density

Figure 3.18: Mach 20 cylinder: stagnation line profiles for non-reacting simulations
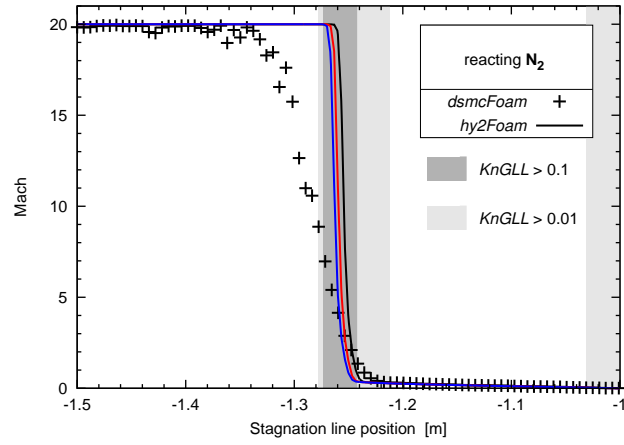
(a) Run 2: Mach number
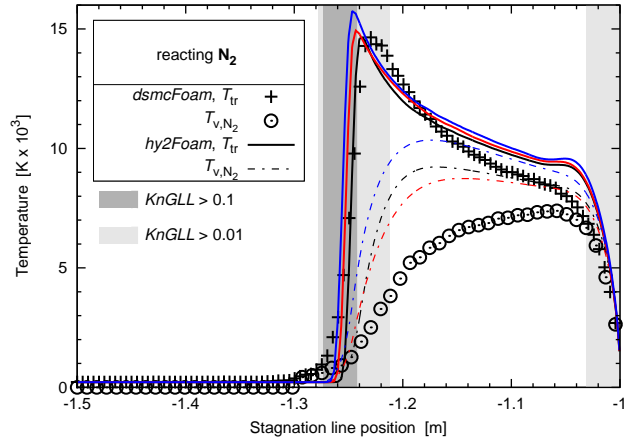
(b) Run 2: Temperature
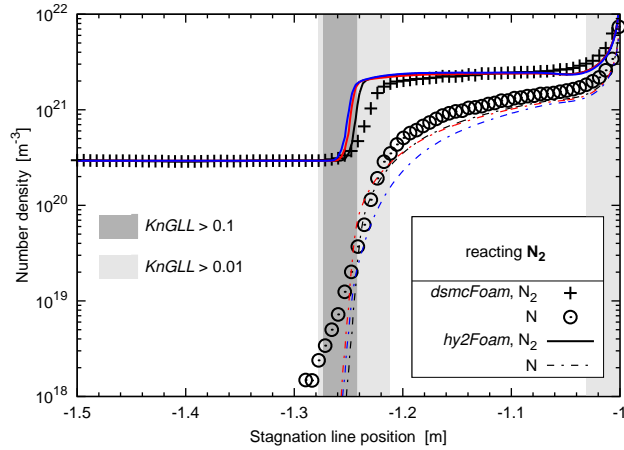
(c) Run 2: Number density

Figure 3.19: Mach 20 cylinder: stagnation line profiles for reacting simulations. CFD run 1: black lines, run 2: red lines, run 3: blue lines.
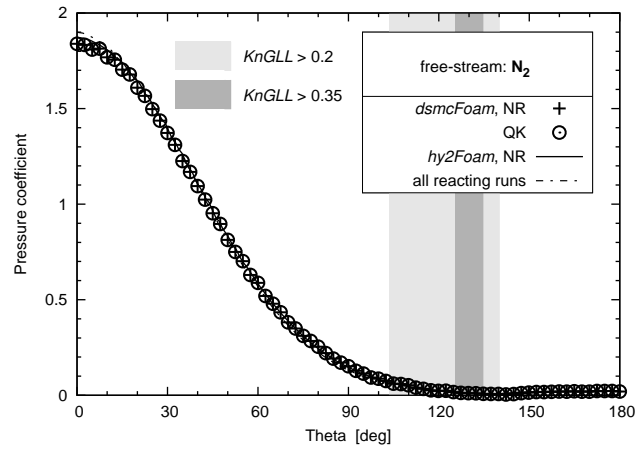
(a) Pressure coefficient
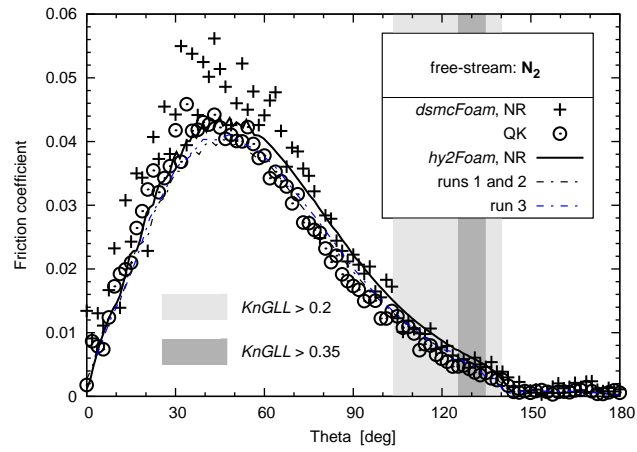
(b) Skin-friction coefficient
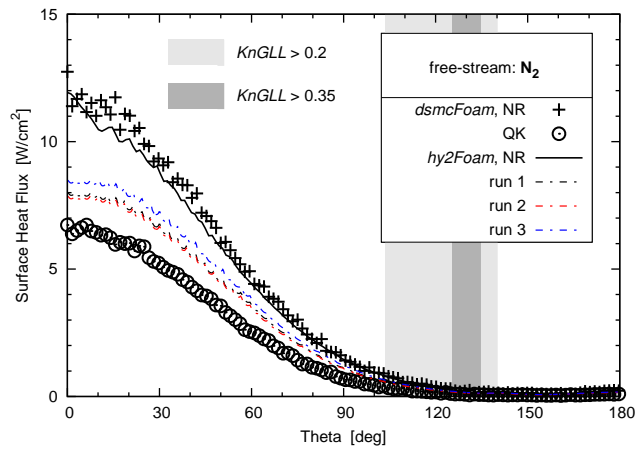
(c) Surface heat flux

Figure 3.20: Mach 20 cylinder: surface quantities around the cylinder.

Chapter 4

DSMC-derived QK Rates

This Chapter is concerned with reaction kinetics used in CFD solvers to model upper atmosphere hypersonic flows. Highly endothermic reactions of dissociation and ionization predominate at such speeds and contribute to significantly reduce the heat load at the vehicle surface. A correct prediction of the gas flow composition in the searing hot conditions of the atmospheric entry is therefore vital to missions including those beyond the Earth's proximity. The previous Chapter dedicated to Verification and Validation employed chemical rates present in well-established hypersonic solvers such as DPLR, LAURA or LeMANS. Those rates to be found in Refs. [7, 14, 127] were determined by Park two decades ago as a best-fit to experimental data for particular problems and are meant to be suited for a two-temperature CFD model. The adiabatic heat bath cases in Section 3.1.4 and the hypersonic cylinder case in Section 3.2.3 exemplified the use of these traditionally adopted chemical rates. However, to what extent can these rate constants be trusted, is there an alternative option for their estimation and what would be the influence of a new set of rate constants on the heat bath computations? Those are the questions that will be addressed in this Chapter.

4.1 Motivation

Chemical reaction rates which occur in an ionized gas at hypersonic speed are currently not well-known, and in fact, there exist flaws in the actual rates for some specific reactions. There are several reasons for this: a) difficulty for a reaction to be isolated,

71

b) uncertainty of measurements (caution must be exercised when the uncertainty in reaction rate constant exceeds one order of magnitude difference [113]), c) extrapolation from measured low-temperature equilibrium rates d) estimation from radiation measurements (*e.g.*, reactions involving NO) e) measurements polluted by other compounds, f) rates adapted from another reaction because of the absence of existing data [113].

Section 2.2.4 gave the background of the DSMC method featuring a quantum-kinetic (QK) chemistry framework. It emerged that despite its phenomenological nature, the QK model does not use any macroscopic quantity nor require the knowledge of reaction-fitted constants to enter into the calculations. Therefore, analytical solutions can be derived and DSMC appears as a suitable candidate to determine the speed of reactions that are involved in upper atmosphere hypersonic flows. The need for QK rates as an alternative solution for strongly endothermic reactions of dissociation and ionization has been expressed by Wysong *et al.* in 2012 [128]. Mention of other reaction types was not included because exchange reactions had issues in matching results from the classical kinetic theory at low temperatures [128]. This has later been circumvented by introducing two coefficients a and b to adjust the activation energy for each exchange and charge exchange reactions [44].

Previous authors [113–115, 129] discussed the use of QK theory as a means to describe the reaction rate versus temperature in an equilibrium gas, whether it was for a 5-species neutral gas, an 11-species ionized air mixture or an oxygen-hydrogen mixture. However, no Arrhenius coefficients were derived from these studies. In this Chapter, it is thus proposed to extract the relevant chemistry information from DSMC simulations using the *dsmcFoam+* solver. Extracting QK rates from *dsmcFoam* simulations was initiated in Ref. [44] for the 19 reactions (15 dissociation reactions and 4 exchange reactions) which occur in a 5-species air mixture. The set-up consisted in a zero-dimensional adiabatic heat bath similar to the one presented in Section 3.1.4. All three energy modes of translation, rotation and vibration were set to be in equilibrium at all times, and equilibrium rates were extracted in the form of the three Arrhenius coefficients: pre-exponential factor, A, temperature exponent, β, and activation energy, E_a. The electronic mode has been added to *dsmcFoam* lately, the code renamed

dsmcFoam+ [49] in consequence, and it is proposed firstly to revisit the chemical rates provided by Scanlon *et al.* [44] for dissociation and exchange reactions in Section 4.2, and then to extend the QK rate constants database to all 116 reactions occurring in an 11-species air mixture. Section 4.3 focuses on reactions that are the most likely to occur at high temperatures and the appropriateness of the rates derived in Section 4.2 is evaluated in Sections 4.4 and 4.5 using heat bath simulations. Finally, future prospects are discussed in Section 4.6.

4.2 Equilibrium rates

This section is dedicated to the determination of the reaction rate constants for all 116 reactions active in an 11-species air mixture. Reactions are considered individually and no splitting can occur, that is when two particles are selected for collision the procedure described in Section 2.2.4 applies but if a reaction is to occur the particles are left unchanged while the reaction counter is augmented by one. Therefore, the energy of the system remains constant and no products are formed. This allows sampling of the rate constant over time and the final value is obtained after convergence of the rate, which usually takes place within 1,000 iterations as shown in Figure 4.1(a). In addition, the equilibrium rates calculation necessitates all of the rotational, vibrational and electronic collision numbers to be set to unity.

Two reacting species are introduced in equal molar proportions, with the exception of electron impact reactions for which the heat bath is filled with 0.5 % electrons. 100,000 equivalent DSMC particles are simulated and the total mixture number density is equal to 1×10^{23} m^{-3}, while the time-step is set to 1×10^{-10} s for electron impact reactions and to 1×10^{-9} s otherwise.

Two electronic energy level datasets are utilized for comparison. Set 1 is from Gurvich *et al.* [130] as referenced by Hash [131] and is typically used in CFD computations. In this dataset, atomic nitrogen and atomic oxygen have five electronic energy levels, which has been lowered to three in this study. Indeed, the first two electronic levels have been merged with the ground energy level due to their relatively small characteristic electronic temperature. Set 2 is the one employed in the *dsmcFoam* code and originates from the work of Liechty [129]. Liechty combined the electronic dataset shown in Hash

with that of Johnston [132], thus augmenting the electronic energy levels for species O, N and N^+, as shown in Appendix B.

A series of python algorithms have been written to browse through the reactions present in the DSMC chemistry dictionary. As an example for one of these reactions it works as follows:

- MAIN SCRIPT:

    - Read the input file (reaction string, reaction activation energy, temperature data points)

    - Pass information onto the script responsible for the *dsmcFoam* simulations

- SIMULATION SCRIPT:

    - Set-up the DSMC case folder and single out the one reaction in the DSMC chemistry folder

    - for each temperature data point, Do

        * Run the simulation until convergence of the reaction rate (with a minimum of 1,000 iterations)

        * Sample across several independent runs (optional)

        * Plot the time evolution of the chemical rate

        * Write to file the final reaction rate value

- MAIN SCRIPT:

    - Run the chemistry script

- CHEMISTRY SCRIPT:

    - Determine the set of Arrhenius coefficients corresponding to the reaction rate (E_a is given as an input, A and β are guesses) as explained below.

    - Plot the DSMC equilibrium rate and the Arrhenius solution versus temperature

- MAIN SCRIPT:

− Write the Arrhenius coefficients in the *hy2Foam* format

The Arrhenius coefficients are obtained by inverting a system of the form $\boldsymbol{M}\,\boldsymbol{x} = \boldsymbol{k}$ where $\boldsymbol{M}$ is a matrix and $\boldsymbol{x}$ and $\boldsymbol{k}$ are vectors. This is done in python using the *NumPy* package and in particular the functions *zeros()*, *linalg.pinv()*, and *dot()*.

This procedure is repeated for all reactions and for the two electronic datasets when relevant. Results are classified by types of reaction and are shown in the subsequent subsections for temperatures ranging from 1,000 K up to 40,000 K.

4.2.1   Dissociation

The time evolution of the reaction rate constant for the molecule-molecule dissociation of nitrogen (reaction 1a) at a temperature of 10,000 K is shown in Figure 4.1(a). Rate convergence is reached before the end simulation time and the final rate of 3.79×10^{-19} m^3 molecule^{-1} s $^{-1}$, that is in reasonable agreement with QK analytical data given by Bird's program QKrates.EXE [133], is then reported in Figure 4.1(b). This latter Figure compares reaction rate results from *dsmcFoam+*, the output of the python algorithm for a temperature varying between 5,000 K and 40,000 K, and the rate constant from Park [7] that is adopted in CFD computations.

It can be seen that the Arrhenius solution is passing through all DSMC data points which gives confidence in the capabilities of the algorithm to find a suitable solution for reactions whose rates are yet to be determined. There is a 1 to 2 multiplication factor (1.68 at 10,000 K) between the reaction rate obtained by the algorithm and the rate given by Scanlon *et al.* using *dsmcFoam* [44] after a correction was made to reaction classes involving similar species[1]. The rate constant from Park [7] is also shown and appears to predict a lower reaction speed throughout most of the temperature range.

Figure 4.2 presents the rate constants for two other dissociation reactions involving the oxygen molecule and nitric oxide. The Arrhenius solution is matching well the DSMC data and the previous results from Scanlon *et al.* [44]. The discrepancies with Park's rate constants are seen to be reduced for these reactions.

A summary of all DSMC-derived dissociation reaction rates arranged by molecule

---

[1]The implementation of this fix is an ongoing work for reactions other than dissociation. For reasons of consistency, the correction for dissociation reactions is disregarded in the rest of this Chapter.
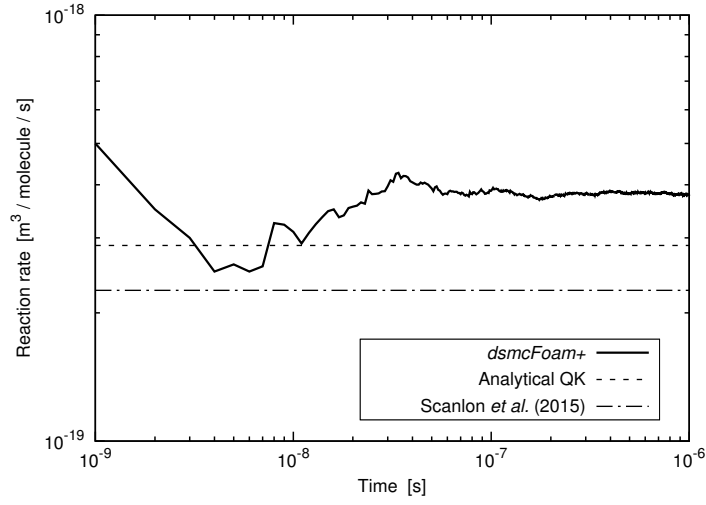
(a) Time evolution of the reaction rate at 10,000 K
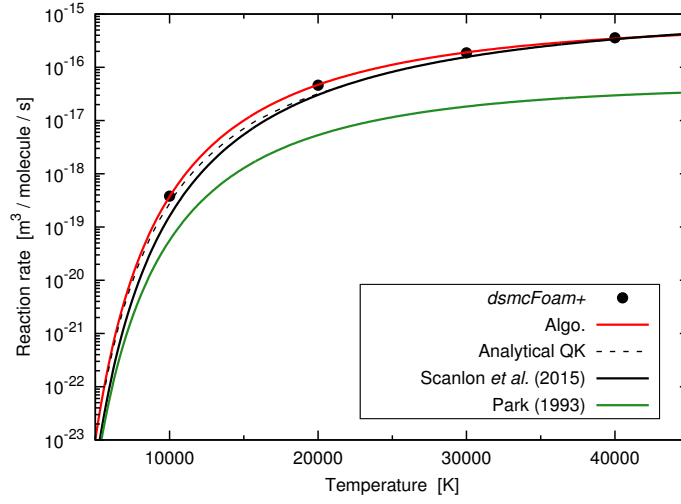
(b) Reaction rate versus temperature

Figure 4.1: Reaction rate for reaction 1a: $N_2 + N_2 \longrightarrow N + N + N_2$

is given in Figure 4.3 and the Arrhenius coefficients are reported in Appendix C.

4.2.2   Ionization

Ionization reactions other than associative ionization and electron impact ionization are not part of the reaction databases such as that of Park [7, 14] and Liechty [129] due to their high energy of activation (greater than 13 eV) which makes them unlikely to occur during re-entry case scenarios. They are, however, considered in this work and the algorithm output for ionization reactions $O_2 + O_2 \longrightarrow O_2^+ + e^- + O_2$ and

(a) Reaction 2g: $O_2 + N \longrightarrow O + O + N$ (b) Reaction 3e: $NO + O_2 \longrightarrow N + O + O_2$
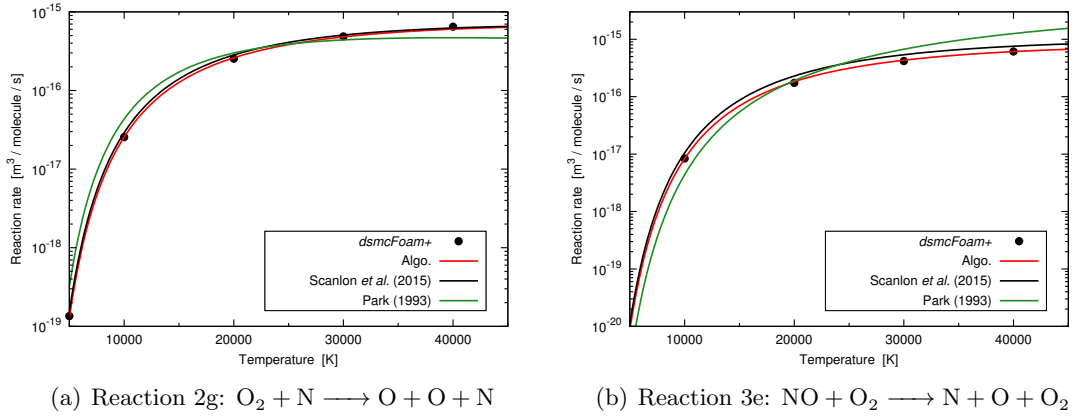
Figure 4.2: Reaction rates versus temperature for dissociation reactions 1 and 12

$O + O \longrightarrow O^+ + e^- + O$ is given in Figure 4.4. The algorithm provides once again an acceptable fit to the DSMC data for both reactions.

Interestingly in Figure 4.4(b), the electronic configuration of atomic oxygen has a major influence on the reaction rate constant as there is more than one order of magnitude difference between the two datasets. This can be explained by the fact that the electronic set 2 for O has many more electronic levels than set 1 (32 versus 3, respectively, as outlined in Table B1). The energy available for ionization that is the sum of the relative translational energy of the colliding pair and the electronic energy of the particle considered for ionization is therefore higher for the second configuration which in turn results in a greater potential for ionization. The underlying question concerns the number of electronic energy levels that should be allocated to atomic nitrogen and oxygen in both CFD and DSMC codes. There is no consensus in the literature about the electronic level cut-off value for each species [134, 135]. Evaluation and criticism of the outcome provided by the different existing methodologies are beyond the scope of this work. Finally, the rates for the 50 ionization reactions present in *dsmcFoam+* can be found in Tables C4 - C9.

4.2.3   Electron impact dissociation

The speeds of the three electron impact dissociation (eid) reactions for the N_2, O_2, and NO molecules are presented in Figure 4.5. These reactions resulting from the collision with an electron are shown to have rate constants nearly two order of magnitude greater
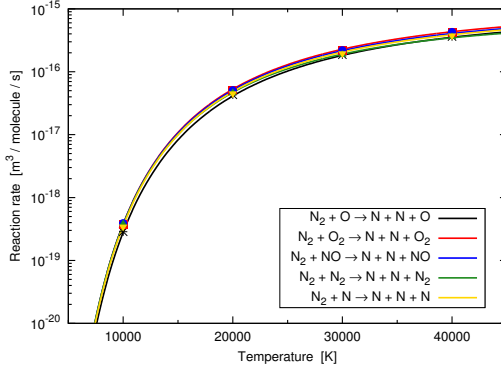
(a) Dissociation of N_2, neutral reactant partner
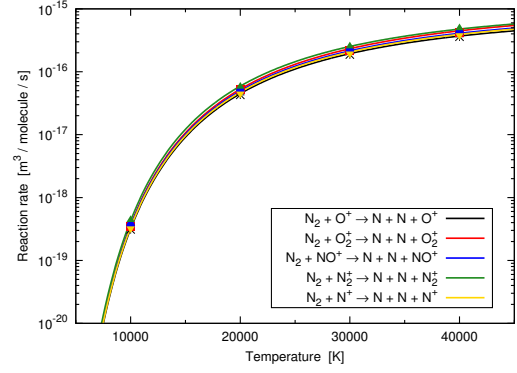
(b) Dissociation of N_2, ionised reactant partner
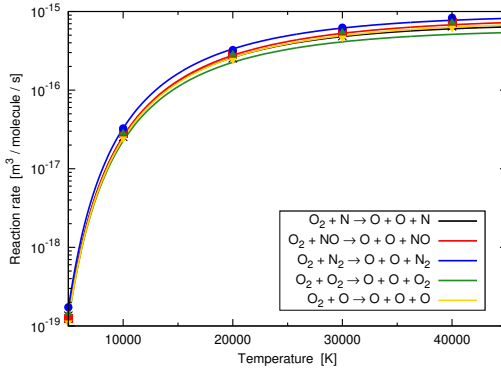
(c) Dissociation of O_2, neutral reactant partner
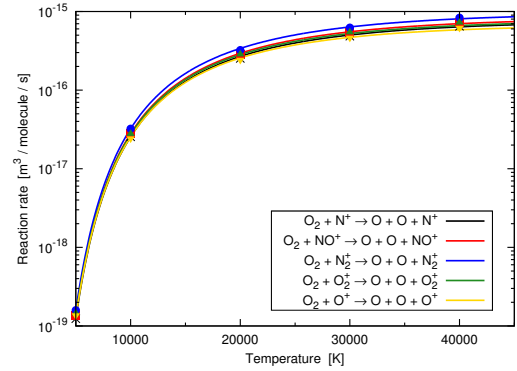
(d) Dissociation of O_2, ionised reactant partner
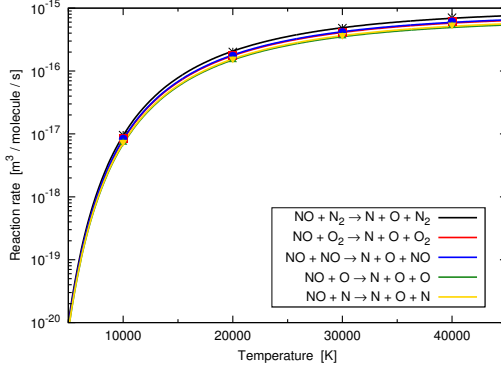
(e) Dissociation of NO, neutral reactant partner
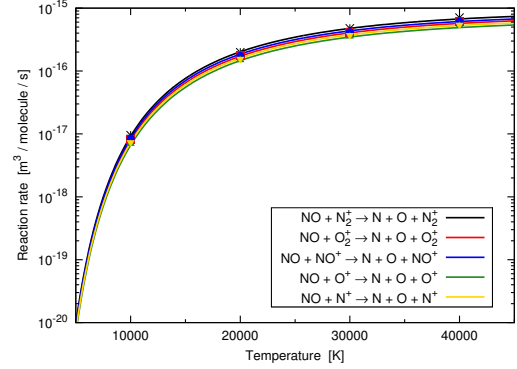
(f) Dissociation of NO, ionised reactant partner

Figure 4.3: DSMC-derived reaction rates versus temperature for dissociation reactions

than dissociation reactions involving heavy-particles. One of the strengths of the QK framework is that the reaction rate is limited by the collision rate: at very high temperatures the reaction rate cannot be greater than the collision rate which is a priori not guaranteed by the Arrhenius law. Since the collision rate of the $(N_2 - e^-)$ pair is higher than any other $(N_2 - M)$ pairs, M being a reactant partner with $M \in N_s \setminus \{e^-\}$, it is

(a) Reaction 6a: $O_2 + O_2 \longrightarrow O_2^+ + e^- + O_2$ (b) Reaction 9a: $O + O \longrightarrow O^+ + e^- + O$
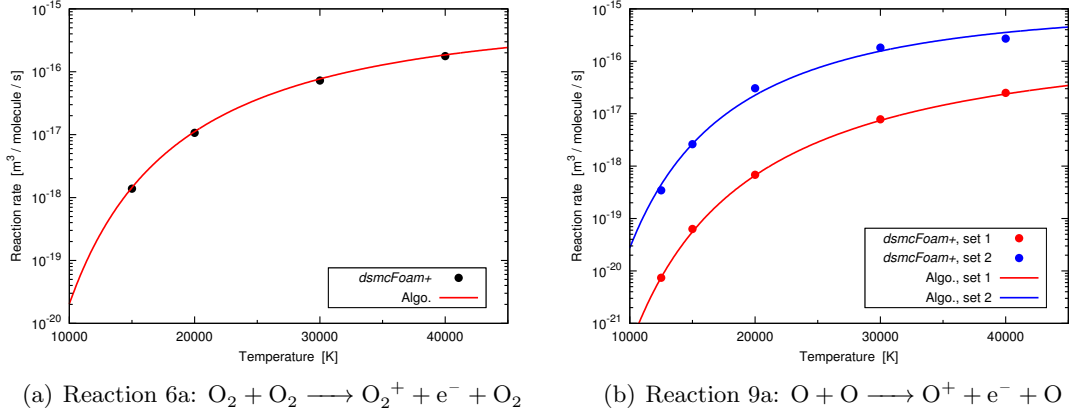
Figure 4.4: Reaction rates versus temperature for ionization reactions 6a and 9a

logical that the reaction rate of $(N_2 - e^-)$ is higher at elevated temperatures. Besides that, Park's solution for the $N_2 - e^-$ eid reaction appears to be a fair approximation of the DSMC results.
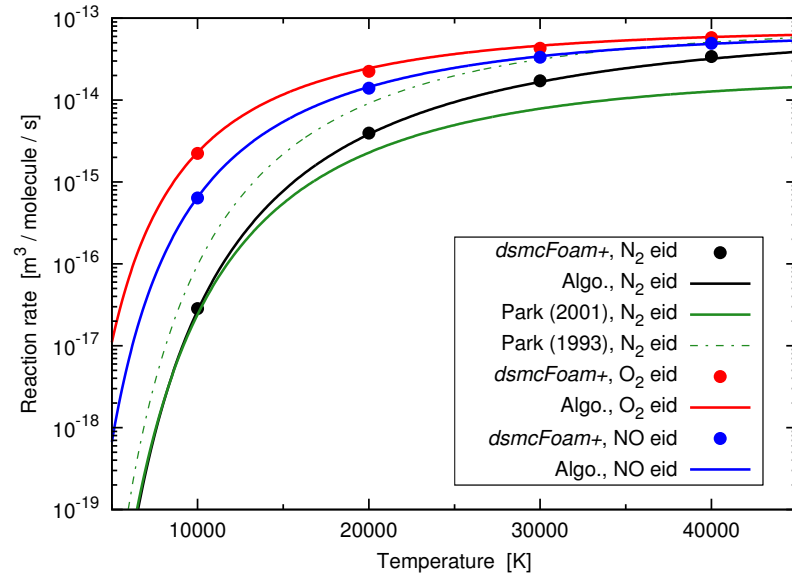
Figure 4.5: Reaction rates versus temperature for electron impact dissociation (eid) reactions 4, 5 and 6

4.2.4   Electron impact ionization

With a molecule   A similar remark to that of eid reactions can be made for electron impact ionization (eii) reactions. The evolution of the rate constants versus temperature is given in Figure 4.6 for collisions involving a molecule. The algorithm is still producing

a solution that is in reasonable agreement with the DSMC data.
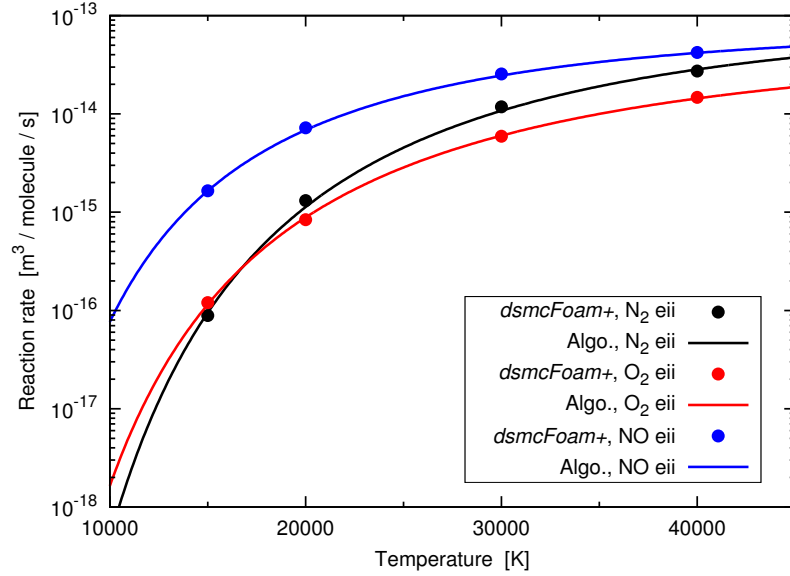
Figure 4.6: Reaction rates versus temperature for electron impact ionization (eii) reactions 10, 11 and 12

With an atom   For the electron impact ionization of an atom (see Figure 4.7), the number of electronic levels retained matters and it is again responsible for large discrepancies (one or two orders of magnitude difference) in the rate constant at high temperatures. Park's rate is found to be somewhat in between the two solutions given by the algorithm for $T < 20,000$ K and reaches a plateau for $T > 30,000$ K.

4.2.5   Associative ionization

Forward associative ionization   A description of forward associative ionization is based on the $N + N \longrightarrow N_2^+ + e^-$ reaction since they all exhibit a similar trend with temperature. DSMC data are relatively well approximated by an Arrhenius fit as shown in Figure 4.8. The influence of the electronic set-up is still noticeable but is worth less than one order of magnitude. Arrhenius coefficients for these two best-fits can be found in Table C10. In addition, the DSMC solution is shown to produce a rate constant at least an order of magnitude lower as compared with Park's data [127].
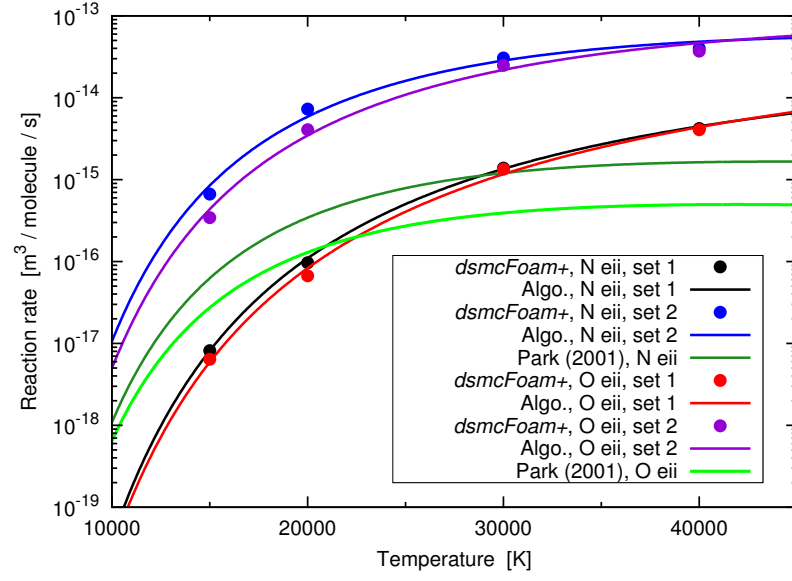
Figure 4.7: Reaction rates versus temperature for electron impact ionization (eii) reactions 13 and 14
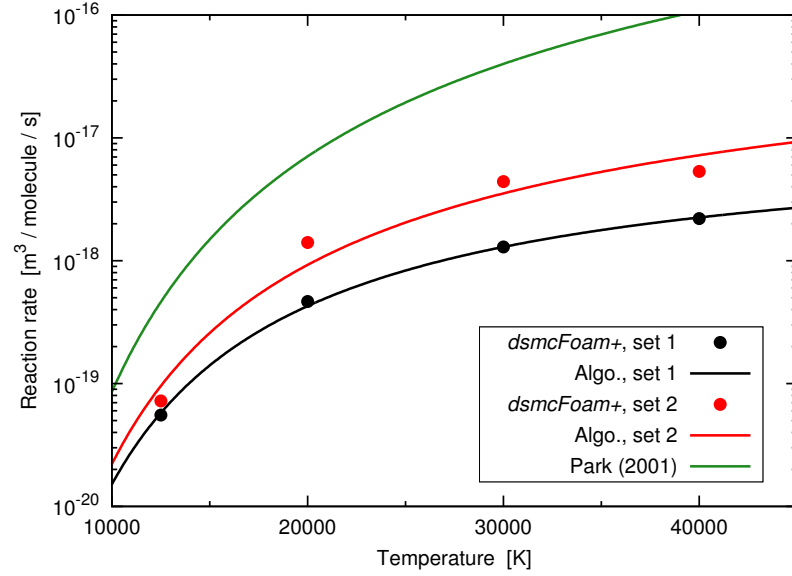
Figure 4.8: Reaction rates versus temperature for forward associative ionization reaction 19a

Reverse associative ionization Reverse associative ionization on the other hand cannot be fitted by an Arrhenius law. The rate constant for the reaction $N_2^+ + e^- \longrightarrow N + N$, that is representative of all three reverse associative ionizations, is given in Figure 4.9. The electronic set-up does not have an effect on the solution since the N_2^+ reactant is not concerned with this issue. The entire temperature range is subdivided into two sub-ranges and a linear interpolation is performed in-between (that is the

solid red curve in Figure 4.9) within a given temperature interval to smoothen the rate constant profile. Therefore, two sets of Arrhenius constants are given for each of the reverse associative ionization reaction in Table C11. The QK solution is again shown to be in disagreement with Park's profile over the whole temperature range.
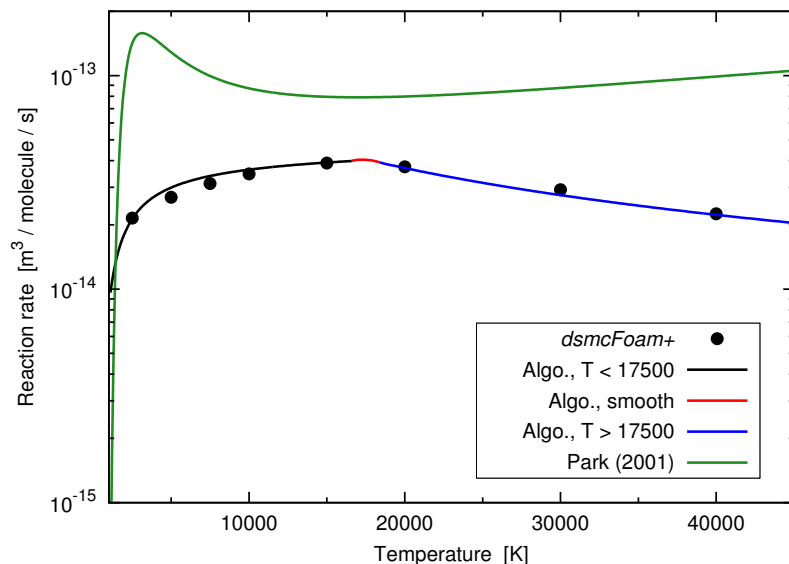
Figure 4.9: Reaction rates versus temperature for reverse associative ionization reaction 19b

4.2.6   Exchange and charge exchange

Fitting an Arrhenius profile for the entire temperature range is impossible for most exchange / charge exchange reactions if a close agreement wants to be achieved between DSMC data and the output of the algorithm. The procedure involving temperature-dependent Arrhenius coefficients detailed in the previous paragraph is repeated here and shown in Figure 4.10 for forward and reverse exchange reactions 22a and 24b, and in Figure 4.11 for forward and reverse charge exchange reactions 29a and 29b. The resulting Arrhenius coefficients are reported in Tables C12 - C15.

4.2.7   Partial conclusion

While reconciling the DSMC and CFD chemistry modules is unfeasible due to the two fundamentally different approaches described in Sections 2.1.6 and 2.2.4, it is thought that the DSMC and CFD solutions of practical engineering cases lying in the near-

(a) Forward exchange 22a: $N_2 + O \longrightarrow NO + N$ (b) Reverse exchange 24b: $O_2 + N \longrightarrow NO + O$
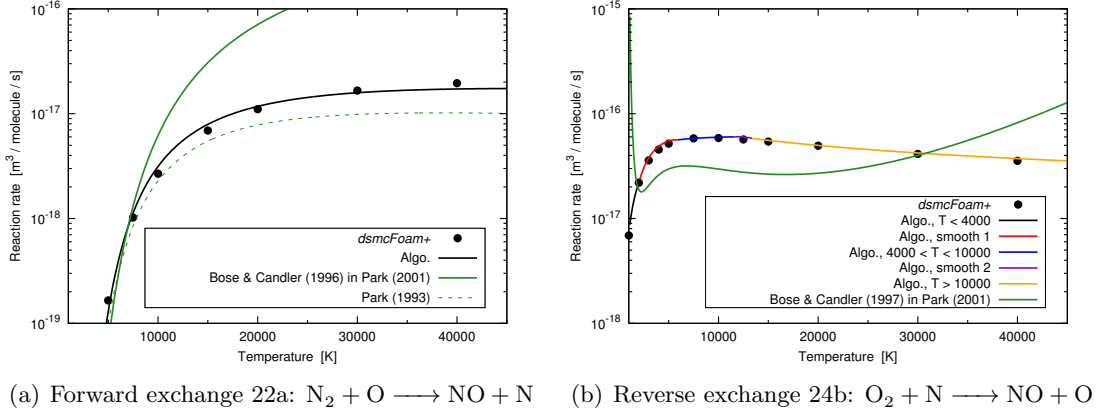
Figure 4.10: Rate constants versus temperature for forward and reverse exchange reactions 22a and 24b

(a) Forward charge exchange 29a: $N_2 + N^+ \longrightarrow N_2^+ + N$ (b) Reverse charge exchange 29b: $N_2^+ + N \longrightarrow N_2 + N^+$
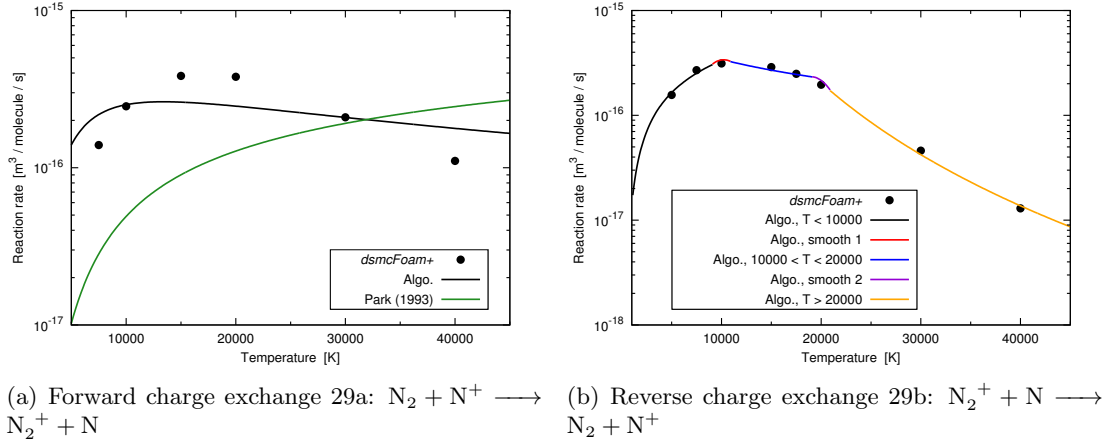
Figure 4.11: Rate constants versus temperature for forward and reverse charge exchange reactions 29a and 29b

continuum regime would present an improved concordance if the temperature evolution and species fates were to match reasonably well for every reaction taken in isolation. Equilibrium rate constants have been derived from the use of *dsmcFoam+* for 116 chemical reactions relevant to the high-speed regime and can be found in Appendix C. Some of these DSMC-derived rate constants have shown to be in major disagreement with Park's rates and some others have shown to be affected by the electronic set-up retained. In addition, rate constants were also given for reactions (ionizations, electron impact dissociations of O_2 and NO, electron impact ionizations of N_2, O_2 and NO) that are usually excluded from hypersonic simulations. In the next two sub-sections, the focus is set on reactions that are the most likely to occur in a high-temperature

environment and on the application of the Arrhenius coefficients derived therein to heat bath cases with particle splitting.

4.3   Dominant reactions in a high-temperature environment

Rate constants for the most probable reactions occurring at hypersonic speed should be treated with special care. The aim of this short section is to find out quantitatively what reactions are the most likely to be taking place in a high-temperature environment that could be typical of a hypersonic re-entry flow. The gas mixture is assumed to be heated at temperatures close to a target temperature, T_{target}.

Heat bath simulations for a 0.8 N_2 + 0.2 O_2 air mixture are run with a time-step of 1×10^{-10} s for various initial temperatures that are in excess of $T_{\text{excess}} = 2,000$ K for the following target temperatures: 10,000 K, 20,000 K, 30,000 K and 40,000 K. The simulations are started and an immediate decrease in temperature is observed as a consequence from the rapid thermo-chemical relaxation. Once the temperature is below the threshold defined as $T_{\text{target}} - T_{\text{excess}}$, the simulation is stopped. Figures 4.12 and 4.13 provide histograms for the four target temperatures and results are ensemble averages over five statistically-independent DSMC computations. To improve reaction identification, each type of reaction is associated with a colour: dissociation (pale yellow), electron impact dissociation (orange), ionization (light blue), electron impact ionization (dark blue), associative ionization (green), exchange (red) and charge exchange (violet).

On the abscissa axis the number of occurrences for one specific reaction over the total number of reactions is represented which allows the sorting of the reactions into groups, and on the ordinate axis for each reaction the frequency of activation in *dsmcFoam+* is shown, as defined by the ratio of the number iterations for which the reaction was active (*i.e.* occurred at least once) to the total number of iterations.

At 10,000 K, it is no surprise to find dissociation (and in particular the one of O_2 resulting from collisions with N_2) and exchange reactions due to their lower activation energies. As the temperature increases in Figure 4.12(b), electron impact dissociation
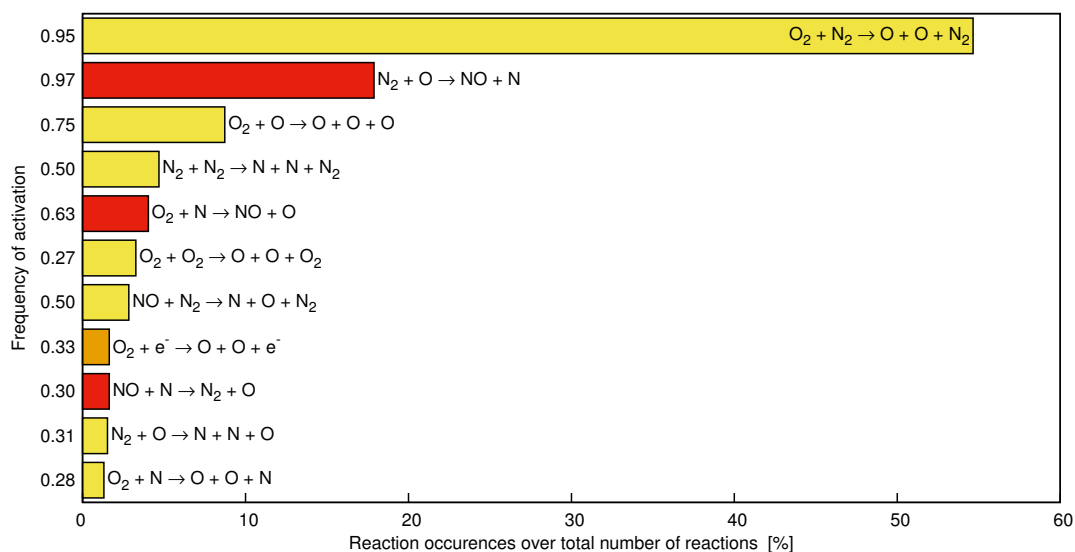
(a) $T_{\text{target}} = 10{,}000$ K
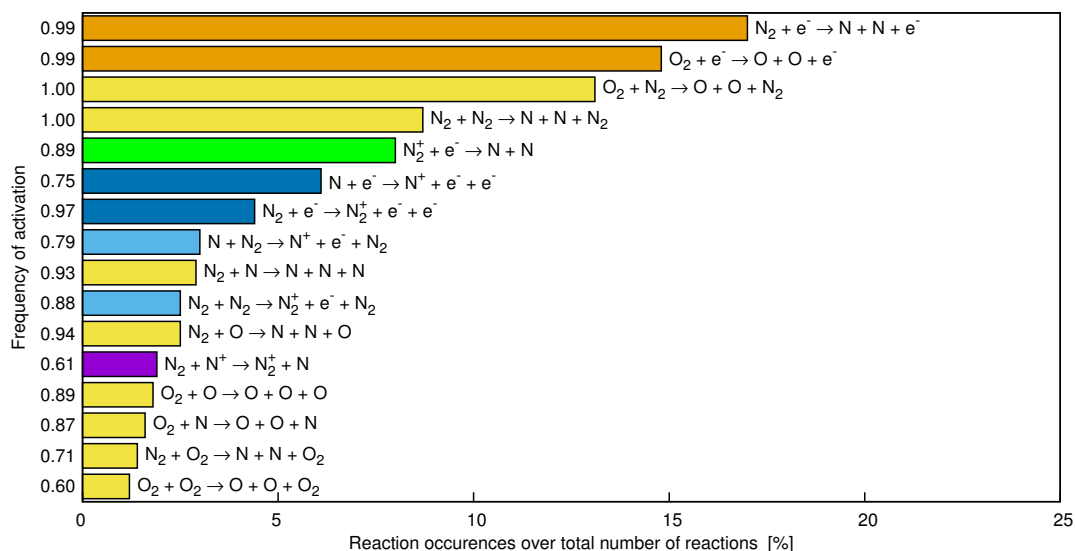
(b) $T_{\text{target}} = 20{,}000$ K

Figure 4.12: Reactions above the 1 % threshold at temperatures close to T_{target} for $T_{\text{target}} \leq 20{,}000$ K

of N_2 and O_2 rapidly takes over because of their activation energies that equal that of regular dissociation reactions combined with the much greater speed at which electrons travel. Reactions involving NO are not present anymore in the reactions list above a 1 % threshold. After further increase in temperature (see Figure 4.13), ionization and electron impact ionizations of N_2 become increasingly prominent, and O_2 is less well

represented because of the initial composition of the mixture and its rapid depletion.
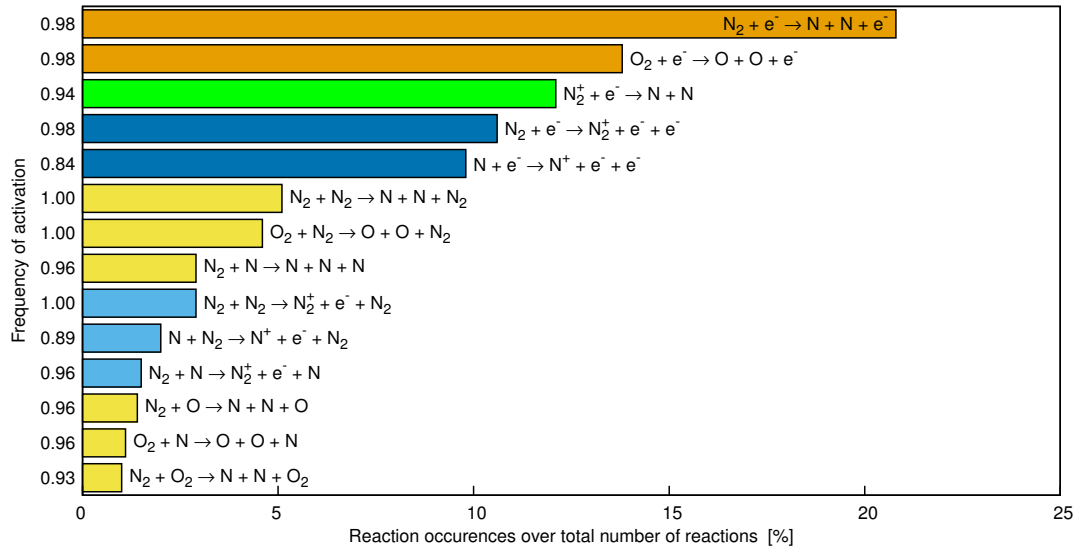
(a) $T_{\text{target}} = 30{,}000$ K
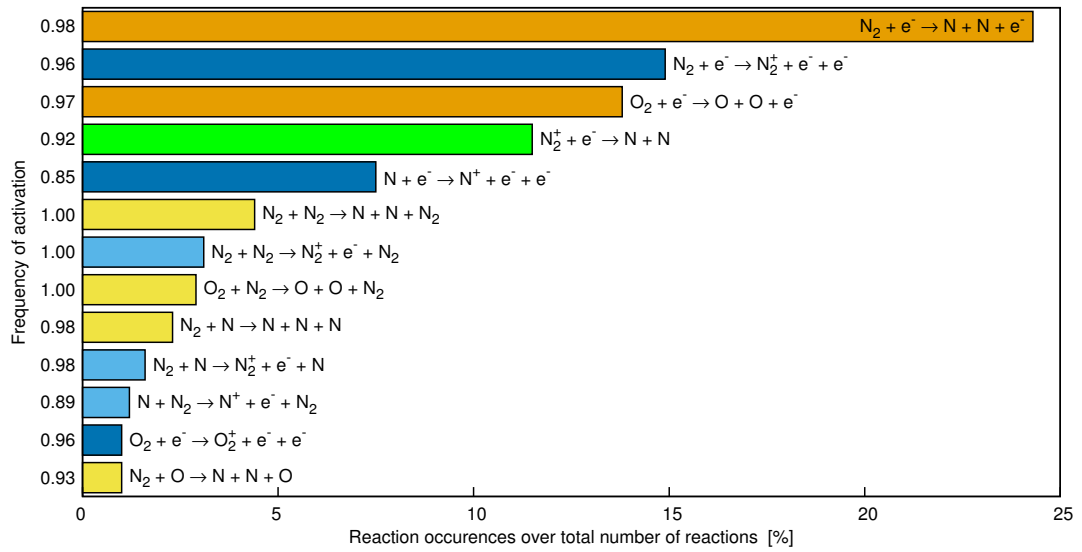
(b) $T_{\text{target}} = 40{,}000$ K

Figure 4.13: Reactions above the 1 % threshold at temperatures close to T_{target} for $T_{\text{target}} \geq 30{,}000$ K

4.4   Splitting cases

This section addresses the problem of heat bath cases that enable particle splitting for reactions taken in isolation. The algorithm presented in Section 4.2 has been slightly modified for this aim. Dissociation reactions will not be covered as they have already been discussed in Scanlon *et al.* [44] and also because the addition of the electronic energy mode does not affect their rate constant. The heat bath simulations set-up is identical to that of the previous subsection.

4.4.1   Ionization

The ionization reaction $N_2 + N_2 \longrightarrow N_2{}^+ + e^- + N_2$ is selected because it has shown to be the most recurrent ionization reaction for an air mixture at high temperatures in Section 4.3. For a temperature of 30,000 K, the thermo-chemical relaxation for this reaction is given in Figure 4.14. There is a fair agreement over time in terms of temperature and an excellent agreement for species number densities between the CFD and DSMC solvers. Therefore, the Arrhenius parameters determined in Section 4.2.2 can be transposed to a real-world application without any modification.

(a) Temperature versus time

(b) Normalised number densities versus time
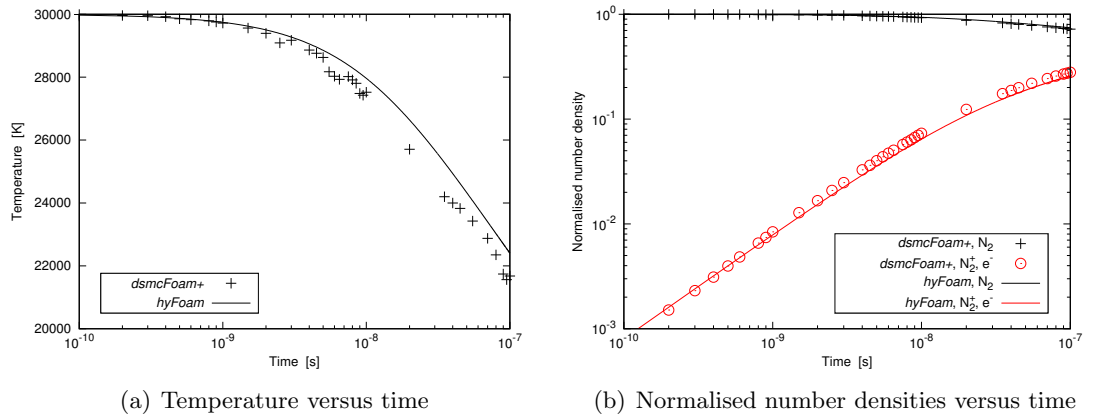
Figure 4.14: Heat bath with splitting enabled for reaction 5a: $N_2 + N_2 \longrightarrow N_2{}^+ + e^- + N_2$

4.4.2   Electron impact dissociation

The solution for the electron impact dissociation of N_2 is shown in Figure 4.15 for both electronic set-ups. A very reasonable agreement is found for set 1 and the temperatures predicted by the CFD solver for both reaction sets at 1 μs equal that of DSMC. The

number of electronic levels of atomic nitrogen plays a significant role as the temperature difference exceeds 5,000 K as the case reaches near-thermal equilibrium. Results using Park's rate constant [7] are added and are shown to give a temperature decrease close to that of set 1 but with species concentrations that of set 2.

(a) Temperature versus time

(b) Normalised number densities versus time
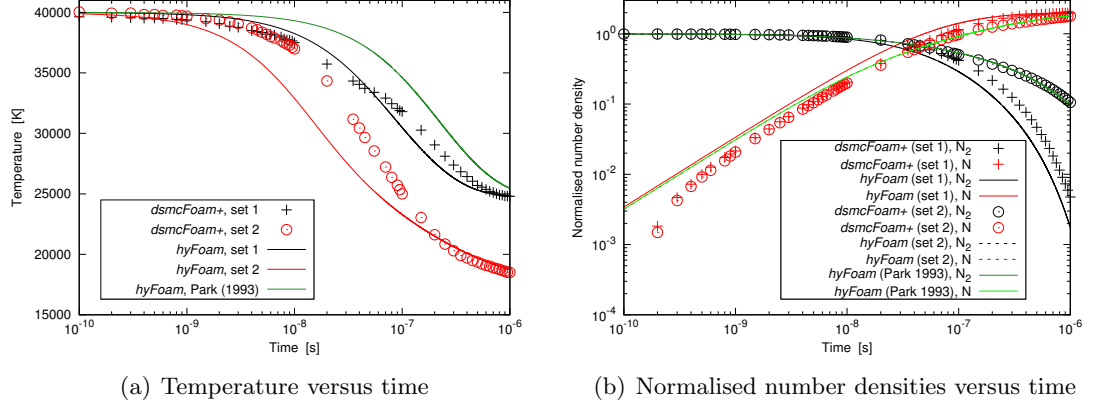
Figure 4.15: Heat bath with splitting enabled for reaction 4: $N_2 + e^- \longrightarrow N + N + e^-$

4.4.3   Electron impact ionization

Discrepancies between the CFD and DSMC solutions appear to grow larger when considering of electron impact ionization (eii) reactions. Figure 4.16(a) presents heat bath temperature results for the eii of O and they are unsurprisingly highly-dependent on the electronic set-up. The uncorrected profiles are obtained using the standard Arrhenius law. Hoffert and Lien [136] studied collisional ionization kinetics of singly ionized argon and pointed out that the forward rate constant was best approximated by an Arrhenius law amended as follows

$$k_f(T) = A' \, T^{\beta'} \times \left(\frac{E'_a}{k_B \, T} + 2 \right) \, exp \left(-\frac{E'_a}{k_B \, T} \right) \qquad (4.1)$$

where A', β', and E'_a are adjusted Arrhenius coefficients. The solution for $A' = 0.01 \, A$, $\beta' = \beta$ and $E'_a = E_a$ is shown using solid lines and reported in Figure 4.16(b). With regard to these results, it appears evident that all electron impact reactions should be tuned individually, whether it is a dissociation or ionization reaction. This is left as future work.

(a) Temperature versus time

(b) Normalised number densities versus time
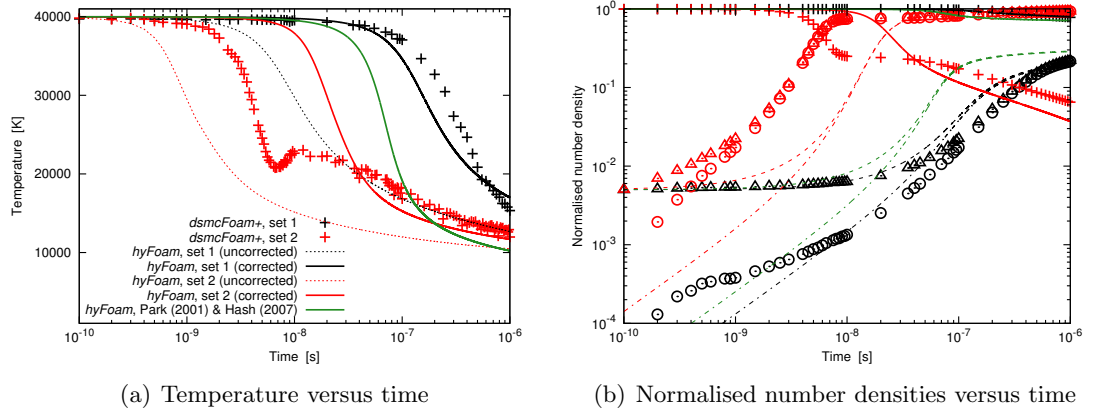
Figure 4.16: Heat bath with splitting enabled for reaction 14: $O + e^- \longrightarrow O^+ + e^- + e^-$

4.4.4 Associative ionization

Forward associative ionization for the oxygen atom can be seen in Figure 4.17. A good agreement is found for both electronic sets but the two solutions exhibit a different trend. Indeed, the use of set 1 yields a temperature decrease while the use of set 2 results in a small increase in temperature after 10 μs. Since forward associative ionizations are endothermic, it can be concluded that the addition of electronic levels to atomic neutral species only in set 2 is creating an energy imbalance between atoms and molecules resulting in the anomalous behaviour observed in Figure 4.17(a). Finally, the solution that uses Park's rates [127] with the electronic data of Hash [131] (that corresponds to set 1) is shown to substantially overpredict the speed of this reaction.

(a) Temperature versus time

(b) Normalised number densities versus time
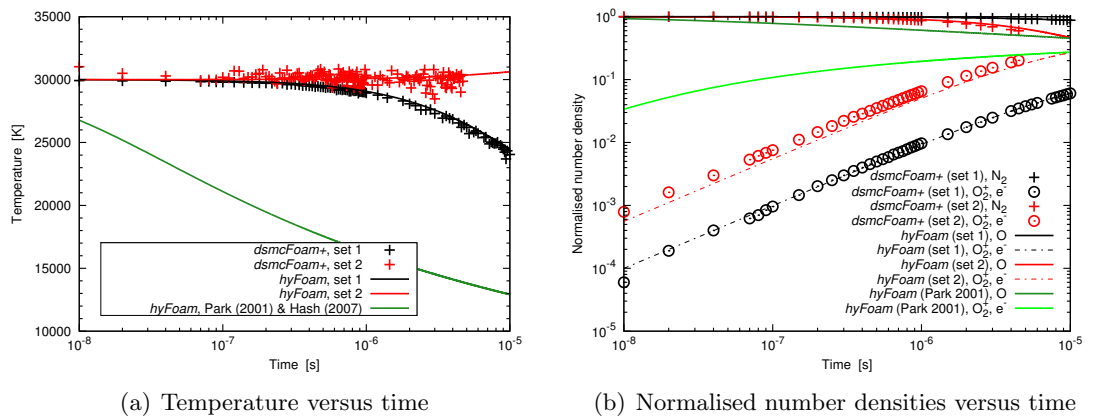
Figure 4.17: Heat bath with splitting enabled for reaction 21a: $O + O \longrightarrow O_2^+ + e^-$

4.4.5   Exchange

Exchange reactions are illustrated with the exact same two reactions that were chosen in Section 4.2.6 when deriving the Arrhenius coefficients. In Section 4.3, they were shown to be in the top 5 of the most abundant reactions at 10,000 K. The initial temperature is here increased up to 20,000 K and the results are shown in Figure 4.18. Although the rate constants appeared to be independent from the electronic set-up, the temperature solution is not. The equilibrium temperatures are not recovered but this was not the case without the inclusion of the electronic energy mode in Ref. [44], that is shown in Figure 4.18 with the mention *no E_{el}*. Overall, the discrepancies between the CFD and DSMC solvers do not appear to be substantially affected by the choice of the electronic set-up.

(a) Temperature versus time

(b) Normalised number densities versus time

(c) Temperature versus time

(d) Normalised number densities versus time
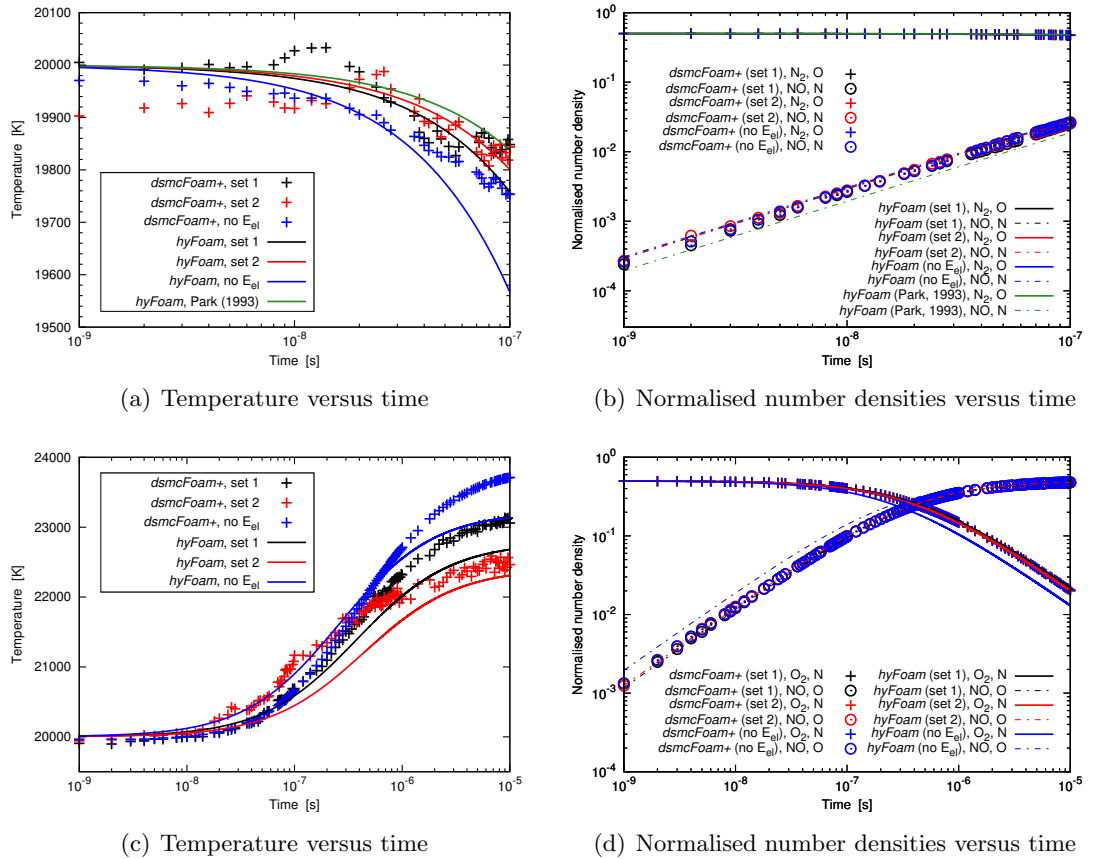
Figure 4.18: Heat bath with splitting enabled for forward and reverse exchange reactions 17 and 18

4.4.6   Charge exchange

Use of the Arrhenius parameters found in Section 4.2.6 is exemplified by considering the reaction $O_2 + NO^+ \longrightarrow O_2{}^+ + NO$. Both electronic set-ups are alike for species involved in this reaction which means that results are independent from the electronic set-up. Figure 4.19 demonstrates the suitability of the DSMC-derived Arrhenius coefficients in matching the *dsmcFoam+* solution for a heat bath case with particle splitting. Conversely, choosing Park's rate in the CFD code produces a solution that is off by three orders of magnitude. It appears as if a similar equilibrium temperature will be recovered in Figure 4.19(a) though.

(a) Temperature versus time   (b) Normalised number densities versus time
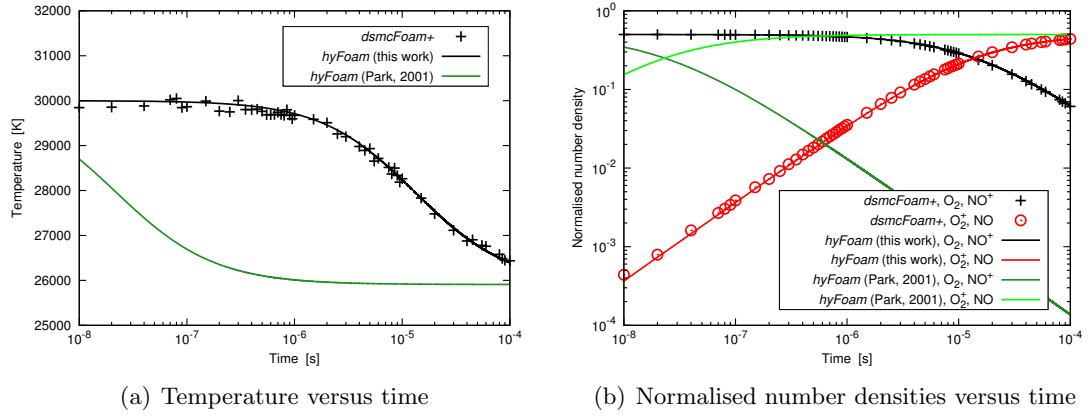
Figure 4.19: Heat bath with splitting enabled for reaction 31a: $O_2 + NO^+ \longrightarrow O_2{}^+ + NO$

4.5   Adiabatic heat baths for air

Adiabatic heat bath simulations are conducted for two initial temperatures equal to 20,000 K and 40,000 K. The initial gas mixture is air in proportions $0.8 \ N_2 + 0.2 \ O_2$ and a total of eleven species are considered. The time-step is set to 1×10^{-10} s. DSMC solutions presented hereafter are the ensemble average of three statically-independent computations. Because of the anomalous behaviour that has been detected for forward associative ionizations using the second electronic energy levels dataset, only the first electronic set will be considered. Results are shown in Figures 4.20 and 4.22 for the newly-derived rates and in Figures 4.21 and 4.23 for Park's 1993 rates [7]. At 20,000 K, the species fate is well described by the QK rates with regards to the DSMC solution,

while a delay in the formation of products is observed using Park's rates. At 40,000 K, the DSMC temperature profile is showing a peculiar increase after 10 ns that is not captured using *hyFoam*. The discrepancies between CFD and DSMC are larger than at 20,000 K and as already stated, an improvement could be achieved by tuning individually the electron impact reactions. The temperature is correctly recovered as the case approaches thermal and chemical near-equilibrium when using the QK rates. Thermo-chemical equilibrium is achieved quicker with Park's rates (but it should not be forgotten that the reaction dataset is different) and the equilibrium temperature is inconsistent with the one provided by *dsmcFoam+*. Species concentrations are also shown to match poorly. Therefore, there seems to be a benefit in using QK rates versus Park's rates for the heat bath simulations presented if a reasonable approximation of the *dsmcFoam+* solution wants to be met.
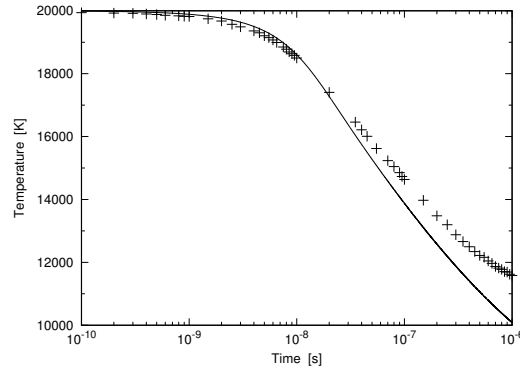
(a) Temperature vs. time
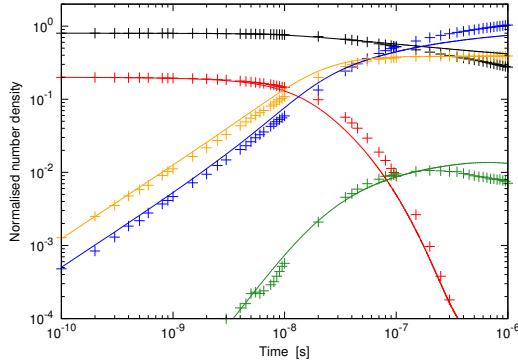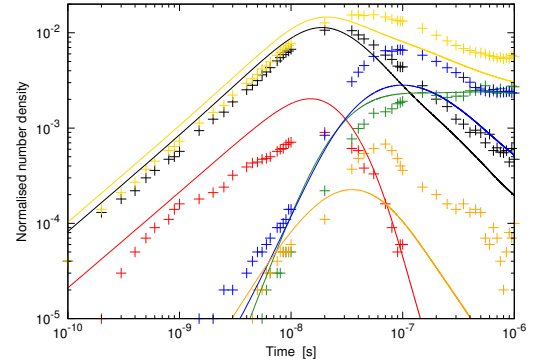
(b) Number densities vs. time (neutral species)   (c) Number densities vs. time (charged species)

Figure 4.20: Heat bath with splitting enabled for all reactions at 20,000 K (using set 1). CFD: lines, DSMC: symbols. N_2/N_2^+: black, N/N^+: dark blue, O_2/O_2^+: red, O/O^+: orange, NO/NO^+: green, e^-: yellow

(a) Temperature vs. time

(b) Number densities vs. time (neutral species)

(c) Number densities vs. time (charged species)
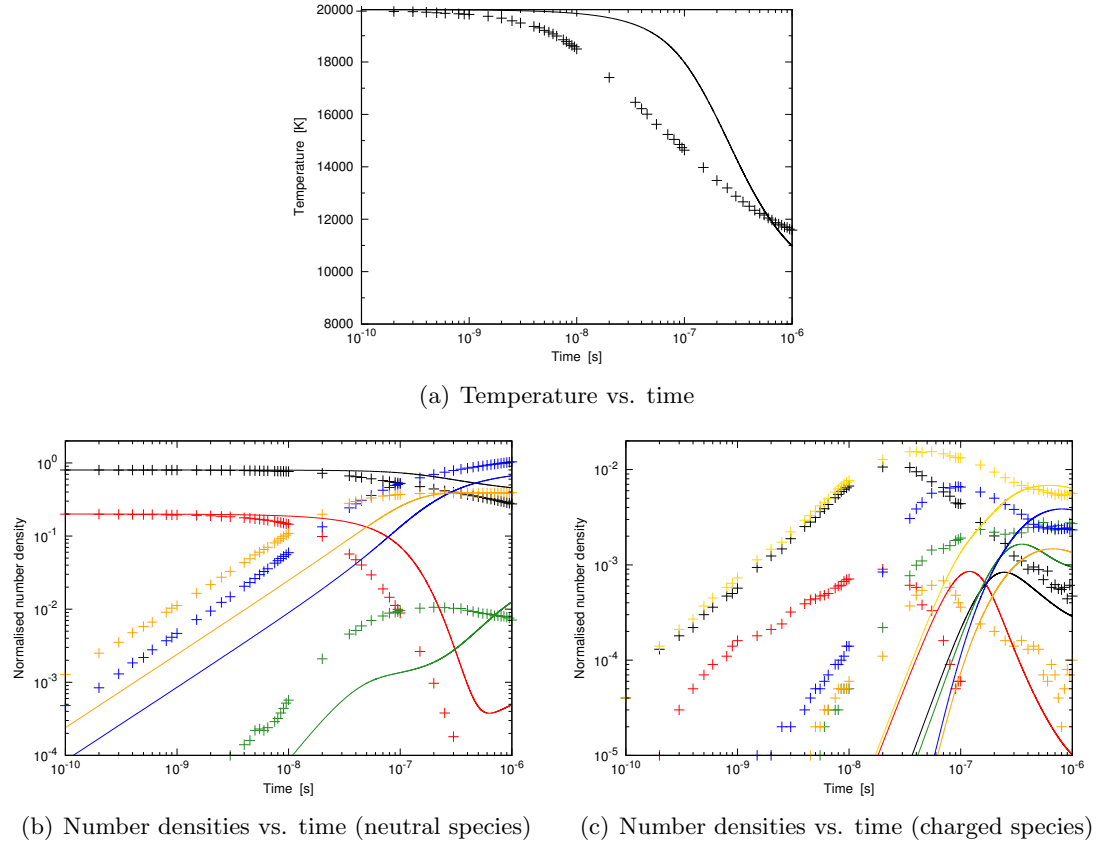
Figure 4.21: Heat bath with splitting enabled for all DPLR reactions at 20,000 K (using set 1). CFD: lines, DSMC: symbols. N_2/N_2^+: black, N/N^+: dark blue, O_2/O_2^+: red, O/O^+: orange, NO/NO^+: green, e^-: yellow

4.6   Future prospects

A list of possible improvements to the work contained in this Chapter is proposed below:

- Implement the fix for reactions involving similar species other than dissociation.

- Use third body interactions to reduce the number of reactions in the CFD dictionary and thus to save computational time. This can be done for dissociation and ionization reactions, fixing the temperature exponent, β, after its evaluation with a first reactant partner.

- Tune electron impact reactions individually

- Multi-vibrational capabilities are currently being implemented into *dsmcFoam+*. The extension of this work to reactions that are characteristic of Mars planetary
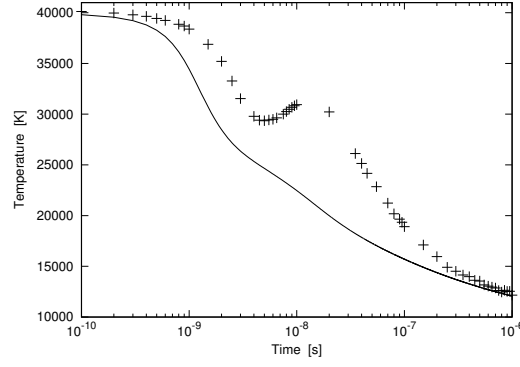
(a) Temperature vs. time
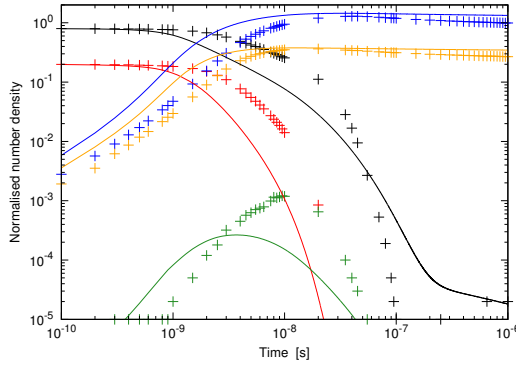
(b) Number densities vs. time (neutral species)
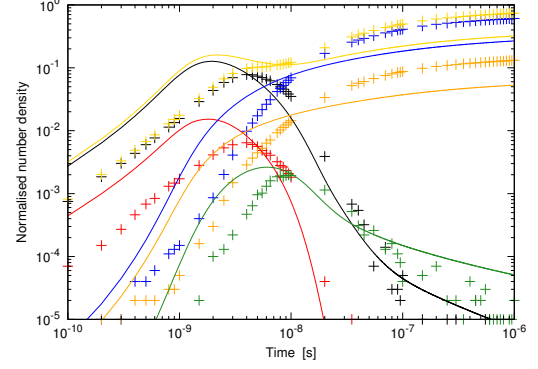
(c) Number densities vs. time (charged species)

Figure 4.22: Heat bath with splitting enabled for all reactions at 40,000 K (using set 1). CFD: lines, DSMC: symbols. N_2/N_2^+: black, N/N^+: dark blue, O_2/O_2^+: red, O/O^+: orange, NO/NO^+: green, e^-: yellow

entry conditions could be considered.

- Test the rate constants in situations of thermal non-equilibrium.

- Evaluate the influence of the new set of rates on a practical entry computation such as that of the 1636 s FireII spacecraft simulation presented by Hash *et al.* [131].
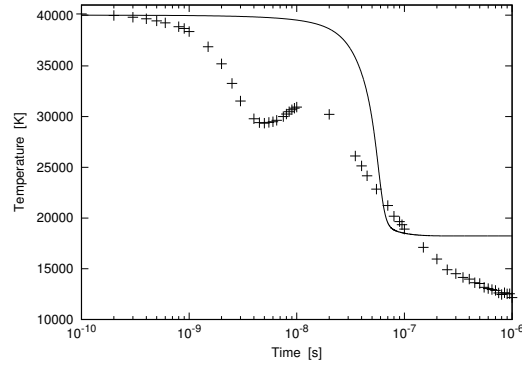
(a) Temperature vs. time
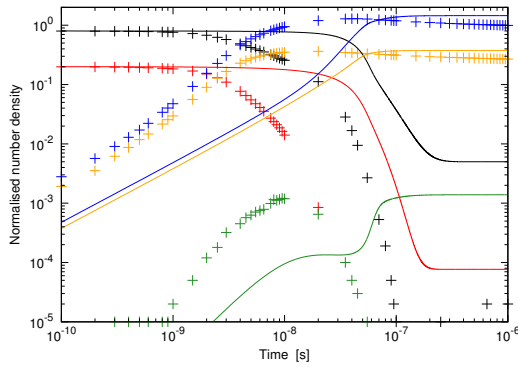
(b) Number densities vs. time (neutral species)
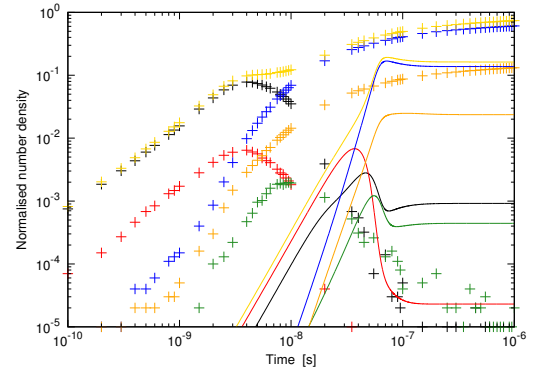
(c) Number densities vs. time (charged species)

Figure 4.23: Heat bath with splitting enabled for all DPLR reactions at 40,000 K (using set 1). CFD: lines, DSMC: symbols. N_2/N_2^+: black, N/N^+: dark blue, O_2/O_2^+: red, O/O^+: orange, NO/NO^+: green, e^-: yellow

Chapter 5

Conclusions

The open-source CFD software suite OpenFOAM has been enhanced with a new solver to compute hypersonic reacting flows in near-equilibrium conditions. The code, called *hy2Foam*, introduces a trans-rotational temperature and multiple vibro-electronic temperatures. It makes the use of state-of-the-art vibrational-translational and vibrational-vibrational energy transfers and offers the choice of whether to include the electronic energy into the calculations. Chemistry-vibration coupling is carried out using either the Park TTv model or the CVDV model.

The first objective of this work was conducted in Chapter 3 with the verification and the validation of the code. Demonstration of the successful implementation using a zero-dimensional benchmark case has been carried out by considering a single-species gas, a non-reacting mixture, and a reacting mixture initially set in a state of thermal non-equilibrium. In comparison with previously published heat bath data, *hy2Foam* has been shown to perform equally well. Further testing against results provided by the DSMC code *dsmcFoam* has highlighted again the discrepancies within CFD for flows that depart significantly from a Boltzmann distribution. The newly-coded two-temperature CFD solver has then been extended to simulate hypersonic multi-dimensional case scenarios. *hy2Foam* has shown to perform as well as an established Navier–Stokes CFD solver from the University of Michigan for a Mach 11 blunted cone, and to be in satisfactory agreement with the *dsmcFoam* code for a Mach 20 flow of a binary reacting mixture around a circular cylinder. For this latter case, the aerothermodynamic loads were better estimated using the novel *CVDV-QK* model combination

rather than the conventional Park combination, when compared to the *dsmcFoam* code. This result reaffirms the predictions found using zero-dimensional cases. It is considered that the cylinder case scenario presented in this paper provides a useful basis for other codes to compare against.

The *hy2Foam* [137] source code has been posted open-source on GitHub [138], a website that houses open-source projects for free and aims to foster collaboration, under the license GNU GPL-3.0. The beta version was released in December 2016, while the first release occurred in March 2017 and was tagged version 1.0. It has been complemented with tutorials, user manuals and the latest presentations. The supersonic open-source combusting flow solver *hyFoam* [137] that was developed and verified/validated in parallel to this work [139] can be found at the same address.

Chapter 4 utilised *dsmcFoam+* and *hyFoam* for the purpose of determining and assessing the rates provided by the DSMC quantum-kinetic framework. Those equilibrium rates have been derived therein and are reported in Appendix C. It was shown using adiabatic heat bath simulations that the electronic configuration has major consequences for specific reactions (*e.g.*, associative ionization) and can yield to an anomalous behaviour in turning an endothermic reaction into an exothermic one. Guidelines for improvements have been suggested.

Future work

Additional testing and verification of *hy2Foam* should be made and the open-source code COOLFluiD appears as an excellent candidate for code comparison. In particular, the further exploration of multi-dimensional case scenarios with the assessment of the code in an 11-species plasma configuration should be considered for future work. In conjunction with the findings of Chapter 4, a comparison could be undertaken between Park's rates [7] and the newly-derived QK rates.

This research opens a number of promising avenues for future investigations, some of which are proposed below

1. numerical schemes: state-of-the-art numerical schemes for the high-speed regime would need to be implemented to better capture near-wall effects.

2. wall catalicity: all simulations in this thesis assumed a non-catalytic wall in which the gas composition in the cell adjacent to the wall is imposed at the surface. To ensure proper accounting for gas-surface interaction, reaction kinetics should be modelled using new wall boundary conditions.

3. loose coupling with a radiation code / ablation code.

The discrepancies observed between the CFD and DSMC codes for Kn_{GLL} numbers outwith the continuum regime is a source of motivation for the development of a hypersonic hybrid hydrodynamic-molecular gas flow solver within OpenFOAM [66, 140]. This work provides the necessary CFD tools to meet this goal and is thus paving the way for open-source computations of planetary entry problems at intermediate altitudes.

References

[1] A. M. Feldick, M. F. Modest, D. A. Levin, P. Gnoffo, and C. O. Johnston. Examination of Coupled Continuum Fluid Dynamics and Radiation in Hypersonic Simulations. *AIAA Aerospace Sciences Meeting*, Paper 2009-0475, 2009.

[2] NASA's Orion Spacecraft official website. `https://www.nasa.gov/exploration/systems/orion/index.html`. Accessed: 4 September 2016.

[3] NASA Symposium. What is the Value of Space Exploration? NASA History Reference Collection, July 18-19, 1994.

[4] S. J. Dick and R. D. Launius (Eds.). *Societal impact of spaceflight.* The NASA history series, NASA SP-2007-4801, Washington, DC, 2007.

[5] R. Wuilbercq, F. Pescetelli, A. Mogavero, E. Minisci, and R. E. Brown. Robust multidisciplinary design and optimisation of a reusable launch vehicle. AIAA Paper 2014-2363, 2014.

[6] R. E. Brown. The future of air travel: Dinner in Sydney, London in time for 'The X-Factor'? The Washington Post, October 2014.

[7] C. Park. Review of Chemical-Kinetic Problems of Future NASA Missions. I-Earth Entries. *Journal of Thermophysics and Heat Transfer*, 7(3):385–398, 1993.

[8] T. E. Schwartzentruber, L. C. Scalabrin, and I. D. Boyd. A modular particle-continuum numerical method for hypersonic non-equilibrium gas flows. *J. Comput. Phys.*, 225(1): 1159–1174, 2007.

[9] J. D. Anderson. In *Hypersonic and High-Temperature Gas Dynamics*. AIAA, Reston, VA, 2 edition, 2006. ISBN : 9781563477805 (alk. paper).

[10] J. M. A. Longo, K. Hannemann, and V. Hannemann. The challenge of modeling high speed flows. In Proceedings of the 6th EUROSIM Congress on Modelling and Simulation. Ljubljana, Slovenia, 2007.

[11] A. Anna. *Numerical Modeling of Surface Chemistry Processes for Hypersonic Entry Environments*. PhD thesis, The University of Michigan, Ann Arbor, MI, US, 2013.

[12] G. A. Bird. *Molecular gas dynamics and the direct simulation of gas flows*. Clarendon, Oxford, 1994.

[13] G. Abbate, B. J. Thijsse, and C. R. Kleijn. *Computational Science – ICCS 2007: 7th International Conference, Beijing, China, May 27 - 30, 2007, Proceedings, Part I*, volume 225, chapter Coupled Navier-Stokes/DSMC Method for Transient and Steady-State Gas Flows, pages 842–849. Springer Berlin Heidelberg, Berlin, Heidelberg, 2007. ISBN 978-3-540-72584-8.

[14] C. Park. *Nonequilibrium Hypersonic Aerothermodynamics*. Wiley International, New York, 1990.

[15] G. V. Candler and I. Nompelis. Computational Fluid Dynamics for Atmospheric Entry. RTO-AVT-VKI Lecture Series 2009-AVT-162, 2009.

[16] D. Petkow, M. Zaretskaya, A. Kling, and G. Herdrich. Progress in probabilistic modelling of atomic spontaneous emission processes in DSMC. pages 16–19. Proceedings of the 5th International Workshop on Radiation of High Temperature Gases in Atmospheric Entry, 2012.

[17] J. M. Burt and I. D. Boyd. A Hybrid Particle Approach for Continuum and Rarefied Flow Simulation. *Journal of Computational Physics*, 228(2):460–475, 2009.

[18] I. D. Boyd, G. Chen, and G. V. Candler. Predicting failure of the continuum fluid equations in transitional hypersonic flows. *Physics of Fluids*, 7(1):210–219, 1995.

[19] M. Darbandi and E. Roohi. Applying a hybrid dsmc/navier-stokes frame to explore the effect of splitter catalyst plates in micro/nanopropulsion systems. *Sensors and Actuators A*, 189:409–419, 2013.

[20] R. Roveda, D. B. Goldstein, and P. L. Varghese. Hybrid euler/particle approach for continuum/rarefied flows. *J. Spacecraft Rockets*, 35(3):258–265, 1998.

[21] T. E. Schwartzentruber, L. C. Scalabrin, and I. D. Boyd. Hybrid particle-continuum simulations of nonequilibrium hypersonic blunt-body flowfields. *Journal of Thermodynamics and Heat Transfer*, 22(1):29–37, 2008.

[22] T. E. Schwartzentruber and I. D. Boyd. A hybrid particle-continuum method applied to shock waves. *J. Comput. Phys.*, 215(2):402–416, 2006.

[23] I. D. Boyd and T. R. Deschenes. Hybrid Particle-Continuum Numerical Methods for Aerospace Applications. Paper 6, 2011. 1–36 pp.

[24] W.-L. Wang and I. Boyd. Hybrid dsmc-cfd simulations of hypersonic flow over sharp and blunted bodies. AIAA, June 2003.

[25] I. D. Boyd. Predicting Breakdown of the Continuum Equations under Rarefied Flow Conditions. *AIP Conference Proceedings*, 2003.

[26] D. B. Hash and H. A. Hassan. A decoupled DSMC/NavierStokes analysis of a transitional flow experiment. *AIAA Proceedings, Paper presented at the 34th AIAA Aerospace Sciences Meeting and Exhibit, Reno, NV*, 96-0353, 1996.

[27] N. G. Hadjiconstantinou, A. L. Garcia, M. Z. Bazant, and G. He. Statistical error in particle simulations of hydrodynamic phenomena. *Journal of Computational Physics*, 187(1):274–297, 2003.

[28] F. M. Cheatwood and P. A. Gnoffo. User's manual for the langley aerothermodynamic upwind algorithm (laura). Technical report, 1996.

[29] G. V. Candler, M. J. Write, and J. D. McDonald. Data-Parallel Lower-Upper Relaxation Method for Reacting Flows. *AIAA Journal*, 32(12):2380–2386, 1994.

[30] L. C. Scalabrin and I. D. Boyd. Development of an Unstructured Navier-Stokes Solver For Hypersonic Nonequilibrium Aerothermodynamics. AIAA, 2005.

[31] L. C. Scalabrin and I. D. Boyd. Numerical Simulation of Weakly Ionized Hypersonic Flow for Reentry Configurations. AIAA, 2006.

[32] I. Nompelis, T. W. Drayna, and G. V. Candler. Development of a Hybrid Unstructured Implicit Solver for the Simulation of Reacting Flows Over Complex Geometries. AIAA, 2004.

[33] I. Nompelis, T. W. Drayna, and G. V. Candler. A Parallel Unstructured Implicit Solver for Hypersonic Reacting Flow Simulation. AIAA, 2005.

[34] A. Mack and V. Hannemann. Validation of the Unstructured DLR TAU-Code for Hypersonic Flows. AIAA 2002-3111, 2002.

[35] G. A. Bird. The DS2V Program User's Guide Ver. 3.2, G.A.B. Consulting Pty Ltd, 2005.

[36] G. A. Bird. The DS3V Program User's Guide Ver. 2.5, G.A.B. Consulting Pty Ltd, 2006.

[37] S. Dietrich and I. D. Boyd. Scalar and Parallel Optimized Implementation of the Direct Simulation Monte Carlo Method. *Journal of Computational Physics*, 126(2):328–342, 1996.

[38] G. J. LeBeau and F. E. Lumpkin. Application Highlights of the DSMC Analysis Code (DAC) Software for Simulating Rarefied Flows. *Computer Methods in Applied Mechanics and Engineering*, 191(6-7):595–609, 2001.

[39] M. S. Ivanov et al. SMILE System for 2D/3D DSMC Computations, July 2006.

[40] ANSYS, Inc. ANSYS FLUENT Academic Research, Release 15.0. `http://www.ansys.com`.

[41] O. Peroomian, S. Chakravarthy, S. Palaniswamy, and U. Goldberg. Convergence acceleration for unified-grid formulation using preconditioned implicit relaxation. *AIAA*, Paper 98-0116, Reno, NV, Jan. 1998.

[42] B. A. Maicke and J. Majdalani. Evaluation of CFD Codes for Hypersonic Flow Modeling. *46th AIAA/ASME/SAE/ASEE Joint Propulsion Conference & Exhibit*, Paper 2010-7184, 2010.

[43] OpenFOAM official website. http://www.openfoam.com/, accessed: 4 September 2016.

[44] T. J. Scanlon, C. White, M. K. Borg, R. C. Palharini, E. Farbar, I. D. Boyd, J. M. Reese, and R. E. Brown. Open source Direct Simulation Monte Carlo (DSMC) chemistry modelling for hypersonic flows. *AIAA Journal*, 53(6):1670–1680, 2015.

[45] R. C. Palharini. *Atmospheric Reentry Modelling Using an Open-Source DSMC Code.* PhD thesis, University of Strathclyde, Glasgow, 2014.

[46] C. Borgnakke and P. S. Larsen. Statistical collision model for simulating polyatomic gas with restricted energy exchange. *Rarefied Gas Dynamics*, 1, 1974. Paper A7, DFVLR Press, Porz-Wahn, Germany.

[47] G. A. Bird. *The DSMC Method.* Sydney, 2 edition, 2013. ISBN : 9781492112907.

[48] Github repository of the *dsmcFoamPlus* solver. `https://github.com/MicroNanoFlows/OpenFOAM-2.4.0-MNF/tree/devel-craig`, 2016.

[49] C. White, R. C. Palharini, V. Casseau, and T. J. Scanlon. Chemical Reactions Involving Charged Species in an Open Source DSMC Solver. *Considered for publication*, 2017.

[50] R. C. Palharini and J. L. F. Azevedo. Assessment of Rarefaction Effects on the SARA Capsule. In *Proceedings of the 30th Rarefied Gas Dynamics Conference*. AIP, Victoria BC, Canada, July 10-15, 2016.

[51] T. J. Scanlon, C. White, and R. C. Palharini. Simulation of Satellite Re-entry Using the Direct Simulation Monte Carlo (DSMC) Method. Paper presented at the Final Stardust Conference held at ESA ESTEC, Noordwijk, The Netherlands, 31st Oct. – 4th Nov. 2016.

[52] C. White et al. Numerical and Experimental Capabilities for Studying Rocket Plume-Regolith Interactions. In *Proceedings of the 30th Rarefied Gas Dynamics Conference*. AIP, Victoria BC, Canada, July 10-15, 2016.

[53] Home page for the DSMC code SPARTA. `http://sparta.sandia.gov/`, 2017.

[54] M. A. Gallis, J. R. Torczynski, S. J. Plimpton, D. J. Rader, and T. Koehler. Direct Simulation Monte Carlo: The Quest for Speed. In *Proceedings of the 29th Rarefied Gas Dynamics Conference*. AIP, Xi'an, China, July 2014.

[55] M. A. Gallis, T. P. Koehler, J. R. Torczynski, and S. J. Plimpton. Direct simulation Monte Carlo investigation of the Richtmyer-Meshkov instability. *Physics of Fluids*, 27: 084105, 2015.

[56] A. Klothakis and I. K. Nikolos. Modeling of Rarefied Hypersonic Flows using the Massively Parallel DSMC Kernel SPARTA. Paper presented at the 8th GRACM International Congress on Computational Mechanics, Volos, Greece, July 2015.

[57] Home page for the CFD code Eilmer3. `http://cfcfd.mechmining.uq.edu.au/eilmer3.html`, 2017.

[58] R.J. Gollan and P.A. Jacobs. About the formulation, verification and validation of the hypersonic flow solver Eilmer. *International Journal for Numerical Methods in Fluids*, 73 (1):19–57, 2013. ISSN 1097-0363.

[59] R. J. Gollan. *The Computational Modelling of High-Temperature Gas Effects with Application to Hypersonic Flows*. PhD thesis, The University of Queensland, Brisbane, QLD, Australia, 2008.

[60] List of Undergraduate Projects using Eilmer3 at the University of Queensland. `http://cfcfd.mechmining.uq.edu.au/undergraduate-projects.html`.

[61] A. Lani, N. Villedieu, K. Bensassi, L. Kapa, M. Panesi, and M. S. Yalim. "COOLFluiD": an open computational platform for multi-physics simulation. *AIAA*, Paper 2013-2589, San Diego, CA, Jun. 2013.

[62] Github repository of the COOLFluiD platform. `https://github.com/andrealani/COOLFluiD`, 2017.

[63] G. Degrez, A. Lani, M. Panesi, O. Chazot, and H. Deconinck. Modelling of high-enthalpy, high-Mach number flows. *Journal of Physics D: Applied Physics*, 42(19), 2013.

[64] ESI OpenCFD / Roger Almenar. Custodians of OpenFOAM: Past, present and future of OpenFOAM. Presented at the Fifth Symposium on OpenFOAM in Wind Energy (SOWE 2017): `http://windbench.net/system/files/roger_almenar_-_presentation.pdf`, April 2017.

[65] P. Jacobs and R. Gollan. Implementation of a Compressible-Flow Simulation Code in the D Programming Language. *Applied Mechanics and Materials*, 846:54–60, 2016.

[66] D. E. R. Espinoza, V. Casseau, T. J. Scanlon, and R. E. Brown. An Open Source Hybrid CFD-DSMC Solver for High-Speed Flows. *AIP Conference Proceedings*, 1786(1):050007, 2016.

[67] C. J. Greenshields, H. G. Weller, L. Gasparini, and J. M. Reese. Implementation of semi-discrete, non-staggered central schemes in a collocated, polyhedral, finite volume framework, for high-speed viscous flows. *International Journal For Numerical Methods In Fluids*, 63(1):1–21, 2010.

[68] A. Kurganov, S. Noelle, and G. Petrova. Semi-discrete central-upwind schemes for hypersonic conservation laws and Hamilton-Jacobi equations. *SIAM J. Sci. Comput.*, 23 (3):707–740, 2001.

[69] P. A. Jacobs, R. J. Gollan, D. F. Potter, D. E. Gildfind, T. N. Eichmann, B. T. O'Flaherty, and D. R. Buttsworth. CFD Tools for Design and Simulation of Transient Flows in Hypersonic Facilities. RTO-AVT-VKI Lecture Series 2010-AVT-186 - Aerothermodynamic Design, Review on Ground Testing and CFD, 2010.

[70] W. G. Vincenti and C. H. Kruger. *Introduction to Physical Gas Dynamics*. Krieger Publishing Company, Florida, 1965. ISBN 0882753096, 978-0882753096.

[71] F. G. Blottner, M. Johnson, and M. Ellis. Chemically reacting viscous flow program for multicomponent gas mixtures. Report no. sc-rr-70-754, Albuquerque, New Mexico, 1971.

[72] R. N. Gupta, J. M. Yos, and R. A. Thompson. A Review of Reaction Rates and Thermodynamic and Transport Properties for the 11-Species Air Model for Chemical and Thermal Nonequilbrium Calculations to 30000 K. NASA TM-101528, 1989.

[73] R. N. Gupta, J. M. Yos, R. A. Thompson, and K.-P. Lee. A Review of Reaction Rates and Thermodynamic and Transport Properties for an 11-Species Air Model for Chemical and Thermal Nonequilbrium Calculations to 30000 K. NASA RP-1232, 1990.

[74] G. E. Palmer and M. J. Wright. Comparison of Methods to Compute High-Temperature Gas Viscosity. *Journal of Thermophysics and Heat Transfer*, 17(2):232–239, 2003.

[75] C. R. Wilke. A Viscosity Equation for Gas Mixtures. *Journal of Chemical Physics*, 18 (4):517–519, 1950.

[76] B. F. Armaly and L. Sutton. Viscosity of Multicomponent Partially Ionized Gas Mixtures. AIAA Paper 80-1495, 1980.

[77] S. Chapman and T. G. Cowling. In *The Mathematical Theory of Non-uniform Gases*. Cambridge University Press, Cambridge, UK, 3rd edition, 1970.

[78] K. Sutton and P. A. Gnoffo. Multi-component Diffusion with Application to Computational Aerothermodynamics. AIAA Paper 98-2575, 1998.

[79] R. Gosse and G. Candler. Diffusion Flux Modeling: Application to Direct Entry Problems. AIAA Paper 2005-389, 2005.

[80] H. Alkandry, I. D. Boyd, and A. Martin. Comparaison of Models for Mixture Transport Properties for Numerical Simulations of Ablative Heat-Shields. AIAA Paper 2013-0303, 2013.

[81] K. A. Stephani. *Development of a Hybrid DSMC/CFD Method for Hypersonic Boundary Layer Flow over Discrete Surface Roughness*. PhD thesis, The University of Texas, Austin, TX, USA, May 2012.

[82] L. Landau and E. Teller. On the theory of sound dispersion. *Physikalische Zeitschrift der Sowjetunion*, 10(34), 1936.

[83] R. C. Millikan and D. R. White. Systematics of Vibrational Relaxation. *The Journal of Chemical Physics*, 39(12):3209–3213, 1963.

[84] R. N. Schwartz, Z. I. Slawsky, and K. F. Herzfeld. Calculation of Vibrational Relaxation Times in Gases. *The Journal of Chemical Physics*, 20(10):1591–1599, 1952.

[85] F. Thivet, M. Y. Perrin, and S. Candel. A unified nonequilibrium model for hypersonic flows. *Physics of Fluids*, 3(11):2799–2812, 1991.

[86] O. Knab, H.-H. Frühauf, and S. Jonas. Multiple Temperature Descriptions of Reaction Rate Constants with Regard to Consistent Chemical-Vibrational Coupling. AIAA Paper 92-2947, July 1992.

[87] O. Knab, H.-H. Frühauf, and E. W. Messerschmid. Theory and Validation of the Physically Consistent Coupled Vibration-Chemistry-Vibration Model. *Journal of Thermophysics and Heat Transfer*, 9(2):219–226, 1995. ISSN 0887-8722.

[88] G. V. Candler and R. W. MacCormack. Computation of weakly ionized hypersonic flows in thermochemical nonequilibrium. *Journal of Thermophysics and Heat Transfer*, 5(3): 266–273, 1991.

[89] P. A. Gnoffo, R. Gupta, and J. L. Shinn. Conservation equations and physical models for hypersonic air flows in thermal and chemical nonequilibrium. Tech. Report NASA-2867, 1989.

[90] R. Brun. *Introduction to Reactive Gas Dynamics*. Oxford University Press, 2009. ISBN 9780199552689. 429 pp.

[91] Leonardo Scalabrin. *Numerical Simulation of Weakly Ionized Hypersonic Flow over Reentry Capsules*. PhD thesis, The University of Michigan, 2007. 198 pp.

[92] P. V. Marrone and C. E. Treanor. Chemical relaxation with preferential dissociation from excited vibrational levels. *Physics of Fluids*, 6(9):1215–1221, 1963.

[93] T. D. Holman and I. Boyd. Effects of continuum breakdown on hypersonic aerothermodynamics for reacting flow. *Physics of Fluids*, 23(2), 2011.

[94] C. E. Treanor and P. V. Marrone. Effect of dissociation on the rate of vibrational relaxation. *Physics of Fluids*, 9(5):1022–1026, 1962.

[95] J. C. Maxwell. On stresses in Rarefied Gases Arising from Inequalities of Temperature. *Philosophical Transactions of the Royal Society of London*, 170:231–256, 1879.

[96] C. J. Greenshields and J. M. Reese. Rarefied hypersonic flow simulations using the Navier-Stokes equations with non-equilibrium boundary conditions. *Progress in Aerospace Sciences*, 52(1):80–87, 2012.

[97] M. von Smoluchowski. Ueber wärmeleitung in verdünnten Gasen. *Annalen der Physik und Chemie*, 64:101–130, 1898.

[98] T. J. Scanlon, R. C. Palharini, C. White, D. E. R. Espinoza, and V. Casseau. Simulations of rarefied and continuum hypersonic flow over re-entry objects. In *Paper presented at 8th European Symposium on Aerothermodynamics for Space Vehicles*. Lisbon, Portugal, 2015.

[99] J. B. Vos, A. Rizzi, D. Darracq, and E. H. Hirschel. Navier-Stokes solvers in European aircraft design. *Progress in Aerospace Sciences*, 38:601–697, 2002.

[100] M.-S. Liou. A Sequel to AUSM, Part II: AUSM$^+$-up for all speeds. *Journal of Computational Physics*, 214(1):137–170, 2006.

[101] Y. Wada and M.-S. Liou. An Accurate and Robust Flux Splitting Scheme for Shock and Contact Discontinuities. *SIAM J. Sci. Comput.*, 18(3):633–657, 1997.

[102] E. F. Toro, M. Spruce, and W. Speares. Restoration of the contact surface in the Harten–Lax–van Leer Riemann solver. *Shock Waves*, 4:25–34, 1994.

[103] Parallel computing in OpenFOAM. https://cfd.direct/openfoam/user-guide/running-applications-parallel/, accessed: 21 March 2017.

[104] D. E. R. Espinoza, T. J. Scanlon, and R. E. Brown. Validation of Tools to Accelerate High-Speed CFD Simulations Using OpenFOAM. In *Proceedings of the 20th AIAA International Space Planes and Hypersonic Systems and Technologies Conference*. AIAA Paper 2015-3566, 2015.

[105] A. L. Garcia. Direct simulation monte carlo: Novel applications and new extensions. 1997.

[106] W. Wagner. A convergence proof for Bird's direct simulation Monte Carlo method for the Boltzmann equation. *Journal of Statistical Physics*, 66(3):1011–1044, 1992.

[107] G. A. Bird. Perception of Numerical Methods in Rarefied Gasdynamics. *Progress in Astronautics and Aeronautics*, 118:221–226, 1989.

[108] G. A. Bird. Monte Carlo simulation in an engineering context. *Progress in Astronautics and Aeronautics*, 74(1):239–255, 1981.

[109] B. L. Haas, J. D. McDonald, and L. Dagum. Models of thermal relaxation mechanics for particle simulations. *Journal of Computational Physics*, 107(2):348–358, 1993.

[110] F. Bergemann and I. D. Boyd. New discrete vibrational energy model for the direct simulation Monte Carlo. *Progress in Astronautics and Aeronautics*, 158:174–183, 1994.

[111] G. A. Bird. Simulation of multi-dimensional and chemically reacting flows (past Space Shuttle orbiter). 11th International Symposium on Rarefied Gas Dynamics, pages 336–388, 1979.

[112] G. A. Bird. A comparison of collision energy-based and temperature-based procedures in DSMC. In T. Abe, editor, *Proceedings of the 26th Rarefied Gas Dynamics Conference*, volume 1084, pages 245–250. AIP, 2009.

[113] M. A. Gallis, R. B. Bond, and J. R. Torczynski. A kinetic-theory approach for computing chemical-reaction rates in upper-atmosphere hypersonic flows. *The Journal of Chemical Physics*, 131(12):124311, 2009.

[114] G. A. Bird. The Q-K model for gas-phase chemical reaction rates. *Physics of Fluids*, 23 (10):106101, 2011.

[115] D. S. Liechty and M. J. Lewis. Extension of the quantum-kinetic model to lunar and Mars return physics. *Physics of Fluids*, 26(2):027106, 2014.

[116] S. Dietrich and I. D. Boyd. Scalar and Parallel Optimized Implementation of the Direct Simulation Monte Carlo Method. *Journal of Computational Physics*, 126(2):328–342, 1996.

[117] B. L. Haas and J. D. McDonald. Validation of chemistry models employed in a particle simulation method. *Journal of Thermophysics and Heat Transfer*, 7(1):42–48, 1993.

[118] I. D. Boyd and E. Josyula. State Resolved Vibrational Relaxation Modeling for Strongly Nonequilibrium Flows. *Physics of Fluids*, 23(5), 2011.

[119] I. D. Boyd. Analysis of vibration-dissociation-recombination processes behind strong shock waves of nitrogen. *Physics of Fluids*, 4(178), 1992.

[120] T. E. Magin, M. Panesi, A. Bourdon, R. Jaffe, and D. Schwenke. Internal energy excitation and dissociation of molecular nitrogen in a compressing flow. Annual Research Briefs 2009, Center for Turbulence Research, 2009. 59–70 pp.

[121] ARCHIE-WeSt High Performance Computer. `https://www.archie-west.ac.uk/`, 2016.

[122] M. S. Holden. Experimental database from cubrc studies in hypersonic laminar and turbulent interacting flows including flowfield chemistry. Rto code validation of dsmc and navier-stokes code validation studies cubrc report, June 2000.

[123] C. Geuzaine and J.-F. Remacle. Gmsh: a three-dimensional finite element mesh generator with built-in pre- and post-processing facilities. *International Journal for Numerical Methods in Engineering*, 79(11):1309–1331, 2009.

[124] J. Ahrens, B. Geveci, and C. Law. *ParaView: An End-User Tool for Large Data Visualization*. Clarendon, Elsevier, 2005. ISBN 978-0123875822.

[125] Thomas Williams, Colin Kelley, and many others. Gnuplot 5.0: an interactive plotting program. `http://gnuplot.sourceforge.net/`, January 2015.

[126] ANSYS, Inc. ANSYS ICEM CFD Academic Research, Release 15.0. `http://www.ansys.com`.

[127] C. Park, R. L. Jaffe, and H. Partridge. Chemical-Kinetic Parameters of Hyperbolic Earth Entry. *Journal of Thermophysics and Heat Transfer*, 15(1):76–90, 2001.

[128] I. Wysong, S. Gimelshein, N. Gimelshein, W. McKeon, and F. Esposito. Reaction cross sections for two direct simulation Monte Carlo models: Accuracy and sensitivity analysis. *Physics of Fluids*, 24(4):042002, 2012.

[129] D. S. Liechty. *Extension of a Kinetic Approach to Chemical Reactions to Electronic Energy Levels and Reactions Involving Charged Species with Application to DSMC Simulations*. PhD thesis, University of Maryland, College Park, MD, USA, 2013.

[130] L. V. Gurvich, I. V. Veyts, and C. B. Alcock. *Thermodynamic Properties of Individual Substances vol 1*. Hemisphere Publishing Corp., New York, NY, USA, 1989.

[131] D. Hash et al. FIRE II Calculations for Hypersonic Nonequilibrium Aerothermodynamics Code Verification: DPLR, LAURA, US3D, and LeMANS. AIAA, 2007.

[132] C. O. Johnston. *Nonequilibrium Shock-Layer Radiative Heating for Earth and Titan Entry*. PhD thesis, Virginia Polytechnic Institute and State University, Blacksburg, VA, USA, 2007.

[133] See supplementary material at `http://dx.doi.org/10.1063/1.3650424`, 2011.

[134] J. R. Downey Jr. Calculation of Thermodynamic Properties of Ideal Gases at High Temperatures: Monatomic Gases. AFOSR–TR-78-0960, DOW Chemical Company, Thermal Research Laboratory, Midland, MI, USA, 1978.

[135] S. Gordon and B. J. McBride. Thernodynamic Data to 20 000 K for Monatomic Gases. TP–1999-208523, National Aeronautics and Space Administration (NASA), Glenn Research Center, Cleveland, OH, USA, 1999.

[136] M. I. Hoffert and H. Lien. Quasi-One-Dimensional, Nonequilibrium Gas Dynamics of Partially Ionized Two-Temperature Argon. *Physics of Fluids*, 10(8):1769–1777, 1967.

[137] Github repository of the *hy2Foam* solver. `https://github.com/vincentcasseau/hyStrath/`, 2017. Version 1.0, commit 8b44e95.

[138] Github webpage. `https://github.com/`, 2017.

[139] J.-J. Hoste, V. Casseau, M. Fossati, I. J. Taylor, and R. J. Gollan. Numerical Modeling and Simulation of Supersonic Flows in Propulsion Systems by Open-Source Solvers. *AIAA*, Paper 2017-2411, 2017.

[140] V. Casseau, D. E. R. Espinoza, and T. J. Scanlon. Open-source High-fidelity Solvers Dedicated to Re-entry Analysis and Design for Demise. 31st Oct. – 3rd Nov. 2016. Paper presented at the Final Stardust Conference, ESA-ESTEC, Noordwijk, the Netherlands.

Appendices

A Species thermochemical properties

Table A1 lists the species thermochemical data used in the *hy2Foam* solver. For each species s is given the molecular weight, $\mathcal{M}_s$, the enthalpy of formation at 298 K, h_s°, the characteristic vibrational temperature, $\theta_{v,s}$, the dissociation potential, D_s, the diameter of the particle, $d_{\text{ref},s}$, the temperature coefficient of viscosity, ω_s, and the three coefficients $A_{B,s}$, $B_{B,s}$, and $C_{B,s}$ used to calculate the shear viscosity according to Blottner's formula in given Eq. 2.15.

Table A1: Species thermochemical data used in *hy2Foam*

Species s	$\mathcal{M}_s$ [g m^{-3}]	h_s° [J kg^{-1}]	$\theta_{v,s}$ [K]	D_s [J kg^{-1}]
N$_2$	28.0134	0	3,371	3.36×10^7
O$_2$	31.9988	0	2,256	1.54×10^7
NO	30.0061	3.04×10^6	2,719	2.09×10^7
N	14.0067	3.37×10^7	-	-
O	15.9994	1.56×10^7	-	-
N$_2{}^+$	28.0128514	5.43×10^7	3,371	3.0×10^7
O$_2{}^+$	31.9982514	3.66×10^7	2,256	3.66×10^7
NO$^+$	30.0055514	3.28×10^7	2,719	2.09×10^7
N$^+$	14.0061514	1.34×10^8	-	-
O$^+$	15.9988514	9.77×10^7	-	-
e$^-$	5.4858×10^{-4}	-	-	-

Cont.

Species s	$d_{\mathrm{ref},s}$ $[10^{-10}$ m$]$	ω_s	$A_{B,s}$	$B_{B,s}$	$C_{B,s}$
N_2	4.17	0.74	0.0268	0.318	-11.3
O_2	4.07	0.77	0.0449	-0.0826	-9.2
NO	4.2	0.79	0.0436	-0.0336	-9.58
N	3.0	0.8	0.0116	0.603	-12.4
O	3.0	0.8	0.0203	0.429	-11.6
N_2^+	4.17	0.74	0.0268	0.318	-11.3
O_2^+	4.07	0.77	0.0449	-0.0826	-9.2
NO^+	4.2	0.79	0.302	-3.504	-3.74
N^+	3.0	0.8	0.0116	0.603	-12.4
O^+	3.0	0.8	0.0203	0.429	-11.6
e^-	5.6×10^{-5}	0.7	0	0	-12.0

B   Species electronic data

Table B1 gives information about the number of electronic levels to consider for all particles to be found in an eleven-species air. Each level i is associated with its respective degeneracy degree, g_i, and characteristic temperature, $\theta_{el,i}$. The horizontal dash line for N and O species indicates the maximum number of electronic levels of the first electronic set-up (set 1) that is typically used in CFD calculations, and all levels after this line are additional levels (set 2) considered in the *dsmcFoam* code as of April 2017. The influence of these two electronic set-ups have been studied in Chapter 4.

Table B1: Species electronic data

Level i	g_i	$\theta_{el,i}$ [K]
N_2		
ground	1	0
1	3	7.223157×10^4
2	6	8.577863×10^4
3	6	8.605027×10^4
4	3	9.535119×10^4
5	1	9.805636×10^4
6	2	9.968268×10^4
7	2	1.048976×10^5
8	5	1.116490×10^5
9	1	1.225836×10^5
10	6	1.248857×10^5
11	6	1.282476×10^5
12	10	1.338061×10^5
13	6	1.404296×10^5
14	6	1.504959×10^5
O_2		
ground	3	0
1	2	1.139156×10^4
2	1	1.898474×10^4
3	1	4.755974×10^4
4	6	4.991242×10^4
5	3	5.092269×10^4
6	3	7.189863×10^4

Cont.

Level i	g_i	$\theta_{el,i}$ [K]
NO		
ground	4	0
1	8	5.467346×10^4
2	2	6.317140×10^4
3	4	6.599450×10^4
4	4	6.906121×10^4
5	4	7.049998×10^4
6	4	7.491055×10^4
7	2	7.628875×10^4
8	4	8.676189×10^4
9	2	8.714431×10^4
10	4	8.886077×10^4
11	4	8.981756×10^4
12	2	8.988446×10^4
13	2	9.042702×10^4
14	2	9.064284×10^4
15	4	9.111763×10^4
N		
ground	4	0
1	10	2.766470×10^4
2	6	4.149309×10^4
3	12	1.199002×10^5
4	6	1.240142×10^5
5	12	1.268027×10^5
6	2	1.346396×10^5
7	20	1.364503×10^5
8	12	1.374209×10^5
9	4	1.392027×10^5
10	10	1.393186×10^5
11	6	1.407020×10^5
12	10	1.433964×10^5
13	12	1.491907×10^5
14	6	1.499150×10^5
15	6	1.505379×10^5
16	28	1.506683×10^5
17	14	1.508566×10^5
18	12	1.508602×10^5
19	20	1.510811×10^5
20	10	1.512622×10^5
21	2	1.531961×10^5
22	20	1.536959×10^5
23	12	1.539711×10^5
24	10	1.542753×10^5
25	4	1.545867×10^5

Cont.

Level i	g_i	$\theta_{el,i}$ [K]
N		
26	6	1.548330×10^5
27	90	1.587080×10^5
28	126	1.589543×10^5
29	450	1.620108×10^5
30	648	1.644372×10^5
31	822	1.656033×10^5
32	1152	1.663566×10^5
33	1458	1.668781×10^5
34	1800	1.672402×10^5
O		
ground	9	0
1	5	2.283029×10^4
2	1	4.861993×10^4
3	5	1.06472×10^5
4	3	1.10817×10^5
5	15	1.24579×10^5
6	9	1.27476×10^5
7	5	1.37616×10^5
8	3	1.38341×10^5
9	25	1.40514×10^5
10	15	1.40876×10^5
11	15	1.42687×10^5
12	9	1.43411×10^5
13	15	1.45584×10^5
14	5	1.47032×10^5
15	3	1.47394×10^5
16	5	1.47757×10^5
17	25	1.48010×10^5
18	15	1.48264×10^5
19	35	1.48481×10^5
20	21	1.48843×10^5
21	15	1.49205×10^5
22	9	1.49567×10^5
23	25	1.51378×10^5
24	15	1.51559×10^5
25	35	1.51740×10^5
26	21	1.51921×10^5
27	288	1.53551×10^5
28	392	1.55000×10^5
29	512	1.55724×10^5
30	648	1.56086×10^5
31	800	1.56448×10^5

Cont.

Level i	g_i	$\theta_{el,i}$ [K]
N_2^+
ground	2	0
1	4	1.318997×10^4
2	2	3.663323×10^4
3	4	3.668876×10^4
4	8	5.985305×10^4
5	8	6.618366×10^4
6	4	7.598992×10^4
7	4	7.625509×10^4
8	4	8.201019×10^4
9	4	8.416835×10^4
10	8	8.632651×10^4
11	8	8.920406×10^4
12	4	9.208161×10^4
13	4	9.222549×10^4
14	2	9.293768×10^4
15	2	9.639794×10^4
16	4	1.035918×10^5
O_2^+
ground	4	0
1	8	4.735441×10^4
2	4	5.837399×10^4
3	6	5.841427×10^4
4	4	6.229897×10^4
5	2	6.733468×10^4
6	4	7.121937×10^4
7	4	7.654284×10^4
8	4	8.819692×10^4
9	4	8.891631×10^4
10	8	9.423978×10^4
11	4	9.495916×10^4
12	2	9.592027×10^4
13	2	9.985100×10^4
14	4	1.035918×10^5

Cont.

Level i	g_i	$\theta_{el,i}$ [K]
NO$^+$		
ground	1	0
1	3	7.508968×10^4
2	6	8.525462×10^4
3	6	8.903576×10^4
4	3	9.746983×10^4
5	1	1.000553×10^5
6	2	1.028034×10^5
7	2	1.057139×10^5
N$^+$, set 1		
ground	1	0
1	3	7.006835×10^1
2	5	1.881918×10^2
3	5	2.203657×10^4
4	1	4.703183×10^4
5	5	6.731252×10^4
6	15	1.327191×10^5
N$^+$, set 2		
ground	1	0
1	3	7.006835×10^1
2	5	1.881918×10^2
3	5	2.203657×10^4
4	1	4.703183×10^4
5	15	1.327191×10^5
6	9	1.571435×10^5
7	5	2.074532×10^5
8	12	2.144644×10^5
O$^+$		
ground	4	0
1	10	3.858335×10^4
2	6	5.822349×10^4

C   QK rates

The Tables contained in this appendix list the QK Arrhenius coefficients, sorted by interaction types, that have been derived in Chapter 4 for the electronic set 1. Units of A and ϵ_a are given in m^3 molecule^{-1} s^{-1} and kg m^2 s^{-2}, respectively.

Table C1: DSMC-derived Arrhenius coefficients, molecule–molecule dissociation (endothermic)

No	Reaction	Temp. range	Arrhenius Law Constants		
			A	β	ϵ_a
1a	$N_2 + N_2 \rightarrow N + N + N_2$	-	2.19×10^{-09}	-1.21	1.567×10^{-18}
1b	$N_2 + N_2^+ \rightarrow N + N + N_2^+$	-	3.59×10^{-10}	-1.01	1.567×10^{-18}
1c	$N_2 + O_2 \rightarrow N + N + O_2$	-	5.53×10^{-10}	-1.06	1.567×10^{-18}
1d	$N_2 + O_2^+ \rightarrow N + N + O_2^+$	-	5.45×10^{-10}	-1.06	1.567×10^{-18}
1e	$N_2 + NO \rightarrow N + N + NO$	-	8.07×10^{-10}	-1.10	1.567×10^{-18}
1f	$N_2 + NO^+ \rightarrow N + N + NO^+$	-	6.84×10^{-10}	-1.08	1.567×10^{-18}
2a	$O_2 + O_2 \rightarrow O + O + O_2$	-	5.91×10^{-11}	-0.96	8.197×10^{-19}
2b	$O_2 + O_2^+ \rightarrow O + O + O_2^+$	-	2.95×10^{-11}	-0.86	8.197×10^{-19}
2c	$O_2 + N_2 \rightarrow O + O + N_2$	-	6.66×10^{-11}	-0.93	8.197×10^{-19}
2d	$O_2 + N_2^+ \rightarrow O + O + N_2^+$	-	3.73×10^{-11}	-0.87	8.197×10^{-19}
2e	$O_2 + NO \rightarrow O + O + NO$	-	3.45×10^{-11}	-0.88	8.197×10^{-19}
2f	$O_2 + NO^+ \rightarrow O + O + NO^+$	-	4.21×10^{-11}	-0.90	8.197×10^{-19}
3a	$NO + NO \rightarrow N + O + NO$	-	2.27×10^{-10}	-1.06	1.043×10^{-18}
3b	$NO + NO^+ \rightarrow N + O + NO^+$	-	1.62×10^{-10}	-1.00	1.043×10^{-18}
3c	$NO + N_2 \rightarrow N + O + N_2$	-	1.75×10^{-10}	-1.00	1.043×10^{-18}
3d	$NO + N_2^+ \rightarrow N + O + N_2^+$	-	1.70×10^{-10}	-0.99	1.043×10^{-18}
3e	$NO + O_2 \rightarrow N + O + O_2$	-	1.45×10^{-10}	-0.99	1.043×10^{-18}
3f	$NO + O_2^+ \rightarrow N + O + O_2^+$	-	1.65×10^{-10}	-1.00	1.043×10^{-18}

Table C2: DSMC-derived Arrhenius coefficients, molecule–atom dissociation (endothermic)

No	Reaction	Temp. range	Arrhenius Law Constants		
			A	β	ϵ_a
1g	$N_2 + N \rightarrow N + N + N$	-	6.69×10^{-10}	-1.09	1.567×10^{-18}
1h	$N_2 + N^+ \rightarrow N + N + N^+$	-	6.77×10^{-10}	-1.09	1.567×10^{-18}
1i	$N_2 + O \rightarrow N + N + O$	-	5.74×10^{-10}	-1.08	1.567×10^{-18}
1j	$N_2 + O^+ \rightarrow N + N + O^+$	-	4.12×10^{-10}	-1.05	1.567×10^{-18}
2g	$O_2 + N \rightarrow O + O + N$	-	2.28×10^{-11}	-0.85	8.197×10^{-19}
2h	$O_2 + N^+ \rightarrow O + O + N^+$	-	3.78×10^{-11}	-0.90	8.197×10^{-19}
2i	$O_2 + O \rightarrow O + O + O$	-	3.08×10^{-11}	-0.88	8.197×10^{-19}
2j	$O_2 + O^+ \rightarrow O + O + O^+$	-	4.16×10^{-11}	-0.91	8.197×10^{-19}
3g	$NO + N \rightarrow N + O + N$	-	1.29×10^{-10}	-0.99	1.043×10^{-18}
3h	$NO + N^+ \rightarrow N + O + N^+$	-	1.40×10^{-10}	-1.00	1.043×10^{-18}
3i	$NO + O \rightarrow N + O + O$	-	1.39×10^{-10}	-1.00	1.043×10^{-18}
3j	$NO + O^+ \rightarrow N + O + O^+$	-	1.34×10^{-10}	-1.00	1.043×10^{-18}

Table C3: DSMC-derived Arrhenius coefficients, electron impact dissociation (endothermic)

No	Reaction	Temp. range	Arrhenius Law Constants		
			A	β	ϵ_a
4	$N_2 + e^- \rightarrow N + N + e^-$	-	3.22×10^{-08}	-1.03	1.567×10^{-18}
5	$O_2 + e^- \rightarrow O + O + e^-$	-	2.78×10^{-09}	-0.88	8.215×10^{-19}
6	$NO + e^- \rightarrow N + O + e^-$	-	7.71×10^{-09}	-0.95	1.042×10^{-18}

Table C4: DSMC-derived Arrhenius coefficients, molecule–molecule ionization (endothermic)

No	Reaction	Temp. range	Arrhenius Law Constants		
			A	β	ϵ_a
5a	$N_2 + N_2 \rightarrow N_2^+ + e^- + N_2$	-	1.01×10^{-05}	-1.89	2.496×10^{-18}
5b	$N_2 + N_2^+ \rightarrow N_2^+ + e^- + N_2^+$	-	2.27×10^{-05}	-1.91	2.496×10^{-18}
5c	$N_2 + O_2 \rightarrow N_2^+ + e^- + O_2$	-	2.08×10^{-05}	-1.91	2.496×10^{-18}
5d	$N_2 + O_2^+ \rightarrow N_2^+ + e^- + O_2^+$	-	2.31×10^{-05}	-1.92	2.496×10^{-18}
5e	$N_2 + NO \rightarrow N_2^+ + e^- + NO$	-	2.02×10^{-05}	-1.91	2.496×10^{-18}
5f	$N_2 + NO^+ \rightarrow N_2^+ + e^- + NO^+$	-	2.42×10^{-05}	-1.93	2.496×10^{-18}
6a	$O_2 + O_2 \rightarrow O_2^+ + e^- + O_2$	-	1.25×10^{-10}	-1.01	1.934×10^{-18}
6b	$O_2 + O_2^+ \rightarrow O_2^+ + e^- + O_2^+$	-	2.80×10^{-10}	-1.02	1.934×10^{-18}
6c	$O_2 + N_2 \rightarrow O_2^+ + e^- + N_2$	-	2.12×10^{-10}	-0.98	1.934×10^{-18}
6d	$O_2 + N_2^+ \rightarrow O_2^+ + e^- + N_2^+$	-	1.95×10^{-10}	-0.97	1.934×10^{-18}
6e	$O_2 + NO \rightarrow O_2^+ + e^- + NO$	-	2.43×10^{-10}	-1.00	1.934×10^{-18}
6f	$O_2 + NO^+ \rightarrow O_2^+ + e^- + NO^+$	-	3.21×10^{-10}	-1.03	1.934×10^{-18}
7a	$NO + NO \rightarrow NO^+ + e^- + NO$	-	2.20×10^{-09}	-1.25	1.484×10^{-18}
7b	$NO + NO^+ \rightarrow NO^+ + e^- + NO^+$	-	5.26×10^{-09}	-1.27	1.484×10^{-18}
7c	$NO + O_2 \rightarrow NO^+ + e^- + O_2$	-	4.15×10^{-09}	-1.24	1.484×10^{-18}
7d	$NO + O_2^+ \rightarrow NO^+ + e^- + O_2^+$	-	4.44×10^{-09}	-1.25	1.484×10^{-18}
7e	$NO + N_2 \rightarrow NO^+ + e^- + N_2$	-	4.42×10^{-09}	-1.24	1.484×10^{-18}
7f	$NO + N_2^+ \rightarrow NO^+ + e^- + N_2^+$	-	5.51×10^{-09}	-1.26	1.484×10^{-18}

Table C5: DSMC-derived Arrhenius coefficients, molecule–atom ionization (endothermic)

No	Reaction	Temp. range	Arrhenius Law Constants		
			A	β	ϵ_a
5g	$N_2 + N \rightarrow N_2^+ + e^- + N$	-	1.31×10^{-05}	-1.88	2.496×10^{-18}
5h	$N_2 + N^+ \rightarrow N_2^+ + e^- + N^+$	-	2.12×10^{-05}	-1.92	2.496×10^{-18}
5i	$N_2 + O \rightarrow N_2^+ + e^- + O$	-	1.53×10^{-05}	-1.90	2.496×10^{-18}
5j	$N_2 + O^+ \rightarrow N_2^+ + e^- + O^+$	-	1.34×10^{-05}	-1.88	2.496×10^{-18}
6g	$O_2 + N \rightarrow O_2^+ + e^- + N$	-	2.69×10^{-10}	-1.03	1.934×10^{-18}
6h	$O_2 + N^+ \rightarrow O_2^+ + e^- + N^+$	-	1.51×10^{-10}	-0.97	1.934×10^{-18}
6i	$O_2 + O \rightarrow O_2^+ + e^- + O$	-	1.22×10^{-10}	-0.95	1.934×10^{-18}
6j	$O_2 + O^+ \rightarrow O_2^+ + e^- + O^+$	-	1.93×10^{-10}	-1.00	1.934×10^{-18}
7g	$NO + N \rightarrow NO^+ + e^- + N$	-	3.93×10^{-09}	-1.25	1.484×10^{-18}
7h	$NO + N^+ \rightarrow NO^+ + e^- + N^+$	-	4.31×10^{-09}	-1.26	1.484×10^{-18}
7i	$NO + O \rightarrow NO^+ + e^- + O$	-	4.72×10^{-09}	-1.27	1.484×10^{-18}
7j	$NO + O^+ \rightarrow NO^+ + e^- + O^+$	-	3.91×10^{-09}	-1.25	1.484×10^{-18}

Table C6: DSMC-derived Arrhenius coefficients, atom–atom ionization (endothermic)

No	Reaction	Temp. range	Arrhenius Law Constants		
			A	β	ϵ_a
8a	$N + N \rightarrow N^+ + e^- + N$	-	3.20×10^{-10}	-1.14	2.328×10^{-18}
8b	$N + O \rightarrow N^+ + e^- + O$	-	3.40×10^{-10}	-1.15	2.328×10^{-18}
9a	$O + O \rightarrow O^+ + e^- + O$	-	1.11×10^{-12}	-0.64	2.182×10^{-18}
9b	$O + N \rightarrow O^+ + e^- + N$	-	8.19×10^{-13}	-0.61	2.182×10^{-18}

Table C7: DSMC-derived Arrhenius coefficients, electron impact ionization (endothermic)

No	Reaction	Temp. range	Arrhenius Law Constants		
			A	β	ϵ_a
10	$N_2 + e^- \rightarrow N_2^+ + e^- + e^-$	-	1.05×10^{-03}	-1.87	2.496×10^{-18}
11	$O_2 + e^- \rightarrow O_2^+ + e^- + e^-$	-	2.62×10^{-08}	-1.03	1.934×10^{-18}
12	$NO + e^- \rightarrow NO^+ + e^- + e^-$	-	4.29×10^{-07}	-1.27	1.484×10^{-18}
13	$N + e^- \rightarrow N^+ + e^- + e^-$	-	6.93×10^{-10}	-0.73	2.328×10^{-18}
14	$O + e^- \rightarrow O^+ + e^- + e^-$	-	1.84×10^{-13}	0.02	2.182×10^{-18}

Table C8: DSMC-derived Arrhenius coefficients, atom–molecule ionization (endothermic)

No	Reaction	Temp. range	Arrhenius Law Constants		
			A	β	ϵ_a
15a	$N + N_2 \rightarrow N^+ + e^- + N_2$	-	6.44×10^{-10}	-1.10	2.328×10^{-18}
15b	$N + O_2 \rightarrow N^+ + e^- + O_2$	-	7.70×10^{-11}	-0.91	2.328×10^{-18}
15c	$N + NO \rightarrow N^+ + e^- + NO$	-	1.63×10^{-10}	-0.98	2.328×10^{-18}
16a	$O + N_2 \rightarrow O^+ + e^- + N_2$	-	6.29×10^{-13}	-0.48	2.182×10^{-18}
16b	$O + O_2 \rightarrow O^+ + e^- + O_2$	-	2.45×10^{-12}	-0.62	2.182×10^{-18}
16c	$O + NO \rightarrow O^+ + e^- + NO$	-	7.83×10^{-12}	-0.74	2.182×10^{-18}

Table C9: DSMC-derived Arrhenius coefficients, atom–ion ionization (endothermic)

No	Reaction	Temp. range	Arrhenius Law Constants		
			A	β	ϵ_a
17a	$N + N^+ \to N^+ + e^- + N^+$	-	8.34×10^{-10}	-1.16	2.328×10^{-18}
17b	$N + O^+ \to N^+ + e^- + O^+$	-	1.74×10^{-10}	-1.01	2.328×10^{-18}
17c	$N + O_2^+ \to N^+ + e^- + O_2^+$	-	1.85×10^{-10}	-0.99	2.328×10^{-18}
17d	$N + N_2^+ \to N^+ + e^- + N_2^+$	-	4.83×10^{-10}	-1.07	2.328×10^{-18}
17e	$N + NO^+ \to N^+ + e^- + NO^+$	-	2.47×10^{-10}	-1.02	2.328×10^{-18}
18a	$O + N^+ \to O^+ + e^- + N^+$	-	1.03×10^{-11}	-0.79	2.182×10^{-18}
18b	$O + O^+ \to O^+ + e^- + O^+$	-	3.88×10^{-12}	-0.69	2.182×10^{-18}
18c	$O + O_2^+ \to O^+ + e^- + O_2^+$	-	1.60×10^{-12}	-0.58	2.182×10^{-18}
18d	$O + N_2^+ \to O^+ + e^- + N_2^+$	-	1.61×10^{-12}	-0.57	2.182×10^{-18}
18e	$O + NO^+ \to O^+ + e^- + NO^+$	-	2.53×10^{-12}	-0.63	2.182×10^{-18}

Table C10: DSMC-derived Arrhenius coefficients, forward associative ionization (endothermic)

No	Reaction	Temp. range	Arrhenius Law Constants		
			A	β	ϵ_a
19a	$N + N \to N_2^+ + e^-$	-	1.66×10^{-17}	-0.03	9.284×10^{-19}
20a	$N + O \to NO^+ + e^-$	-	1.81×10^{-17}	-0.01	4.412×10^{-19}
21a	$O + O \to O_2^+ + e^-$	-	2.46×10^{-19}	0.24	1.112×10^{-18}

Table C11: DSMC-derived Arrhenius coefficients, reverse associative ionization (exothermic)

No	Reaction	Temp. range	Arrhenius Law Constants		
			A	β	ϵ_a
19b	$N_2^+ + e^- \to N + N$	< 20000	2.10×10^{-14}	0.07	2.000×10^{-20}
19b	$N_2^+ + e^- \to N + N$	> 20000	8.66×10^{-11}	-0.77	2.000×10^{-20}
20b	$NO^+ + e^- \to N + O$	< 18500	3.72×10^{-14}	-0.00	2.000×10^{-20}
20b	$NO^+ + e^- \to N + O$	> 18500	4.62×10^{-10}	-0.96	2.000×10^{-20}
21b	$O_2^+ + e^- \to O + O$	< 14500	2.63×10^{-13}	-0.19	2.000×10^{-20}
21b	$O_2^+ + e^- \to O + O$	> 14500	1.45×10^{-11}	-0.61	2.000×10^{-20}

Table C12: DSMC-derived Arrhenius coefficients, forward exchange (endothermic)

No	Reaction	Temp. range	Arrhenius Law Constants		
			A	β	ϵ_a
22a	$N_2 + O \rightarrow NO + N$	-	1.93×10^{-13}	-0.79	5.175×10^{-19}
23a	$NO^+ + N \rightarrow N_2^+ + O$	-	2.24×10^{-14}	-0.56	4.901×10^{-19}
24a	$NO + O \rightarrow O_2 + N$	-	1.45×10^{-20}	0.67	2.719×10^{-19}
25a	$NO + O^+ \rightarrow O_2 + N^+$	< 7500	6.45×10^{-01}	-3.73	3.673×10^{-19}
25a	$NO + O^+ \rightarrow O_2 + N^+$	7500 - 15000	7.93×10^{-06}	-2.47	3.673×10^{-19}
25a	$NO + O^+ \rightarrow O_2 + N^+$	> 15000	1.02×10^{-09}	-1.54	3.673×10^{-19}

Table C13: DSMC-derived Arrhenius coefficients, reverse exchange (exothermic)

No	Reaction	Temp. range	Arrhenius Law Constants		
			A	β	ϵ_a
22b	$NO + N \rightarrow N_2 + O$	< 4000	3.42×10^{-17}	0.07	2.000×10^{-20}
22b	$NO + N \rightarrow N_2 + O$	> 4000	4.82×10^{-15}	-0.53	2.000×10^{-20}
23b	$N_2^+ + O \rightarrow NO^+ + N$	< 4000	1.14×10^{-19}	0.88	2.000×10^{-20}
23b	$N_2^+ + O \rightarrow NO^+ + N$	> 4000	5.82×10^{-15}	-0.43	2.000×10^{-20}
24b	$O_2 + N \rightarrow NO + O$	< 4000	5.60×10^{-19}	0.58	2.000×10^{-20}
24b	$O_2 + N \rightarrow NO + O$	4000 - 10000	4.60×10^{-17}	0.04	2.000×10^{-20}
24b	$O_2 + N \rightarrow NO + O$	> 10000	5.30×10^{-15}	-0.47	2.000×10^{-20}
25b	$O_2 + N^+ \rightarrow NO + O^+$	< 15000	1.18×10^{-19}	0.60	2.000×10^{-20}
25b	$O_2 + N^+ \rightarrow NO + O^+$	> 15000	4.53×10^{-16}	-0.26	2.000×10^{-20}
26	$N_2 + O^+ \rightarrow NO^+ + N$	< 7500	1.70×10^{-15}	-0.09	2.000×10^{-20}
26	$N_2 + O^+ \rightarrow NO^+ + N$	> 7500	1.51×10^{-16}	0.18	2.000×10^{-20}
27	$O_2^+ + N \rightarrow NO^+ + O$	-	3.12×10^{-16}	0.10	2.000×10^{-20}

Table C14: DSMC-derived Arrhenius coefficients, forward charge exchange (endothermic)

No	Reaction	Temp. range	Arrhenius Law Constants		
			A	β	ϵ_a
28a	$N_2 + O_2^+ \rightarrow N_2^+ + O_2$	-	2.37×10^{-19}	0.53	5.619×10^{-19}
29a	$N_2 + N^+ \rightarrow N_2^+ + N$	-	3.61×10^{-12}	-0.91	1.684×10^{-19}
30a	$N_2 + O^+ \rightarrow N_2^+ + O$	-	2.70×10^{-17}	0.16	3.148×10^{-19}
31a	$O_2 + NO^+ \rightarrow O_2^+ + NO$	-	1.00×10^{-14}	-0.75	4.501×10^{-19}
32a	$O_2^+ + N \rightarrow O_2 + N^+$	< 17500	2.46×10^{-12}	-0.80	3.945×10^{-19}
32a	$O_2^+ + N \rightarrow O_2 + N^+$	> 17500	2.41×10^{-07}	-1.98	3.945×10^{-19}
33a	$O_2^+ + O \rightarrow O_2 + O^+$	< 17000	1.72×10^{-26}	2.15	2.485×10^{-19}
33a	$O_2^+ + O \rightarrow O_2 + O^+$	> 17000	1.14×10^{-19}	0.54	2.485×10^{-19}

Table C15: DSMC-derived Arrhenius coefficients, reverse charge exchange (exothermic)

No	Reaction	Temp. range	Arrhenius Law Constants		
			A	β	ϵ_a
28b	$N_2^+ + O_2 \rightarrow N_2 + O_2^+$	-	1.29×10^{-19}	0.34	2.000×10^{-20}
29b	$N_2^+ + N \rightarrow N_2 + N^+$	< 10000	2.29×10^{-19}	0.80	2.000×10^{-20}
29b	$N_2^+ + N \rightarrow N_2 + N^+$	10000 - 17500	1.64×10^{-14}	-0.41	2.000×10^{-20}
29b	$N_2^+ + N \rightarrow N_2 + N^+$	> 17500	5.04×10^{-13}	-0.76	2.000×10^{-20}
30b	$N_2^+ + O \rightarrow N_2 + O^+$	< 17000	2.30×10^{-26}	2.02	2.000×10^{-20}
30b	$N_2^+ + O \rightarrow N_2 + O^+$	> 17000	1.56×10^{-17}	-0.07	2.000×10^{-20}
31b	$O_2^+ + NO \rightarrow O_2 + NO^+$	< 7000	2.49×10^{-33}	4.39	2.000×10^{-20}
31b	$O_2^+ + NO \rightarrow O_2 + NO^+$	7000 - 15000	1.09×10^{-20}	1.10	2.000×10^{-20}
31b	$O_2^+ + NO \rightarrow O_2 + NO^+$	> 15000	2.09×10^{-12}	-0.88	2.000×10^{-20}
32b	$O_2 + N^+ \rightarrow O_2^+ + N$	< 15000	1.53×10^{-14}	-0.37	2.000×10^{-20}
32b	$O_2 + N^+ \rightarrow O_2^+ + N$	> 15000	3.61×10^{-12}	-0.94	2.000×10^{-20}
33b	$O_2 + O^+ \rightarrow O_2^+ + O$	< 8500	9.01×10^{-25}	1.91	2.000×10^{-20}
33b	$O_2 + O^+ \rightarrow O_2^+ + O$	> 8500	7.30×10^{-17}	-0.11	2.000×10^{-20}